Search for the Neutral Long-Lived Kaon Rare Decay $K_L \to \pi^0 \nu\bar{\nu}$

by

Stephanie Y. Su

A dissertation submitted in partial fulfillment
of the requirements for the degree of
Doctor of Philosophy
(Physics)
in The University of Michigan
2019

Doctoral Committee:

Professor Myron Campbell, Chair
Professor Christine Aidala
Dr. Brian Beckford
Professor Sara Pozzi
Professor Benjamin Safdi


THE UNIVERSITY OF MICHIGAN
ARTES · SCIENTIA · VERITAS
1817

Stephanie Y. Su
stephsu@umich.edu
ORCID iD: 0000-0003-3869-2260

To my fiance, Timothy Brubaker, for being my pillar.

To my best friend Hsuan-Yu Lin, and my sisters Caroline Su, Michelle Su, for supporting me throughout my graduate life.

To my beloved parents, who provided me with everything.

Acknowledgements

This work would not have been accomplished without the effort and support of many people.

First and foremost, I would like to thank Professor Myron Campbell, who actively reached out to me and brought me into the KOTO experiment. Myron is more than an advisor and mentor, he is a friend. I appreciate his leadership and caring for others. I have benefited and learned from Myron not only about research but also about life.

I want to thank Dr. Brian Beckford for helping to broaden my vision and outlook. He brought in ideas and values that have impacted my views towards graduate school, academia, and life. I admire his philosophical approach to life that acknowledges and incorporates all of our aspects and identities.

I would like to thank my DAQ comrades Myron, Dr. Monica Tecchio, previous Osaka University graduate student Dr. Yasuyuki Sugiyama, and previous graduate student Dr. Jia Xu. The system would not have been successfully designed and built without teamwork. I appreciate Monica for her mentorship over my graduate studies, and for always trying to instill joy in our work and group. Yasu is very knowledgeable, a senpai I look up to. Myron's expertise in the data acquisition system made the paths of the system development clearer and easier to achieve. I am grateful to be part of the University of Michigan KOTO group.

I learned a lot working with Dr. Kōji Shiomi, Professor Hajime Nanjo, Professor Taku Yamanaka, Shigeto Seki, Ichinori Kamiji, Kota Nakagiri, and Satoshi Shinohara, and Kōichi Miyazaki. The effort of analysis in this study cannot be belittled, and I appreciate the teamwork with these people. I have also learned a lot from the

discussions with Chieh (Jay) Lin and Shih-Hsuan (Jack) Chen. I enjoyed the time of working with the analysis comrades and driving to different places for dinner after long work days in Tōkai. I would also like to thank Taku for hosting me in Japan and for my analysis in the KOTO experiment.

I am fortunate to be part of this experiment and appreciate the opportunities to think critically, build ideas, travel to meet people who work on cutting edge technologies, present work to the fields, and explore different countries. I will forever treasure this experience.

I appreciate many people who supported me throughout the ups and downs of my graduate life - classes, researches, teaching, and life - to which I cannot possibly list all of them. I am extremely grateful to have these people as my pillar, especially to my fiance Timothy Brubaker, my best friend since high school Hsuan-Yu Lin, my friend acquainted from KOTO Jack, my sisters Caroline Su and Michelle Su, and my parents Leslie Su and J.J. Su. Thank you for all the supports, especially for the past five and a half years, with my joy and tears, successes and struggles, and pride and complains.

February, 2019

Stephanie Su

Table of Contents

List of Figures

List of Tables

List of Appendices

Abstract

The goal of the KOTO experiment is to search for the direct CP violating decay mode, $K_L \to \pi^0\nu\overline{\nu}$, and to probe for physics beyond the Standard Model of the elementary particle physics by measuring the branching ratio of this decay.

The data was analyzed by a blind analysis technique and determined a single event sensitivity of $(1.30 \pm 0.01_{\,stat.} \pm 0.14_{\,sys.}) \times 10^{-9}$ with 0.42 ± 0.18 background events in the signal region. No candidate events in the signal region was observed, which allows an upper limit of 3.0×10^{-9} to be set at 90% confidence level. This is more than an order of magnitude improvement from the previous result in the 2013 analysis with single event sensitivity of $(1.28 \pm 0.04_{\,stat.} \pm 0.13_{\,sys.}) \times 10^{-8}$ and upper limit of 5.1×10^{-8} at 90% confidence level. The analysis of the 2015 data will be discussed in this thesis.

Chapter 1
Introduction

Among our current universe, we observe more matter than antimatter. It is assumed that at the time of the Big Bang, when a matter encounters its antiparticle, they annihilate. However, the matter-antimatter balanced universe it not this is not the situation we live in. Perhaps the matter-antimatter asymmetry is a local phenomenon, where we live in a corner of the matter-dominated universe, which can be balanced by the antimatter-dominated region in the universe elsewhere. The border of an antimatter-dominated region would be noticeable. On the other hand, current astrophysical observations, such as cosmic microwave background, have not detected any sign suggested an antimatter-dominated region in the universe. This chapter will introduce the matter-antimatter asymmetry, leading to the motivation of searching for the $K_L \to \pi^0 \nu\overline{\nu}$ decay.

1.1 The Standard Model

In contemporary particle physics, the Standard Model (SM) is a theory that describes all known elementary particle interactions, except gravity. Figure 1.1 shows the SM fundamental particles. It contains six quarks, six leptons, and five gauge bosons, and the Higgs boson. The gauge bosons carry three fundamental forces for particle interactions: strong (g), electromganeticc (γ), and weak interactions ($Z^0, W^{\pm}$). Quarks are involved in strong interaction and often observed in a combination of compound particles, called "hadron." Hadron refers to two types of quark combinations: "mesons" and "baryons." Mesons are composed by a quark and an

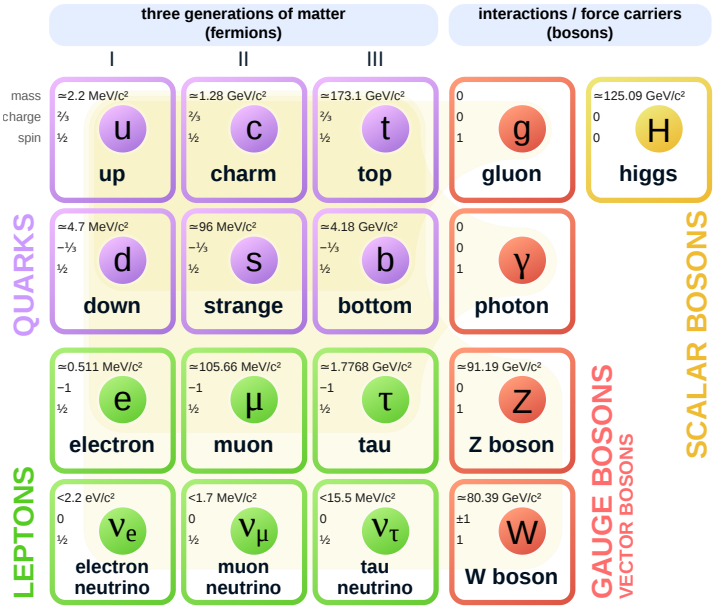

Figure 1.1: The Standard Model of elementary particles [1].

anti-quark. Baryons consist of three quarks or three anti-quarks. The quarks and leptons together are called fermions, which can involve in weak interaction. The Higgs boson gives rise to particle mass. Since the discovery of the Higgs boson in 2012 [2, 3, 4, 5], the existence of all SM fundamental particles are experimentally confirmed. The measurements are consistent to the SM prediction.

1.2 CP Violation and Kaon Phenomenology

In the quantum field theory, there are three important discrete symmetries: charge conjugation (C), parity (P), and time reversal (T). Charge conjugation converts a particle to its antiparticle. Its charge conjugation number is represented with its orbital angular momentum l and total spin s to be $(-1)^{l+s}$. Parity inverts a particle's spatial coordinates. It can be presented by the angular momentum of a particle to be $(-1)^{l}$. Time reversal symmetry refers to a particle interaction process is invariant under time.

The charge symmetry is invariant if the particle is its own eigenstate, which only

few particles have this property. The parity symmetry can be broken in weak interaction. Both charge conjugation and parity symmetries can be broken individually and were observed experimentally. However, Charge-Parity symmetry (CP-symmetry) was once believed to be conserved, after the discovery of the parity violation in 1957 [6], until the neutral kaon experiment performed by Cronin and Fitch in 1964 [7]. Though CP-symmetry can be broken, CPT-symmetry holds invariant. If CP violation occurs, there is a compensating T violation.

1.2.1 $K^0 - \bar{K}^0$ Mixing

A neutral kaon (K^0) is a meson composed of a s quark and a d quark, with an electric charge of 0. The states of a neutral kaon meson and its antiparticle can be represented in Eq. 1.1 and Eq. 1.2, respectively.

$$K^0 = (\bar{s}, d) \tag{1.1}$$

$$\bar{K}^0 = (s, \bar{d}) \tag{1.2}$$

By performing the CP operation on neutral kaons, we found that neither of them are their weak eigenstates, as shown in Eq. 1.3 and Eq. 1.4.

$$CP\,|K^0\rangle = |\bar{K}^0\rangle \tag{1.3}$$

$$CP\,|\bar{K}^0\rangle = |K^0\rangle \tag{1.4}$$

As the result, the normalized CP eigenstate of neutral kaon can be represented as a combination of K^0 and $\bar{K}^0$, where

$$|K_1\rangle = \frac{1}{\sqrt{2}}\,(|K^0\rangle + |\bar{K}^0\rangle), \tag{1.5}$$

$$|K_2\rangle = \frac{1}{\sqrt{2}}\,(|K^0\rangle - |\bar{K}^0\rangle), \tag{1.6}$$

and

$$CP\,|K_1\rangle = \frac{1}{\sqrt{2}}\left(|\bar{K}^0\rangle + |K^0\rangle\right) = |K_1\rangle\,, \tag{1.7}$$

$$CP\,|K_2\rangle = \frac{1}{\sqrt{2}}\left(|\bar{K}^0\rangle - |K^0\rangle\right) = -\,|K_2\rangle\,. \tag{1.8}$$

Neutral kaons can normally decay into two or three π^0 mesons. A π^0 is a pseudoscalar and has parity eigenvalue of -1 ($s = 0, l = 1$), which is a CP odd state. From Eq. 1.7 and Eq. 1.8, the K_1 and K_2 are CP even and odd states, respectively. Therefore, the K_1 particle is expected to decay into two π^0 mesons rather than three π^0 mesons, and the K_2 particle is expected to decay into three π^0 mesons instead of two π^0 mesons. Considering the energy of the decays, K_1 is expected to quickly release its energy and have a shorter lifetime, and K_2 is expected to have a longer lifetime. This prediction, by Gell-Mann and Pais [9] in 1954, was observed at Brookhaven in 1956 [10]. However, in 1964, Cronin and Fitch found $2\pi^0$ events from K_L decays, where only $3\pi^0$ decays were expected [7].

This result indicated that the CP-symmetry can indeed be broken, and K_L is mainly composed of the K_2 state with a small contribution of the K_1 state, as represented in Eq. 1.9.

$$|K_L\rangle = \frac{1}{\sqrt{1+\epsilon^2}}\left(|K_2\rangle + \epsilon\,|K_1\rangle\right) \tag{1.9}$$

Similar to K_S, where

$$|K_S\rangle = \frac{1}{\sqrt{1+\epsilon^2}}\left(|K_1\rangle + \epsilon\,|K_2\rangle\right). \tag{1.10}$$

The parameter ϵ indicates the strength of the contamination contributing to the CP-violation. The value of ϵ is [8]

$$|\epsilon| = (2.228 \pm 0.011)\ \times 10^{-3} \tag{1.11}$$

1.2.2 The Cabibbo–Kobayashi–Maskawa (CKM) Matrix

The Cabibbo–Kobayashi–Maskawa (CKM) matrix is a unitary matrix that represents the transformation between the flavor eigenstates and the mass eigenstates among three generations of quarks. The CKM matrix representations are described in Eq. 1.12. Equation 1.13 shows the CKM matrix with Wolfenstein parameterization of $\lambda = |V_{us}| = 0.22$ [11].

$$V_{CKM} = \begin{pmatrix} V_{ud} & V_{us} & V_{ub} \\ V_{cd} & V_{cs} & V_{cb} \\ V_{td} & V_{ts} & V_{tb} \end{pmatrix} \tag{1.12}$$

$$= \begin{pmatrix} 1 - \frac{\lambda^2}{2} & \lambda & A\lambda^3(\rho - i\eta) \\ -\lambda & 1 - \frac{\lambda^2}{2} & A\lambda^2 \\ A\lambda^3(1 - \rho - i\eta) & -A\lambda^2 & 1 \end{pmatrix} + O(\lambda^4) \tag{1.13}$$

The parameters are

$$\lambda = \frac{|V_{us}|}{\sqrt{|V_{ud}|^2 + |V_{us}|^2}}\,, \tag{1.14}$$

$$A\lambda^2 = \lambda \left| \frac{V_{cb}}{V_{us}} \right|\,, \tag{1.15}$$

$$A\lambda^3(\rho + i\eta) = V_{ub}^*\,. \tag{1.16}$$

The η term is the contribution to the CP violation.

1.2.3 $K_L \to \pi^0 \nu\bar{\nu}$ Decay

To probe for the CP violation decays in the quark sector, there are four "golden" process: asymmetries in $B^0 \to J/\psi\, K_S^0$ decays, the ratio of $B_s - B_d$ mixing, $K^+ \to$

$\pi^+\nu\bar{\nu}$, and $K_L \to \pi^0\nu\overline{\nu}$. These decays involve Flavor Changing Neutral Current (FCNC) processes, which undergo weak interactions. The FCNC process is forbidden at tree level in the SM. They have to proceed through higher order loop diagrams with $W^{\pm}$ or Z^0 bosons. Because the rates of FCNC processes are small, these studies are referred to as precision measurements.

The $K_L \to \pi^0\nu\overline{\nu}$ process is a direct CP violating decay involving the transition of $s \to d$. The Feynman diagrams are drawn in Fig. 1.2.

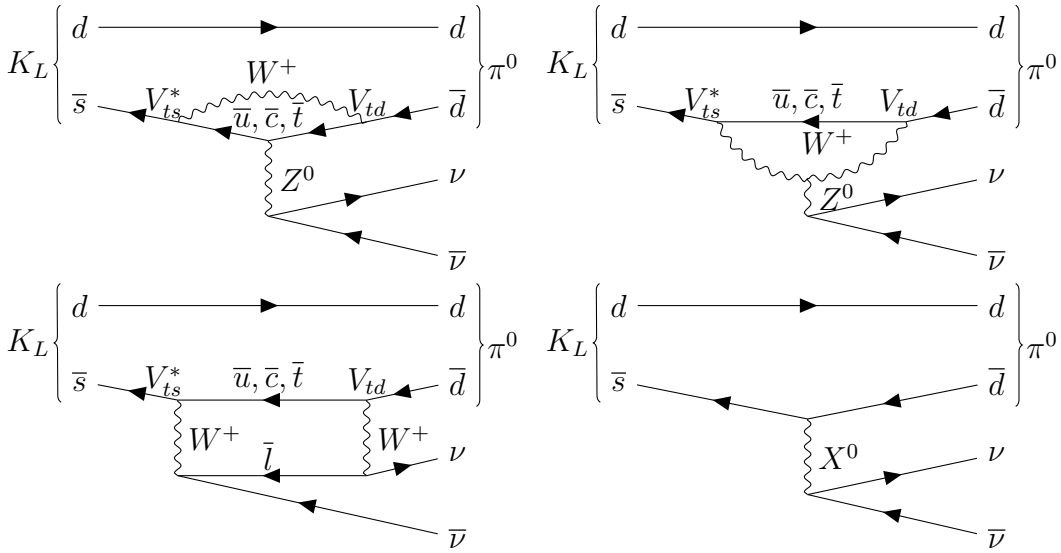

Figure 1.2: Feynman diagrams of the $K_L \to \pi^0\nu\overline{\nu}$ decay. The top two and the bottom left figures are the Feynman diagrams from the SM. The bottom right diagram is an interaction beyond the SM with unknown particle X^0.

The $K_L \to \pi^0\nu\overline{\nu}$ decay represented in the unitary triangle constructed from the CKM matrix can be written as Eq. 1.17.

$$V_{us}^* V_{ud} + V_{cs}^* V_{cd} + V_{ts}^* V_{td} = 0, \tag{1.17}$$

which is used to construct the unitary triangle by dividing the middle term, as shown in Fig. 1.3. The $\bar{\eta}$ term, which associates with the CP violation strength, can be obtained directly by measuring the branching ratio of $K_L \to \pi^0\nu\overline{\nu}$ or indirectly by measuring the branching ratio of $K^+ \to \pi^+\nu\bar{\nu}$.

The branching ratio of a decay refers to the fraction of particles which undergoes

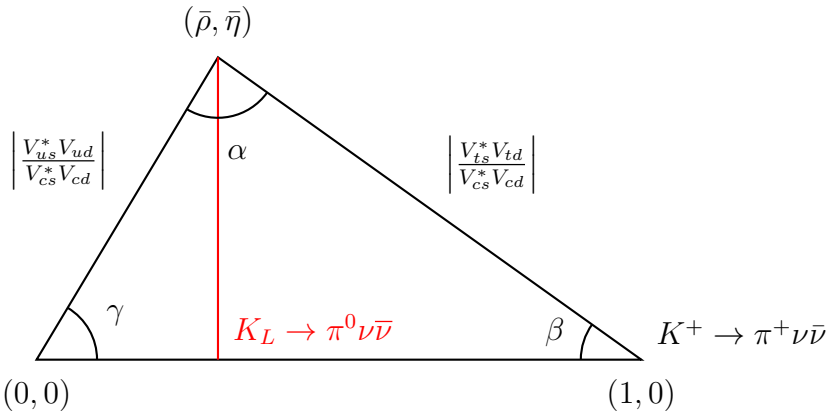

Figure 1.3: The unitary triangle related to $K_L \to \pi^0 \nu\overline{\nu}$ and $K^+ \to \pi\nu\bar{\nu}$. The branching ratio of $K_L \to \pi^0 \nu\overline{\nu}$ is directly related to the CP violation strength, $\bar{\eta}$.

an individual decay mode with respect to the total number of particles which decay. The branching ratio of the $K_L \to \pi^0 \nu\overline{\nu}$ decay, represented as $BR(K_L \to \pi^0 \nu\bar{\nu})$, is described in Eq. 1.18. In the FCNC process of the $K_L \to \pi^0 \nu\overline{\nu}$ decay, t quark dominates the flavor changing vertices over u and c quarks due to its heavy mass.

$$BR(K_L \to \pi^0 \nu\bar{\nu}) = \kappa_L \left(\frac{\mathrm{Im}(V_{td} V_{ts}^*)}{\lambda^5} X(x_t) \right)^2 \tag{1.18}$$

$$= \kappa_L A^4 \bar{\eta}^2 X^2(x_t) \tag{1.19}$$

The term $x_t = M_t^2 / M_W^2$ is the square of the mass ratio between the top quark and the W boson, and $X(x_t)$ is the Inami-Lim loop function [12]. The factor κ_L includes other effects and is given to be

$$\kappa_L = (2.231 \pm 0.013) \times 10^{-10} \left(\frac{\lambda}{0.225} \right)^8 . \tag{1.20}$$

Due to theoretical cleanness of the $K_L \to \pi^0 \nu\overline{\nu}$ decay, its branching ratio can be calculated accurately to be [13]

$$BR(K_L \to \pi^0 \nu\bar{\nu}) = (3.00 \pm 0.30) \times 10^{-11}. \tag{1.21}$$

1.2.4 Grossman-Nir Bound

The branching ratio between $K^+ \to \pi^+\nu\bar{\nu}$ and $K_L \to \pi^0\nu\bar{\nu}$ can be related by calculation using isospin symmetry [14] as

$$BR(K_L \to \pi^0\nu\bar{\nu}) < 4.4 \times BR(K^+ \to \pi^+\nu\bar{\nu}). \tag{1.22}$$

This relationship is called the "Grossman-Nir" bound. The upper limit of the $K_L \to \pi^0\nu\bar{\nu}$ branching ratio is bounded by the $K^+ \to \pi^+\nu\bar{\nu}$ branching ratio. Physics models are allowed in the region where the Grossman-Nir relationship is satisfied until being ruled out experimentally, as shown in Fig. 1.4. Figure 1.5 shows the upper limit of $BR(K_L \to \pi^0\nu\bar{\nu})$ measured directly or indirectly with 90% Confidence Level (C.L.).

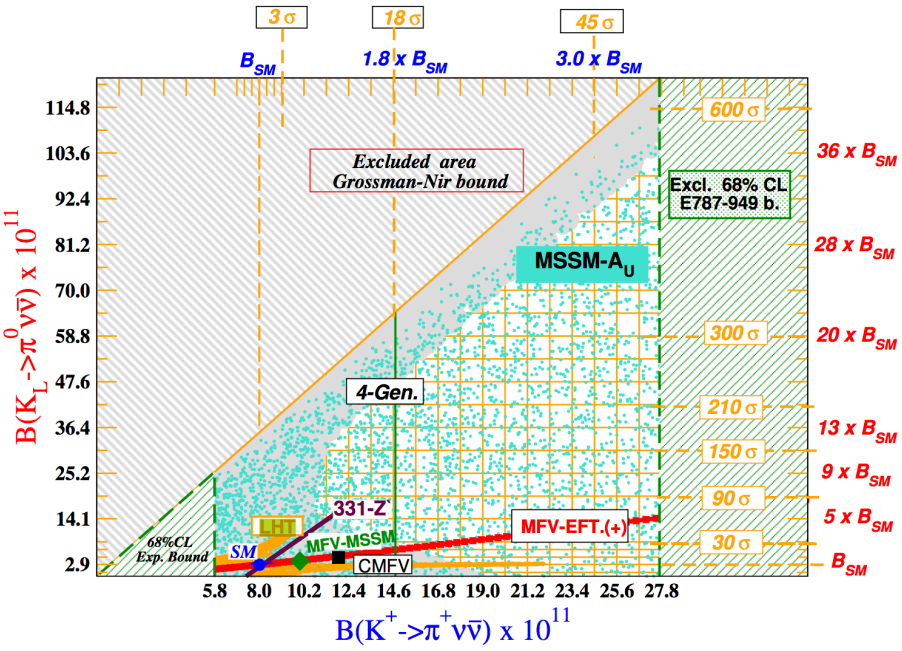

Figure 1.4: The Grossman-Nir relationship between the branching ratios of $K_L \to \pi^0\nu\bar{\nu}$ and $K^+\pi^+\nu\bar{\nu}$ with new physics models beyond the SM [15].

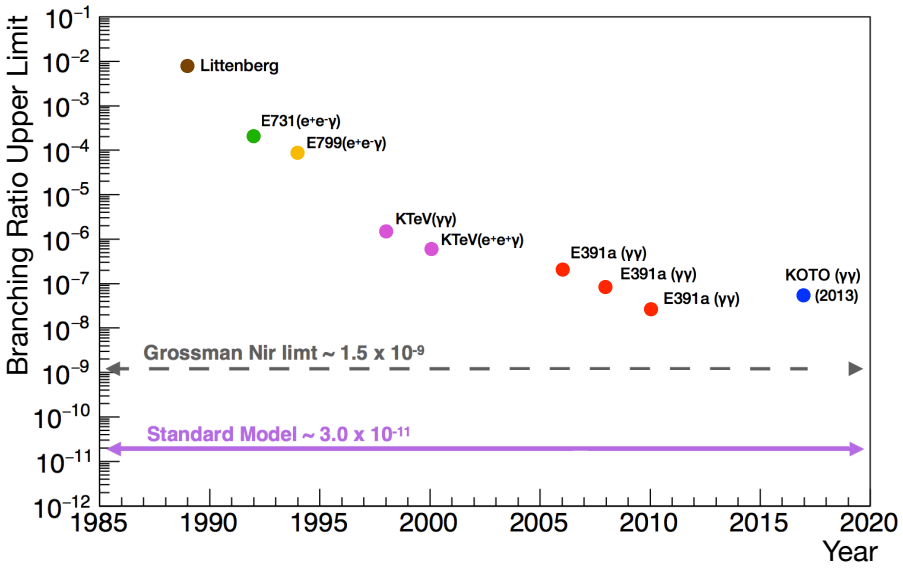

Figure 1.5: Previous searches of $BR(K_L \to \pi^0\nu\overline{\nu})$ upper limit.

1.2.5 Beyond the SM (BSM)

The CP violation cannot fully account for the amount of matter-antimatter asymmetry, where the baryon number violation and non-thermal equilibrium also take part in the contribution. Many theoretical models , such as Littlest Higgs with T-parity (LHT) [16], Minimal Supersymmetric Model (MSSM) [17], Z' Model, and Minimal Flavour Violation (MFV) [18] aim to explore physics beyond the SM, as shown in Fig. 1.4.

1.3 The KOTO Experiment

The KOTO experiment was designed to observe $K_L \to \pi^0\nu\overline{\nu}$ events directly by observing two photons and nothing else. The missing transverse momentum carried by the neutrinos give the signature of large transverse momentum on two photons. The KOTO experiment is carried out under two steps [19]. The goal of "Step 1" is to observe a few $K_L \to \pi^0\nu\overline{\nu}$ events at the single event sensitivity (S.E.S.) of 8×10^{-12}. The goal of "Step 2" is to perform precise measurement of $BR(K_L \to \pi^0\nu\bar{\nu})$ by

observing 100 events with S.E.S. around 3×10^{-13}.

The KOTO experiment brings together over 60 collaborators from 16 different institutions among five countries.

1.4 Outline of This Thesis

This thesis presents the KOTO experiment 2015 runs and introduces how the analysis was proceed towards setting the upper limit of $K_L \to \pi^0\nu\overline{\nu}$ decay. Physics background and motivation was discussed in this chapter. Details of the KOTO experiment are described in Chap. 2. The data acquisition used in 2015 data collection is described in Chap. 3. The status of 2015 data collection and the data acquisition performance are discussed in Chap. 4. The analysis approach used to observe $K_L \to \pi^0\nu\overline{\nu}$ events is discussed in Chap. 5. Details of $K_L \to \pi^0\nu\overline{\nu}$ analysis strategy including simulation methods, normalization, and background reduction are detailed in Chap. 6, 7, and 8, respectively. Chapter 9 described the result of the $K_L \to \pi^0\nu\overline{\nu}$ analysis using data from 2015, future upgrades, and conclusion. Acronyms used in this thesis are listed in Appx. C in alphabetical order.

My main contribution to the KOTO experiment was on the development, upgrades, and integration of the data acquisition system[1] (Chap. 3 and Chap. 4), study of the $K_L \to 3\pi^0$ normalization mode (Chap. 7), as well as background studies of $K_L \to \pi^+\pi^-\pi^0$, $K_L \to 2\gamma$ decay modes, and scattered K_L (Chap. 8).

[1] Level 3 trigger system and event building development and the Level 2 hardware trigger upgrade

Chapter 2
The KOTO Experiment

The KOTO experiment was designed to observe the $K_L \to \pi^0\nu\overline{\nu}$ decay. The experiment is located at Japan Proton Accelerator Research Complex (J-PARC) [20]. The name of the experiment, KOTO, was taken from the neutral kaon ($\boldsymbol{K^0}$) decay at J-PARC, which is in the **Tō**kai village at Ibaraki prefecture in Japan. The KOTO experiment took its first physics run in 2013 with 100 hours of data taking. The data taking was stopped due to the accident in Hadron Hall [21]. The upper limit of $K_L \to \pi^0\nu\overline{\nu}$ branching ratio was set to be 5.1×10^{-8} [22]. The setup of the KOTO experiment in 2015 is described in this chapter.

2.1 J-PARC Facility

The J-PARC facility is a high-intensity proton accelerator facility in Ibaraki, Japan. A bird's-eye view of J-PARC is shown in Fig. 2.1. It contains three accelerator facilities and three experimental facilities. The accelerator facilities are: a linear accelerator (LINAC) [23], a 3 GeV Rapid Cycle Synchrontron (RCS) [24], and the Main Ring (MR) [25]. The experimental facilities are: the Material and Life science experimental Facility (MLF), the Neutrino Experimental facility (NU) [26], and the Hadron experimental hall (HD-hall) [27, 28].

2.1.1 Accelerator Facilities

Negative hydrogen ions (H^-) are extracted from the ion source and accelerated up to 400 MeV by the LINAC. The accelerated H^- ions are converted to protons

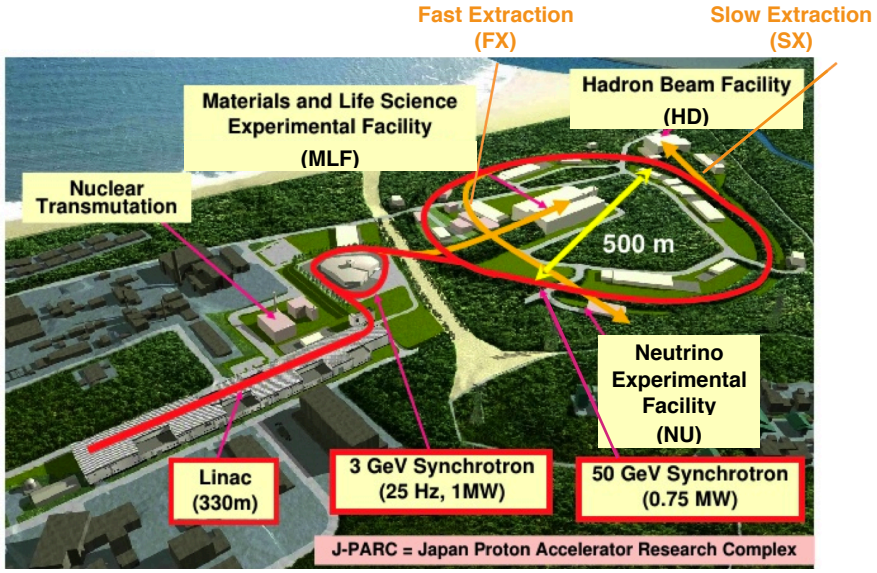

Figure 2.1: J-PARC bird's eye view.

via electron-stripping foil located at the injection point of the RCS over a period of 0.5 ms. The RCS accelerates protons up to 3 GeV with repetition of 25 MHz and delivers the protons to the either the MR or the MLF. The MR further accelerates the protons from 3 GeV to 30 GeV with repetition of 0.2∼0.7 Hz.[1] The accelerated 30 GeV protons are extracted by either the fast extraction (FX) within 5.23 μs or the slow extraction (SX) within 2 s. The FX delivers the beam to the NU with repetition cycles of 3.2 s and 2.6 s, using kicker magnets. The SX delivers the proton beam to HD with a repetition of 6 s, using a resonant extraction. As of December 2015, the MR achieved operation with beam power of 330 kW for FX and 42 kW for SX.

2.1.2 Hadron Experiment Hall

The hadron experimental hall (HD-hall) is designed to use the megawatt (MW)-class proton beams from the MR to provide secondary beams for various experiments inside the HD-hall. The layout of the HD-hall is shown in Fig. 2.2. It has dimensions of 60 m in width and 56 m in length. The proton beam in the MR with energy of

[1]The MR was designed for accelerating protons up to 50 GeV. In 2015, the proton energy in the MR was operated at 30 GeV.

30 GeV and beam power of 240 kW is slowly extracted to the HD-hall via the Switch Yard (SY), which has the length of approximately 200 m, over 2 s. The beam was extracted every 6 s in the runs prior to summer 2015 and 5.52 s afterwards. A "Spill" refers to a cycle of the extraction of a shot of beam. Figure 2.3 is an illustration of a spill and its relation to the KOTO data taking.

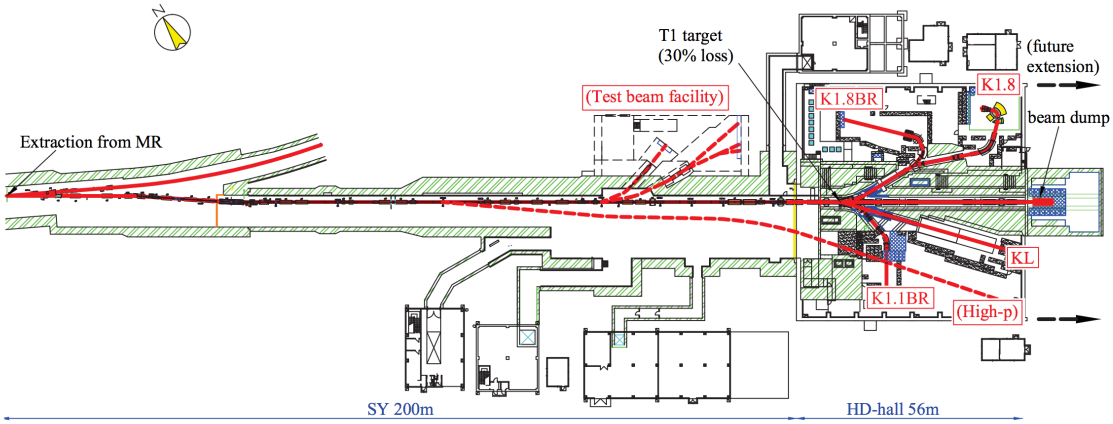

Figure 2.2: Layout of the primary beamline extraction to the HD-hall [29].

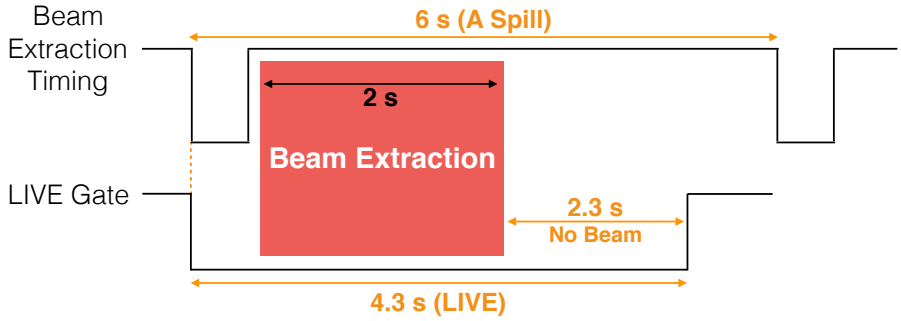

Figure 2.3: A typical spill cycle. The beam extraction occurs over 2 s, with repetition of 6 s. The beam extraction period is called "On Spill", the no beam period is called "Off Spill". A "LIVE" signal is on as the beam extraction starts, and the KOTO data acquisition system collects data during this period. Details are in Chap. 3.

The "spill duty factor" is defined in Eq. 2.1, which is a measurement of the per-

formance of the beam extraction.

$$\text{Spill Duty Factor} = \frac{\left[\int_0^T I(t)\,dt\right]^2}{\int_0^T dt \int_0^T I^2(t)\,dt} \tag{2.1}$$

The variable T is the beam extraction time (spill length) and $I(t)$ is the beam current (extracted protons). The closer the spill duty factor is to value of 1, the flatter the time structure of the extracted beam is. In the 2015 runs, the spill duty factor varied between 40%∼50%.

The protons extracted from the MR (primary proton beam) are delivered to the T1 production target (T1-target) and produce secondary particle beams (secondary beam) including kaons, pions, antiprotons, and so on. Figure 2.4 shows a picture of the T1-target used in 2015. The T1-target consists of two gold bars, with only one is used at a time, sitting on top of a copper block with water cooling system. The secondary particles produced by the T1-target are delivered to different experiments. A total of three beam lines were used in 2015, two for charged and one for a neutral beam.

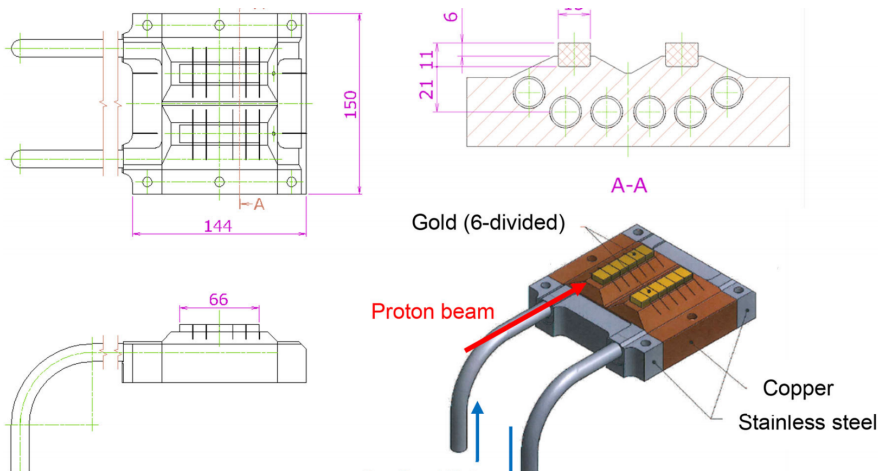

Figure 2.4: Schematic view of the T1-target [30]. The target is composed of two gold bars, with a cross section of 6×11 mm^2 and length of 66 mm. The units labeled in this figure are in mm.

2.2 Beamline

The "KL" beamline is used to deliver secondary beam produced by the T1-target to the KOTO experiment. It is 21 m long and is at a 16° angle from the primary proton beam. The KOTO detector is located at the end of the KOTO beamline. Figure 2.5 and Fig. 2.6 show the layout and the components of the KL beamline. The KOTO experiment used the long beamline to allow shorter-lived neutral particles to decay such as K_s and Λ particles, 16° angle shifted from the primary beam to reduce high energy neutrons, and two collimators to produce narrow beam (pencil beam).

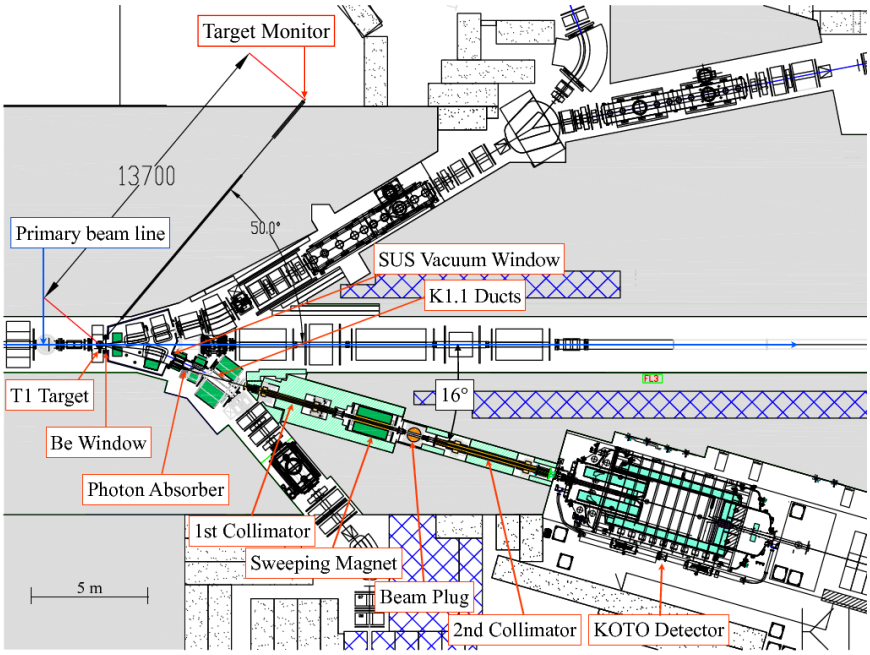

Figure 2.5: The KL beamline [31].

The KL beamline consists of a photon absorber (γ absorber), two sets of collimators, a sweeping magnet, and two beam plugs. The γ absorber is a lead block with a thickness of 7 cm and its purpose is to stop the photons produced from the T1-target. The collimators are designed to produce narrow beam with dimensions of 8 cm $\times$ 8 cm and to suppress neutron outside the beam (halo neutrons) produced by multiple scattering of the beam neutrons. Both collimators are made of iron wrapped in tungsten. The first and the second collimators have a length of 4 m and 5 m,

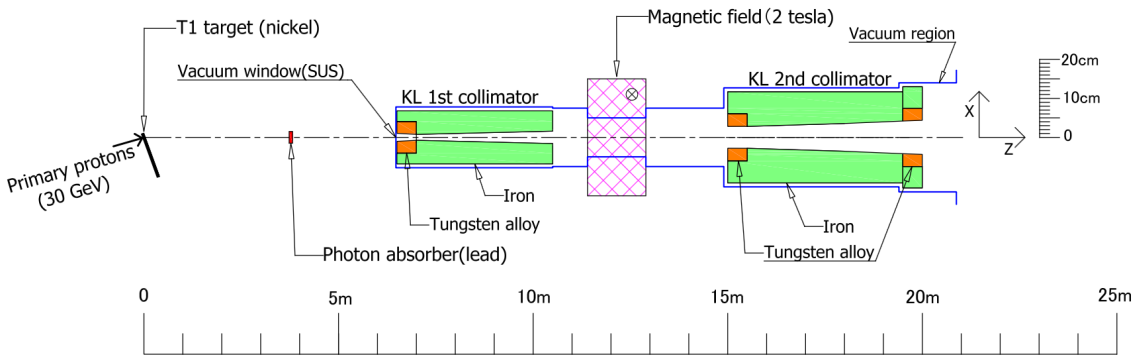

Figure 2.6: KL beamline components [32].

respectively. Charged particles from the T1-target are swept out by the sweeping magnet (KL-D1), which is a dipole magnet located between two collimators. A pair of rotatable D-shaped beam plug, made of brass, are located behind the sweeping magnet. The beam plug can be "opened" or "closed", which allows the neutral beam to go through between the two blocks or be blocked. The second beam plug is located between the second collimator and the KOTO detector. It is movable away from the beamline. We defined the downstream side of the second collimator to be the "beam exit".

2.3 The KOTO Detector

The $K_L \to \pi^0\nu\overline{\nu}$ decay can be identified by observing its final product of two photons with "nothing" else. Neutrinos cannot be detected and will escape from the KOTO detectors. The momentum carried away by the neutrinos results in the observation of large transverse momentum (P_T) on two photons decayed from the π^0. The KOTO detector is designed to observe the $K_L \to \pi^0\nu\overline{\nu}$ signal using a calorimeter, enclosed by hermetic veto detectors to ensure no particles escape from detection. Figure 2.7 is an schematic view of the KOTO detector. Cartesian coordinates are used in the KOTO experiment, where +x points in horizontal direction towards north of HD-hall, +y points towards vertical top, and +z points towards the direction of

the KL beam. The origin of the KOTO detector coordinates is on the KL beam axis, located at the upstream surface of the FB detector. All detectors have single-end readout system except for the MB, BCV, CV, and BHPV detectors. Table. 2.1 summarized some information of the KOTO detector.

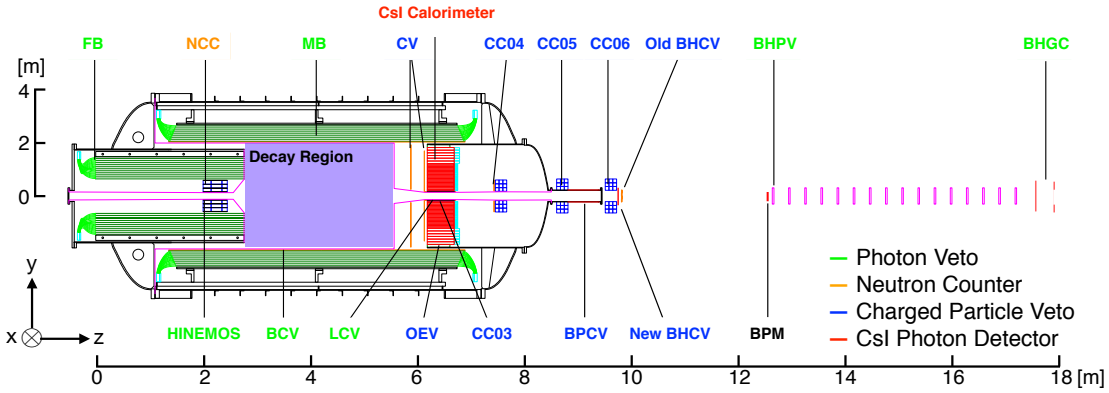

Figure 2.7: Schematic view of the KOTO Detector in 2015. The decay region is the low-vacuum area inside the KOTO detector, wrapped by the membrane (shaded purple region).

Table 2.1: Summary of the KOTO detector. Scintillators and CsI crystals are represented as "Scin." and "Crys." in the table, respectively. In 2015, the z coordinate of the T1-target was -21 m and the that of the beam exit was -1.507 m.

Detector	Module Length [cm]	Upstream Surface z Coordinate [mm]	Readout	Detector Type
FB	275	0	Single-end	Scin.
NCC	44.66	1998.4	Single-end	Crys. & Scin. (HINEMOS)
MB	550	1348	Single-end	Scin.
BCV	550	1348	Single-end	Scin.
CV	50	6142.77	Dual-end	Scin.
CsI	50	6148	Single-end	Crys.
LCV	50	6148	Single-end	Scin.
OEV	50	6148	Single-end	Scin.
CC03	50	6148	Single-end	Crys.
CC04	See Fig. 2.14	7415	Single-end	Crys. & Scin.
CC05	See Fig. 2.14	8773	Single-end	Crys. & Scin.
CC06	See Fig. 2.14	10338	Single-end	Crys. & Scin.
new BHCV	See Fig. 2.15	10571.7	Single-end	Wire
BPCV	100	9064.5	Single-end	Scin.
BHPV	See Fig. 2.17	12460	Dual-end	Cherenchov
BHGC	See Fig. 2.18	18195	Single-end	Scin.

2.3.1 CsI calorimeter

The electromagnetic calorimeter is made of two sizes of undoped Cesium Iodide (CsI) crystals. Figure 2.8 shows the illustration of the CsI calorimeter. The cross section of the small crystals is 2.5×2.5 cm^2 and that of the large crystals is 5×5 cm^2. Two types of photomultiplier tubes (PMT) are used in the CsI calorimeter readout. Hamamatsu 3/4 inch PMTs[1] were used for the small crystals, and Hamamatsu 1.5 inch PMTs[2] are used for the large crystals. The CsI calorimeter is composed of 2240 small crystals surrounded by 476 large crystals and stacked in a stainless steel cylinder with a diameter of 1.9 m. A total of 2716 crystals were used.

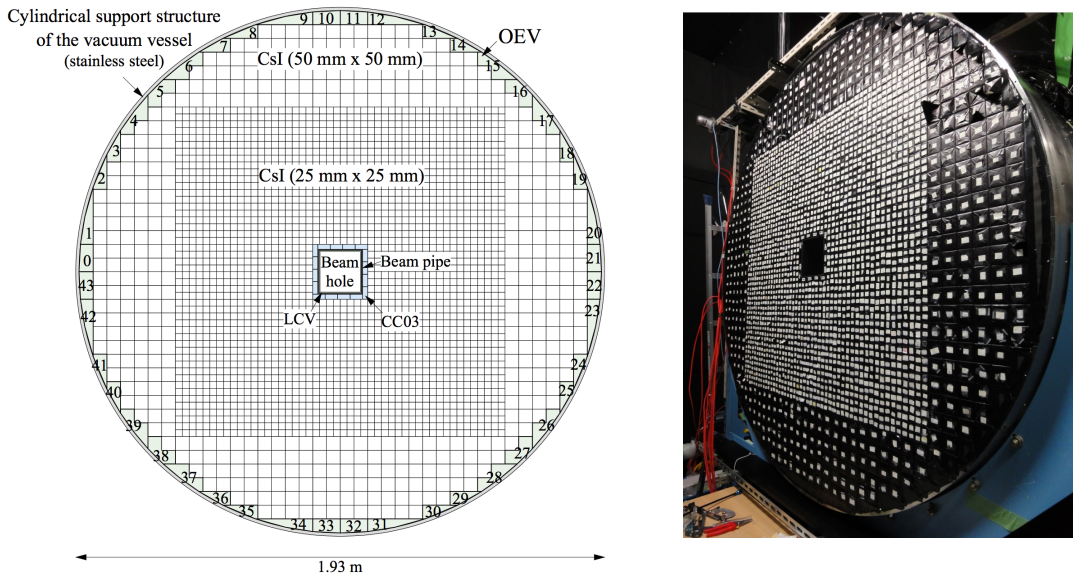

Figure 2.8: The CsI calorimeter - schematic view (left) towards downstream direction and a picture (right).

The CsI crystals are 50 cm in length, which is equivalent to 27 radiation lengths (X_0). Among all CsI crystals used, 20% of the crystals were made from a single crystal fabricated by HORIBA company and 80% of crystals were made by gluing two 25-cm long single crystals together. The "beam hole" refers to a square of 20×20 cm^2, located at the center of the CsI calorimeter, is designed to allow the beam to pass

[1] R5364
[2] R5330

without interacting with the CsI calorimeter. The beam hole is surrounded by the LCV and the CC03 detectors, which will be introduced in Sec. 2.3.6 and Sec. 2.3.8. The gap between the calorimeter and the support is filled with the OEV detector, which will be introduced in Sec. 2.3.7.

2.3.2 Front Barrel (FB) and Main Barrel (MB)

The front barrel (FB) and the main barrel (MB) detectors are designed to detect photons in the transverse direction from the K_L decay. Both detectors are made of sandwich layers of altering lead plates and organic scintillators. The lead plates increase the probability of photon interaction to the modules to create electromagnetic showers. Lights emitted from the excited electrons in the scintillators are captured by the wavelength shifting (WLS) fibers mounted in the groves of the scintillators and are converted from the ultraviolet light to visible light, then captured by the PMTs. Figure 2.9 shows the schematic view of the FB and the MB modules.

The FB detector contains 16 modules and the MB detector contains 32 modules. The FB detector has a single-end readout system and the PMTs are located at the upstream side of the detector. The MB detector has a dual-end readout system, where the PMTs are located at both the upstream and the downstream side of the detector to detect scintillating lights. Detailed information of the FB and the MB detectors are in Ref. [33].

2.3.3 Barrel Charged Veto (BCV)

A layer of scintillators with thickness of 10 mm is placed at the inner surface of the MB detector to detect charged particles. The barrel charged veto (BCV) detector, similar to the MB detector, consists of 32 modules and is a dual-end readout system.

2.3.4 Neutron Collar Counter (NCC) and HINEMOS

The neutron collar counter (NCC) is located inside the FB detector. The purpose of the NCC detector is to detector photons generated from the upstream $K_L \to 3\pi^0$

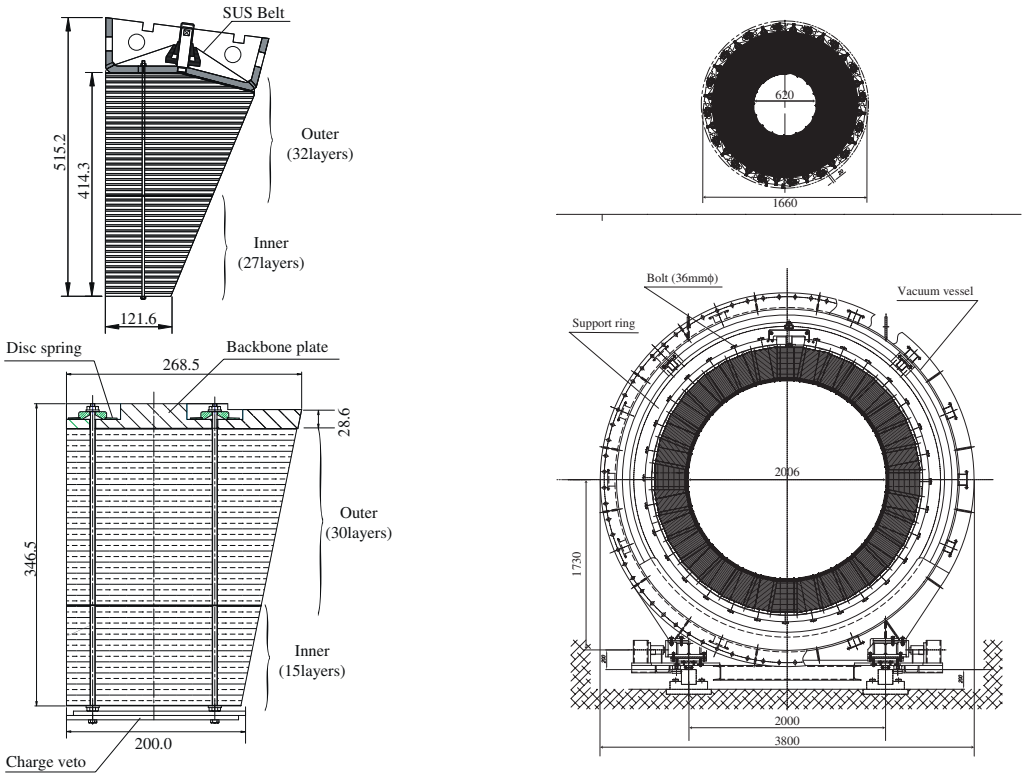

Figure 2.9: The FB and the MB modules (left) and detectors (right) [33]. The FB detector components are the at the top of the figure and the MB are at the bottom.

and $K_L \to 2\pi^0$ decays. It can also detect halo neutrons by observing the photons decayed from a π^0, generated from the interaction of halo neutrons with the detector.

The NCC detector is made of updoped CsI crystals and divided into three regions: front, middle, and rear [34]. An "individual" readout refers to the readout from one region of the module. This information is used for halo neutron measurement. A The "common" readout refers to the readout that connects all three regions. This information is used for vetoing extra photons from K_L decays. Only the "common" readout was used in the data analysis performed in this thesis.

The Horizontal Inner NCC Edge Mounted Scintillator (HINEMOS) consists of four pieces of scintillators, which are located at the inner surface of the NCC detector. Figure 2.10 shows the NCC detector configuration.

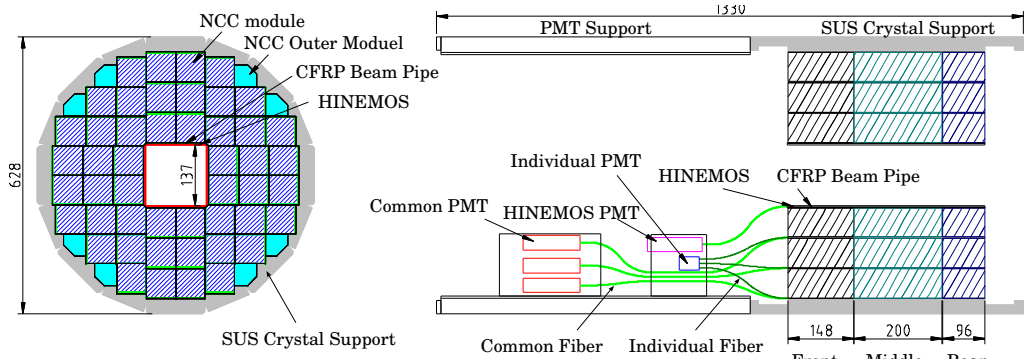

Figure 2.10: Schematic view of the NCC detector.

2.3.5 Charged Veto (CV)

The charged veto (CV) detector is located in front the CsI calorimeter and serves the purpose to detect charged particles. It consists of two layers of scintillators fixed on a Carbon-fiber-reinforced-plastic (CFRP) plate, each has a quadrant symmetry [35]. Figure 2.11 shows a schematic view of the CV detector. Each quadrant consists of 12 scintillator strips in the front layer and 11 scintillator strips in the rear layer. Each scintillator strip is 70.7 mm wide and 3 mm thick. The Multi-Pixel Photon Counters (MPPC) are attached to both ends of the CV modules for signal readout.

2.3.6 Liner Charged Veto (LCV)

The liner charged veto (LCV) detector is located at the inner surface of the beam pipe around the center square region of the CsI calorimeter shown in Fig. 2.8. The purpose of the LCV detector is to increase the detection efficiency for charged particles hitting the inside of the beam hole. The LCV detector is made of four 3-mm-think scintillator modules, with one module at each edge of the square region. Figure 2.12 illustrate the position of the LCV detector. More details can be found in Ref. [36].

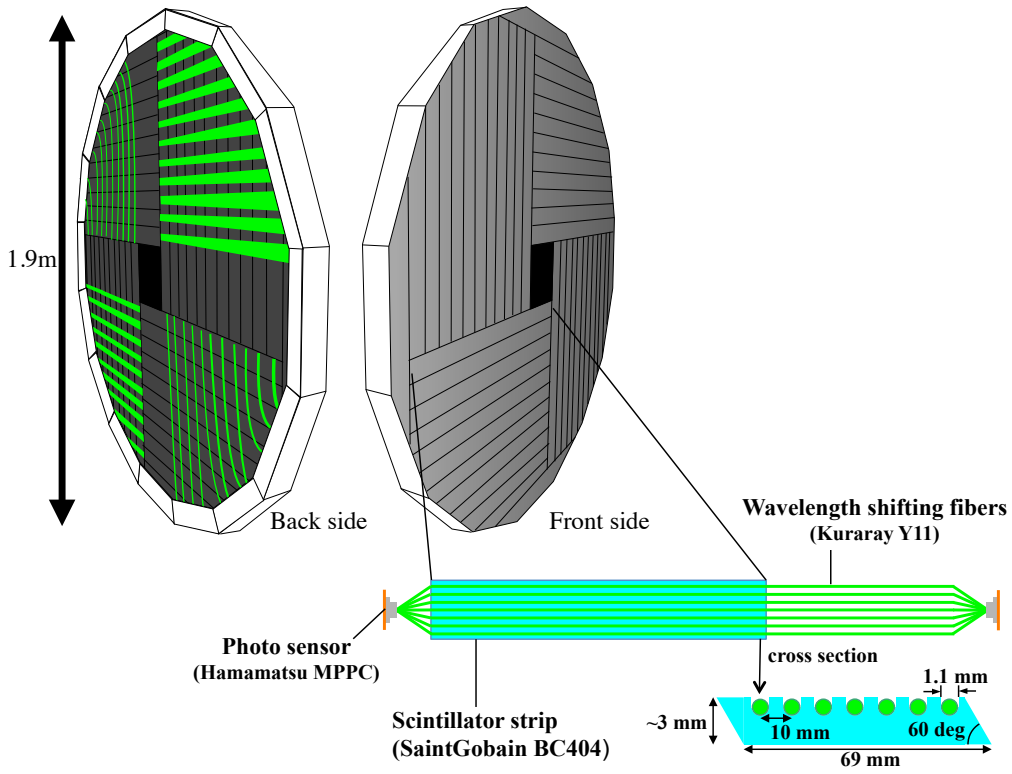

Figure 2.11: Configuration of the CV detector.

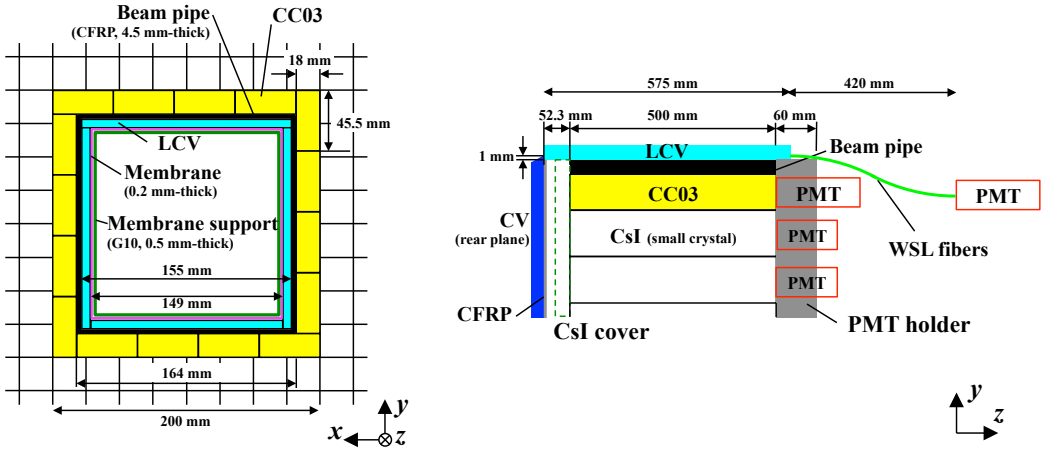

Figure 2.12: The LCV and the CC03 detectors. The left figure shows the zoomed in area of the beam hole area in Fig. 2.8. The right figure shows the side view in +x direction.

2.3.7 OEV

The outer edge veto (OEV) detector is located at the filling between the CsI calorimeter and the cylindrical-shaped structure. The purpose of the OEV detector

is to enclose the gap between the CsI calorimeter and the cylindrical support. The OEV detector has various shapes and it consists of 44 modules made of the layers of lead plates and scintillators. Figure 2.13 shows the structure of the OEV detector. More details can be found in Ref. [37].

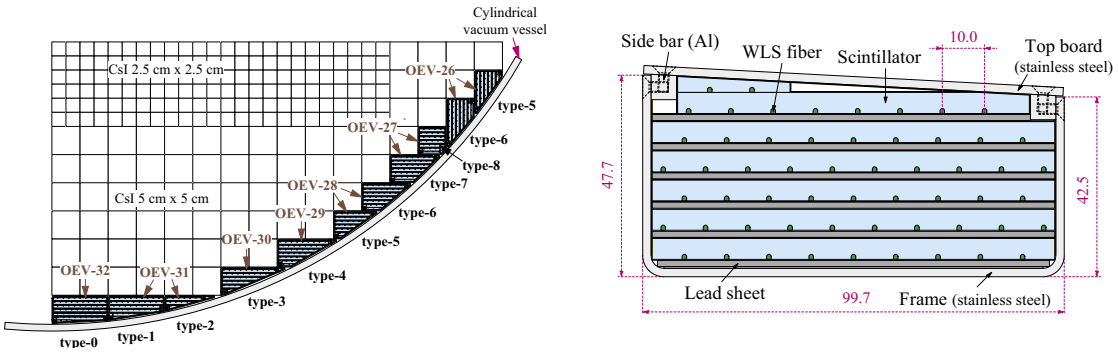

Figure 2.13: The OEV detector [37]. The left figure is the zoomed in view of Fig. 2.8. The right figure shows an OEV module.

2.3.8 Collar Counters (CC0X)

CC03

The CC03 detector is a collar counter located between the beam pipe and the regular small CsI crystals at the squared area of the CsI calorimeter, as shown in Fig. 2.12. The CC03 detector is made of undoped CsI crystals, with cross section of 45.5×18 mm^2 and length of 500 mm. It contains 16 modules. Details of the CC03 detector can be found in Ref. [38].

Downstream Collar Counters (CC04, CC05, CC06)

A series of collar counters (CC04, CC05, and CC06) are located around the beam hole, downstream of the CsI calorimeter. The purpose of these detectors are to detect photons and charged particles which escape in the downstream direction via the calorimeter beam hole. Each detector consists of a layer of scintillator upstream, followed by a stack of undoped CsI crystals downstream. Figure 2.14 shows the

illustration of the CC04, CC05, and CC06 detectors. The CC04 detector is located inside the vacuum tank while the CC05 and the CC06 detectors are located outside. Details of these detectors can be found in Ref. [40].

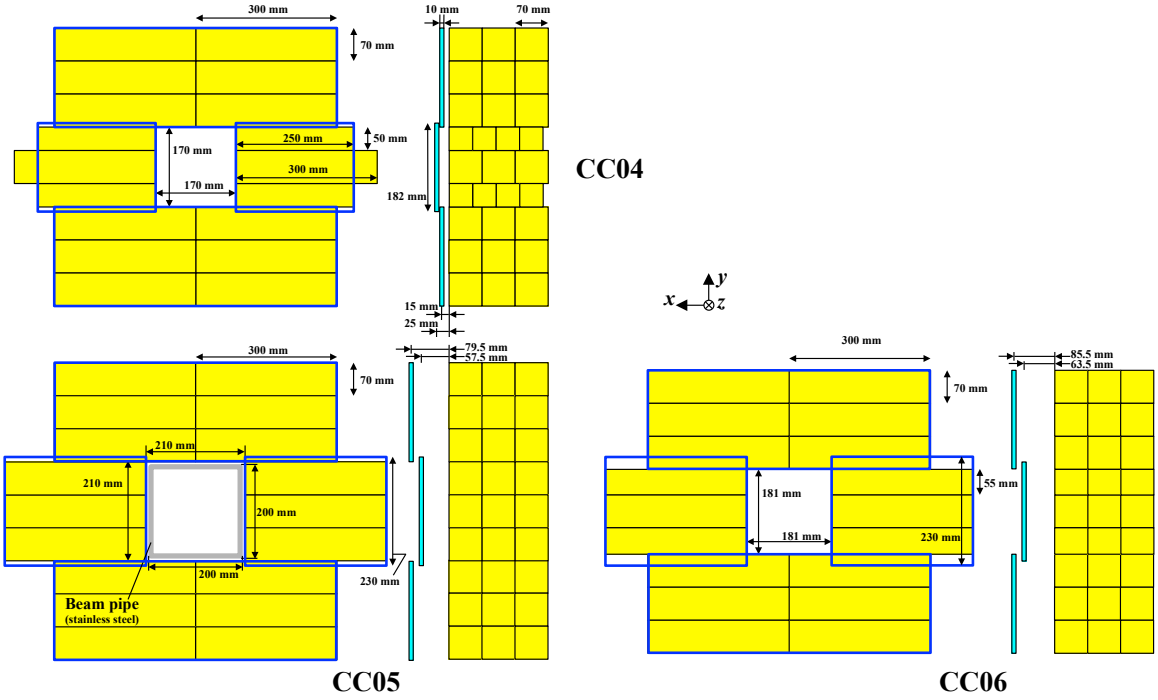

Figure 2.14: The CC04, CC05, and CC06 detectors [51].

2.3.9 Beam Hole Charged Veto (new BHCV)

The new beam hole charged veto (new BHCV) is located inside the beamline, behind the CC06 detector. The purpose of this detector is to detect charged particles that escape in the downstream direction. The new BHCV is a wire chamber made of three layers. A mixture of n-Pentane and CF4 gases was used as drift gas. Figure 2.15 shows the new BHCV detector structure. Details can be found in Ref. [41]. The old BHCV was not used in the 2015 analysis.

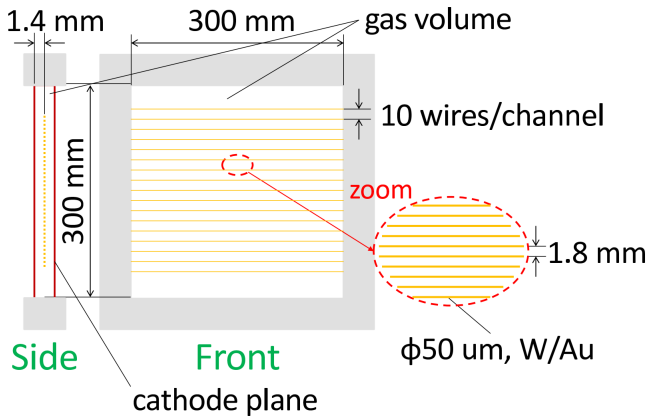

Figure 2.15: The new BHCV detector module [42].

2.3.10 Beam Pipe Charged Veto (BPCV)

The beam pipe charged veto (BPCV) detector is located between the CC05 and the CC06 detector. Its purpose is to increase the charged particle detection efficiency escaping downstream between the CC05 and the CC06 detectors, such as the charged pions from the $K_L \to \pi^+\pi^-\pi^0$ decay. It contains four modules, each on one side of the beam pipe with a dimension of 100×20 cm^2 and a thickness of 5 mm. Figure 2.16 shows the BPCV detector. Detailed information can be found in Ref. [43].

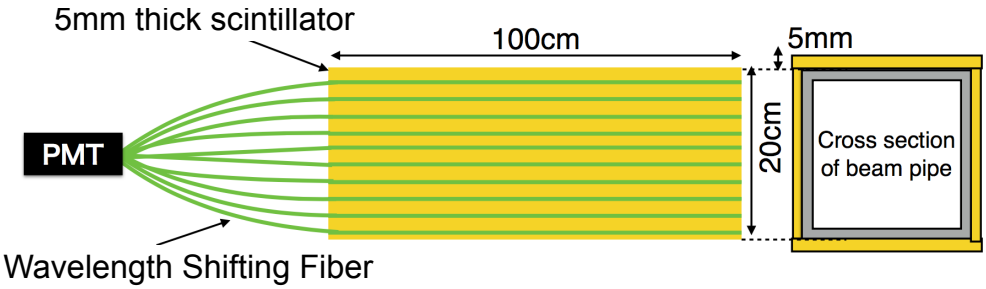

Figure 2.16: A BPCV detector module [43].

2.3.11 Beam Hole Photon Veto (BHPV)

The beam hole photon veto (BHPV) detector is located downstream of the new BHCV detector. Its purpose is to detect photons escaping down the beamline. The

BPCV detectors is a cherenkov detector, which consists of an array of 16 aerogel modules[1]. Figure 2.17 is an illustration of the BHPV detector structure. Detail information can be found in Ref. [44].

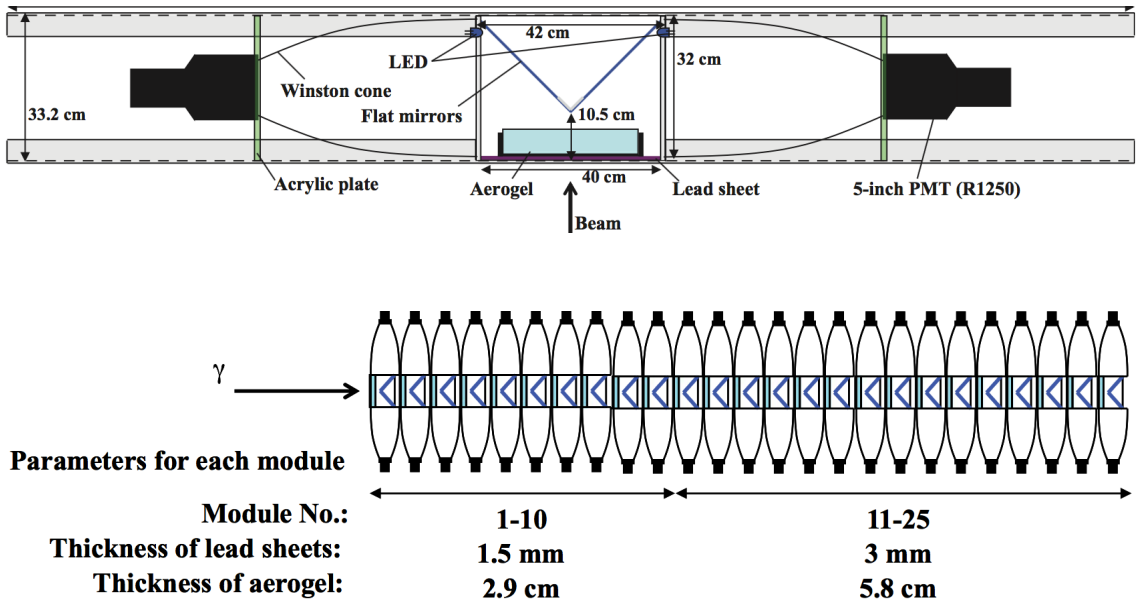

Figure 2.17: The BHPV detector modules [44]. The top figure is one BHPV module with dual-end readout. The bottom figure shows an array of the BHPV modules staked in downstream direction. The BHPV detector refers to the collection of the BHPV modules.

2.3.12 BHGC

The beam hole guard counter (BHGC) detector is located behind the BHPV detector array. The purpose is to detect the photons going through the edge region of BHPV. Each counter was 120 mm wide and 500 mm long. Figure 2.18 shows an illustration of the BHGC detector structure. Detailed information can be found in Ref. [45].

[1]Total of 25 modules are available, total of 12 modules were implemented in 2013 and total of 16 modules were implemented in 2015

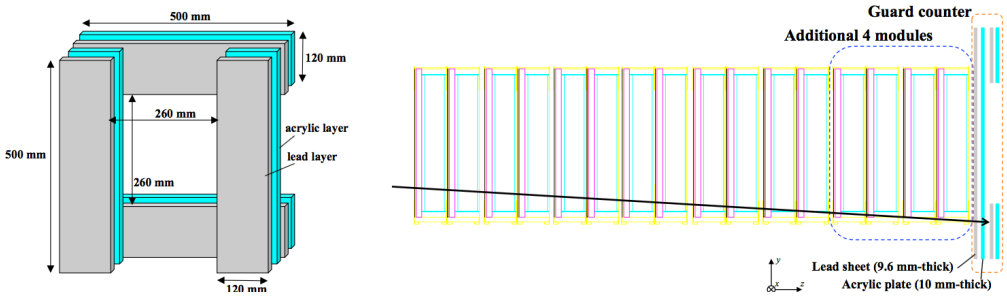

Figure 2.18: The BHGC detector [45]. The left figure shows the detector moduels. The right figure is in illustration of the detector configuration in the KOTO detector, placed behind the BHPV detector.

2.4 Vacuum System

To prevent interaction of the decaying particles with residual gas inside the decay region, a thin membrane is used to separate the decay region from the detector region. A vacuum level of 10^{-5} Pa is required to suppress these backgrounds. In the 2015, two vacuum levels were used. A high-vacuum area with 5×10^{-5} Pa (magenta line in Fig. 2.7, inside the decay region) and a low-vacuum area (orange line in Fig. 2.7, outside at the detector region) of 1 Pa were evacuated, respectively. Figure 2.19 shows the schematic view of the vacuum system in the KOTO experiment.

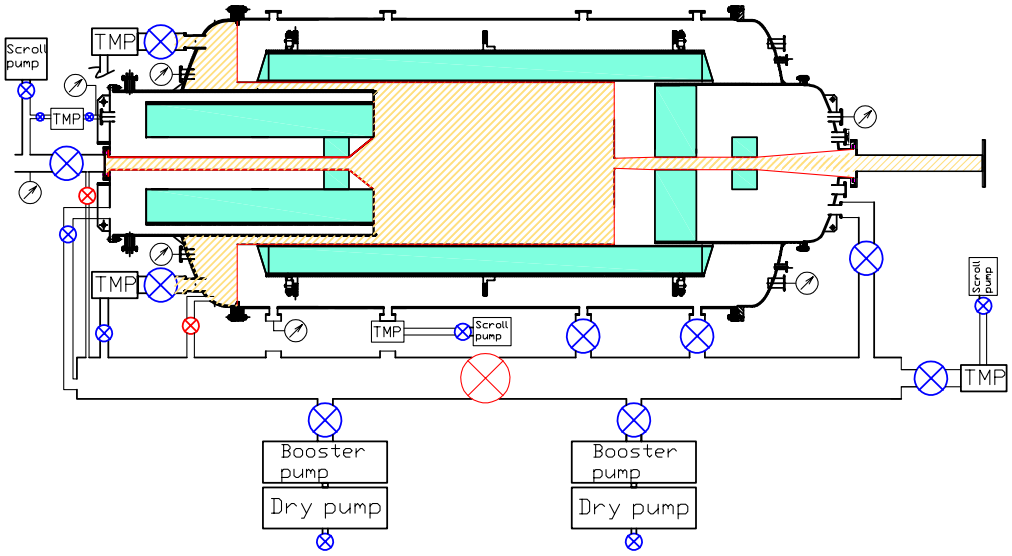

Figure 2.19: The vacuum system of the KOTO experiment. Membranes are denoted in red line. The red and blue $\otimes$ represent the closed and open valves, respectively.

Chapter 3
The Data Acquisition System

The KOTO Data Acquisition (DAQ) System serves the purpose to secure reliable data collection and to provide efficient trigger selections.

To achieve the statistics required for the sensitivity of $K_L \to \pi^0\nu\overline{\nu}$, one can spend decades collecting data with low intensity proton beam, or increase the beam intensity to increase statistics more rapidly. The KOTO DAQ system is designed to sustain high data rate that comes with high beam intensity. It must be able to process triggers with high throughput with minimum dead time and select relevant events from large amount of data. A DAQ system with good timing resolution is required to distinguish signals from accidental backgrounds and to make trigger selections accurately and efficiently. Hence, we designed a DAQ system with fast digitization and high dynamic range of the front-end signals, as well as three levels of triggers to fulfill these requirements. This chapter will focus on introducing the DAQ system used in the 2015 runs, which correlates to the main data set used in this thesis. The DAQ performance will be discussed in Ch. 4.

3.1 The DAQ Chain

The main components of the KOTO DAQ system and their functionalities to eliminate background decays while retaining the sensitivity to the signal events are listed as follows:

- The MAster Control and TRigger Supervisor (MACTRIS) - System Control

- Analog-to-Digital Converter (ADC) modules - Data Digitization
- Level 1 (L1) hardware trigger - Energy & Veto Cut
- Level 2 (L2) hardware trigger - COE Radius Cut
- Level 3 (L3) software trigger - Event Building.

Figure 3.1 shows the KOTO DAQ system chain in the 2015 runs. The MACTRIS board provides the system clock, controls the triggers, and oversees the DAQ system. The ADC modules digitize the detector analog signals for data processing and delivery to the L1 and the L2 triggers. The L1 and L2 triggers filters irrelevant events based on the physics characteristics of the $K_L \to \pi^0\nu\overline{\nu}$ signal decay. The L3 trigger is a computing farm that builds pieces of event fragments to complete events and store the data for future offline analysis. Data processing prior to the storage to disk (upstream of the L3 computing farm) is referred as "online". Conversely, analysis performed using the stored data files is referred as "offline" analysis.

3.1.1 Layout of the DAQ System

The KOTO DAQ schematics and layout are shown in Fig. 3.2 and Fig. 3.3. We use the UDP protocol for data passage prior to the L3 trigger system to establish rapid data transfer. To secure data quality after trigger selections, we use TCP/IP protocol for data delivery after the triggers enters the L3 trigger system. In the Hadron Hall, the ADC system is located inside the radiation area close to the detector. The optical fibers from the ADC modules and the control cables go through the concrete shielding and connect to the MACTRIS, the L1, and the L2 trigger systems located outside the concrete shielding blocks. The L3 trigger system is located inside the container room, outside of Hadron Hall. Ethernet converters for copper to optical fiber conversion are used for the data delivery between the L2 and the L3 trigger system due to the limitation on the Ethernet cable lengths. Details of each subsystem will be introduced in the following sections.

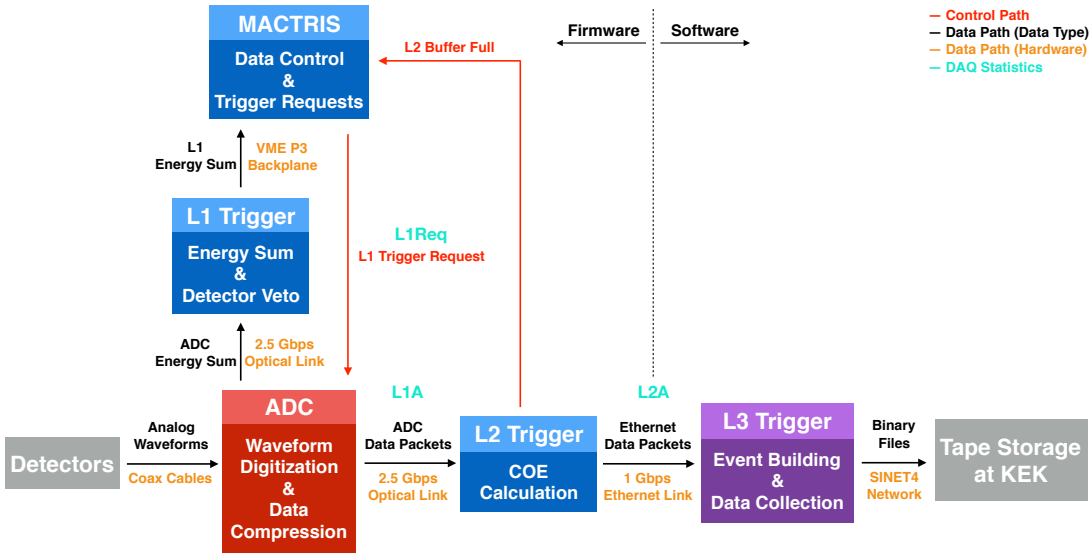

Figure 3.1: The DAQ system flowchart for the 2015 runs. Red arrows shows the system control signals paths. Black arrows indicate the data transfer paths and the transferred data type. Orange labels represent the connections for data passage between each stage of the DAQ system. Aqua green labels show the DAQ statistics used to measure the DAQ performance, which will be introduced in Chap. 4. The L1 trigger and the L2 trigger are hardware triggers. The L3 is designed to be a software trigger but only used as the function of a computing farm in the 2015 runs.

3.2 The MACTRIS Board and the Fanout System

The MACTRIS board is the central controller board that supervises the entire DAQ system. It has two important features: signal control and trigger decision making. There are two other flavors of the MACTRIS - the slave MACTRIS and the COE MACTRIS, where the different flavors of the MACTRIS is determined by jumpers and the firmware on the FPGA[1] on the board.

The MACTRIS generates three main signals for the DAQ system: the 125 MHz (8 ns) system clock, the L1 trigger decision (L1A), and the logic gate for data collection (LIVE). It is also capable of receiving error report signals (ERROR) from the ADC modules. These four control signals are distributed to the ADC system via the fanout system. The RJ45 control Ethernet port on the front panel of the MACTRIS

[1]Xilinx XC5VFX30T

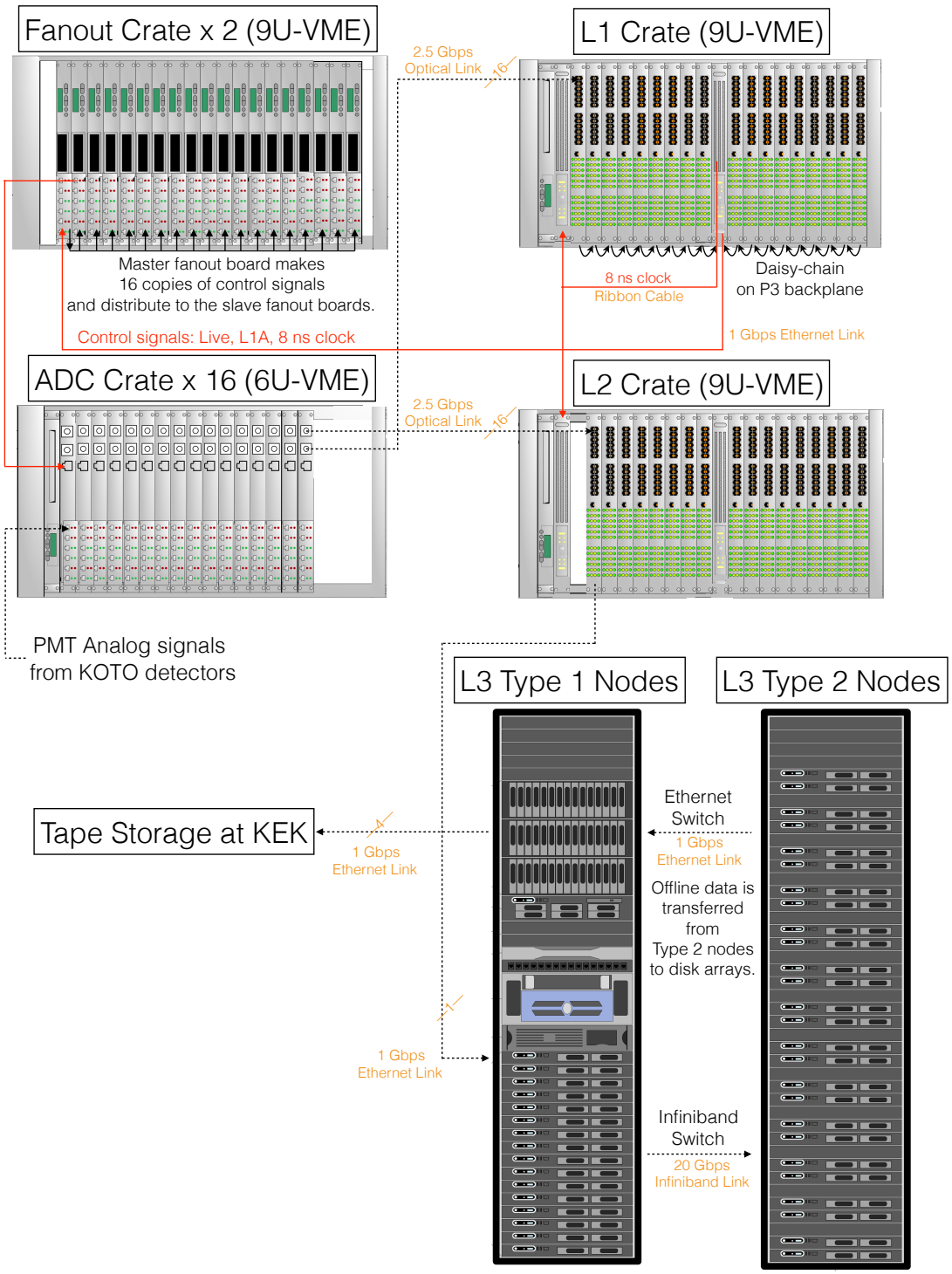

Figure 3.2: Schematics of the DAQ system for the 2015 runs. Red lines are the control signals. Black lines are the data paths. Orange labels indicates the connection links used for the signal or data passage.

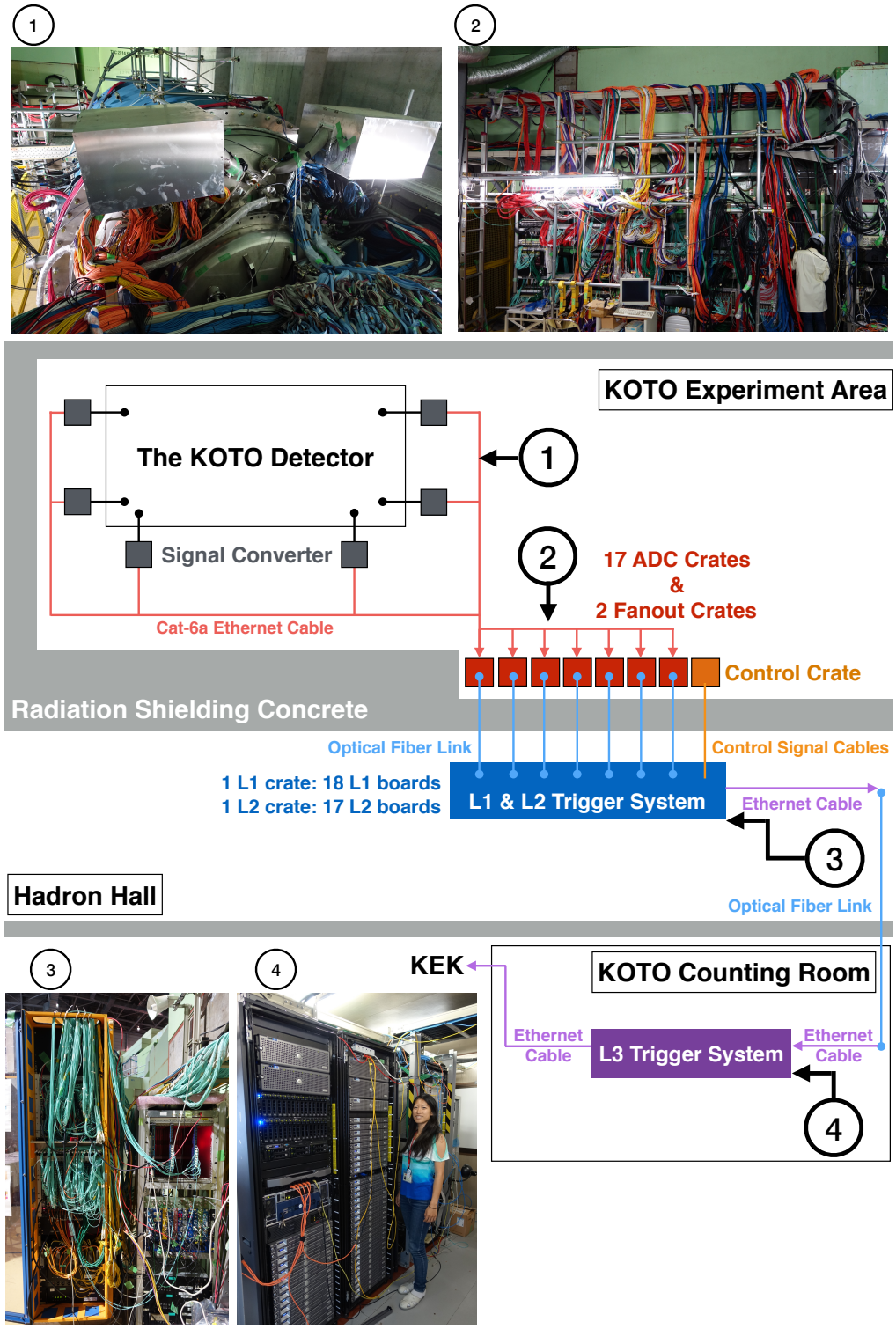

Figure 3.3: DAQ system layout on site in 2015. North side faces towards the top.

(Fig. 3.4) is connected to the Ethernet port on a master fanout board (Fig. 3.5), which produces 16 copies of the control signals. Each copy is fed into a slave fanout board to create 16 more copies. Each control signal created from a slave fanout board is outputted to an ADC board via a 20-feet Ethernet cable[1]. The same cable lengths are used to ensure the timing alignment across all trigger crates in the ADC system.

Figure 3.4: The front panel of the MACTRIS board. The 8 ns system clock is connected to the Slave MACTRIS in the L1 and the L2 trigger crates via the CHIE ports. The Ethernet port is used to pass on the control signals to the fanout system and to the ADC modules. The LVDS ports are used to receive spill gate and external trigger signals.

The 8 ns system clock, designed to drive the 125-MHz ADC boards, is also delivered to the L1 and L2 systems via 68-pin[2] flat ribbon cables at the front panel to synchronize the data handling in the DAQ firmware system. Each 34-pair flat ribbon cable is connected to the slave MACTRIS boards in slot 2 of the L1 and in the L2 trigger crates. The slave MACTRIS redirects the signals received via the ribbon cable to all of the trigger boards in the crate via the VME P2 backplane bus lines. In the L2 crate, the slave MACTRIS also delivers the system clock to the COE MACTRIS through the front panel ribbon cable.

[1]Category-6A (Cat-6A)
[2]32×2 pins

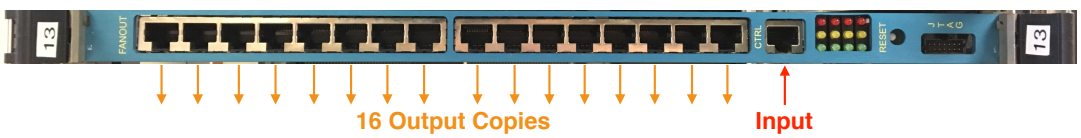

Figure 3.5: The front panel of a fanout board. Each fanout board can create 16 copies of signals.

The MACTRIS board and the COE MACTRIS board are located at the middle slot of the center of the L1 and the L2 trigger crate respectively. They are in charge of L1 and L2 trigger decision making based on the information received from the VME P3 backplane. The L1 trigger system is synchronous to the 8-ns clock and does not generate any dead time. The L2 trigger system is asynchronous, where triggers are received at non-fixed clock time and can generate dead time due to limitation in the buffer resource. Therefore, in data passage, the MACTRIS checks the available buffers in the L2 trigger before issuing a L1 trigger accept (L1A). If it receives a L2 buffer full signal, the MACTRIS will not send out the L1A to prevent data clog and ensure safe data recording.

3.3 ADC Module

The output signals from the PMTs connected to the detectors are analog. To analyze the waveform information and make trigger decisions during the high rate online data recording, waveform signal digitization are performed. To reduce the electronic noise throughout the cable transmission from detectors to the ADC modules, analog PMT signal outputs except for the CsI calorimeter, CV, BHPV, and detectors implemented in 2015 (new BHCV, BPCV, and BHGC) were converted from 50 Ω single ended signals to 100 Ω differential signals to match the ADC board design. These detectors already have differential signals from the twisted pairs thus no need to be converted and we use two shielded twisted pairs in each Cat-6A Ethernet cable to transfer the analog signals from these detectors. The signal converters are located around the KOTO detector, as shown in Fig. 3.3. The cable lengths varies depends on the location of each detector. The timing delays due to different cable lengths are adjusted in the FPGA[1] firmware on the ADC boards.

We designed two types of ADC boards for different detectors to meet the resolution requirement due to different counting rates. A detector located inside the beamline encounters higher interaction with the beam compare to a detector outside

[1] Analog Devices AD9254

Table 3.1: Detector channels and the ADC modules used in the 2015 runs.

Detectors	Number of Channels	ADC Modules		Number of Converters
		125-MHz	500-MHz	
FB	32	2		4
NCC	204	13		26
MB	128	8		16
BCV	64	4		8
CV	184	12		
CsI	2716	176		
LCV	4	1		1
OEV	44	3		6
CC03	32	2		4
CC04	64	4		8
CC05	64	4		8
CC06	64	4		8
old BHCV (not used)	8		2	
new BHCV	48		12	
BPCV	8	1		
BHPV	32		8	
BHGC	8		2	

the beamline, thus require a high data sampling rate. One design of the two types of ADC boards is a 14-bit ADC with 125 MHz sampling rate and the other is a 12-bit ADC with 500 MHz sampling rate. In the 2015 runs, total of 4192 detector channels were connected to the ADC boards and 16 6U VME crates were used. A list of detector channels and the corresponding ADC modules used are included in Table 3.1. Pictures of a 125-MHz ADC and a 500-MHz ADC are shown in Fig. 3.6.

3.3.1 A 14-bit 125-MHz ADC

Most of the detectors use the 14-bit 125-MHz ADC modules. Figure 3.7 shows the schematics view of the 14-bit 125-MHz ADC module. The 125-MHz ADC boards shape the incoming analog waveform into Gaussian-like waveform then digitize them synchronously at a sampling rate of 8 ns, provided by the MACTRIS system clock. Figure 3.8 illustrates the transformation of an analog waveform. The leading edge of the analog waveform is too fast to collect the necessary information using an 8-ns sampling rate. To improve the timing resolution, we introduced a 10-pole Bessel filter

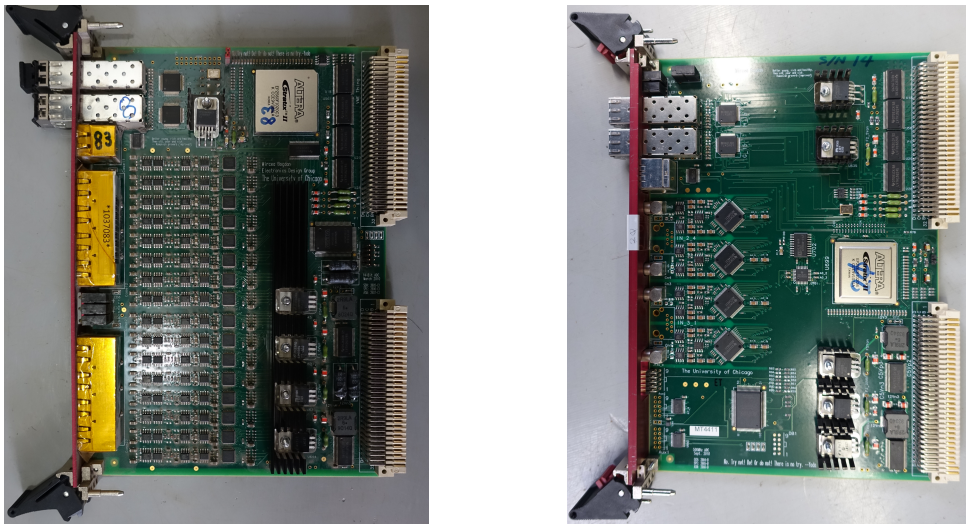

Figure 3.6: Pictures of the ADC boards. The left is a 125-MHz ADC board and it can take up to 16 channels of detector PMT signals via Ethernet cables. The right is a 500-MHz ADC board and it can take up to 4 channels of detector PMT outputs via LEMO cables.

to shape the pulse into a Gaussian waveform with $\sim$ 40 ns FWHM[1].

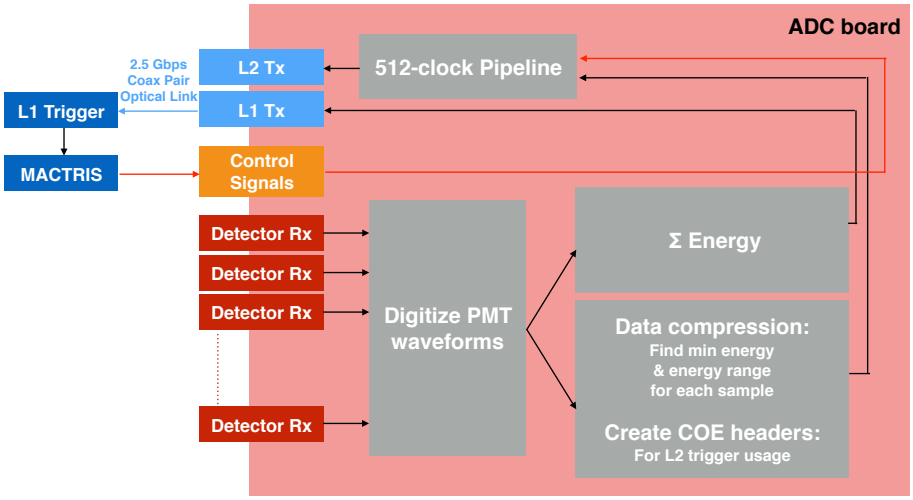

Figure 3.7: ADC firmware logic. There is a 5-clock (clk) delay in each L1 board for trigger calculation. The total L1 trigger calculation takes 30 clk cycles (240 ns). The 512 clk pipeline buffer is sufficient to intake triggers during the L1 trigger selection.

[1]Full width at half maximum. See Appx. C.

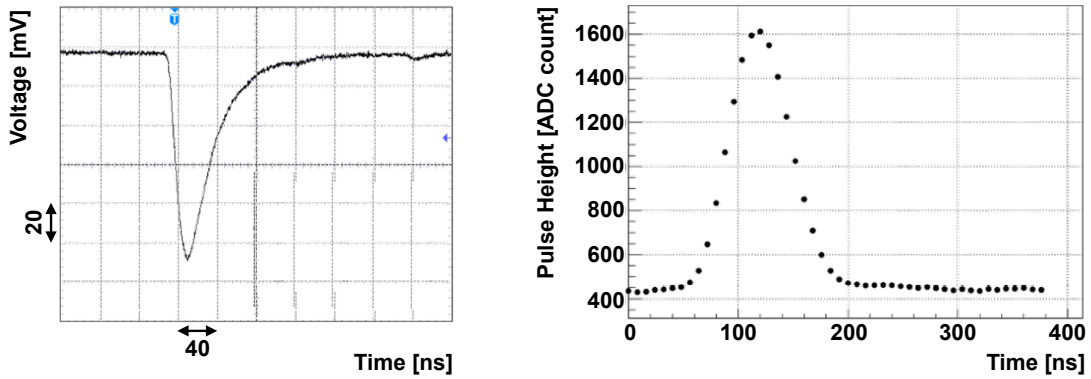

Figure 3.8: Digitization of an analog waveform. The left figure is the signal of the detector PMT output collected on the oscilloscope and it has a sharp edge. The right figure is the waveform after digitized by the ADC.

The digitized waveform is sent to the FPGA[1] on the ADC boards where the signals from up to 16 channels are corrected for cable delays and aligned to the K_L beam pulse [46]. The ADC processes the digitized waveforms and sends them to the L1 and the L2 triggers via optical fibers at 2.5 Gbps rate. The top port of the ADC module is configured to deliver data packets to the L2 trigger system and the second port is configured to deliver energy sum information to the L1 trigger system.

Two processes are carried out in parallel inside the FPGA. The energy sum of the waveforms are calculated and sent to the L1 trigger for trigger decisions. Meanwhile, a lossless compression[2] algorithm is used to reduce the data size for downstream DAQ data transmission and storage. The uncompressed data packet goes into a 512 clock-wide ($\sim 4\,\mu$s) pipeline, which is used to reduce the DAQ dead time, for the L1 and MACTRIS trigger decision. The data coming out from the pipeline is compressed and saved to a memory before being sent to the L2 trigger or ignored.

3.3.2 A 12-bit 500-MHz ADC

Due to the direct interaction with the beam, detectors located inside the beamline or around the beam hole such as BHCV, BHPV, and BHGC have higher event rate

[1] Altera StratixII EP2S60F1020

[2] The lossless compression will be discussed in Sec. 3.6.1.

compared to other detectors outside of the beamline. We use ADC modules with faster sampling rate to support the high counting rate. A 4-channel 500-MHz ADC module with 2 ns sampling rate is fast enough to capture the sharp falling edge of the waveform without any analog waveform shaping. The remaining features of data handling in a 500-MHz ADC module is identical to that of a 125-MHz ADC module.

3.4 Level 1

The L1 trigger uses the CsI energy and veto signals to eliminate unwanted events. In the signal of $K_L \to \pi^0\nu\overline{\nu}$ decay, we require both photons to hit the CsI calorimeter and no hits in the veto detectors. Therefore, the L1 trigger selection is determined by requiring a minimum energy (Et) sum of 550 MeV on the CsI calorimeter and no activity on the veto detectors[1]. The veto detectors considered in the L1 trigger decision were NCC, CV, MB, and CC03.

Each L1 trigger board receives the energy sum from up to 16 ADC boards and calculates the partial energy sums from all its inputs. There is a three to five-clock delay before passing the partial energy sums to its neighboring L1 board via the P3 VME backplane in a daisy-chain fashion. The neighboring L1 board adds the received energy sums information from both its ADC inputs and that from the another L1 board and pass on to its neighboring board towards the center of the crate, as shown in Fig. 3.9. The daisy-chain sum starts from the outer L1 modules and moves towards MACTRIS, where the total energy sums over the full CsI calorimeter and the veto detector energies are calculated. The MACTRIS makes the trigger decision, L1 Accept (L1A) and send it to the ADC modules.

[1]The ADC count to energy conversion is performed by matching the integrated area underneath the waveform (ADC counts) to known energy (MeV).

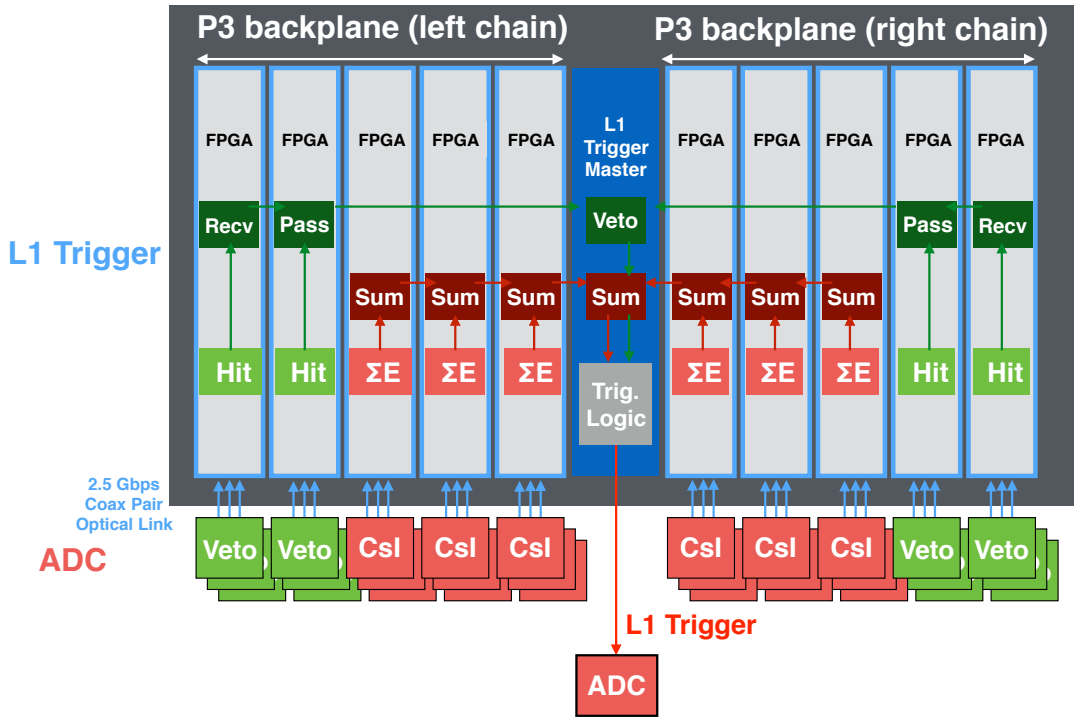

Figure 3.9: The L1 trigger data flow chart. Talk about the fiber connection 2.5 Gbps optical link.

3.5 Level 2

Another characteristic a $K_L \to \pi^0\nu\overline{\nu}$ decay processes is a large transverse momentum of the π^0 due to the missing neutrinos. The L2 trigger uses this property to distinguish possible $K_L \to \pi^0\nu\overline{\nu}$ decays from other K_L decay modes by placing a Center-of-Energy (COE) radius cut on the events. The COE radius is calculated using photo energies weighted by their positions on the CsI calorimeter, as shown in Eq. 3.1, where each i represents a CsI crystal. The larger the COE radius, the more likely that there are missing particles in the final decay product. Figure 3.10 and Fig. 3.11 shows the COE radius distribution on several K_L decay backgrounds that are sensitive to the COE radius selection. We apply the COE radius cut at 165 mm in the L2 trigger selection.

$$\text{COE online radius} = \frac{\sqrt{\left(\sum_i E_i x_i\right)^2 + \left(\sum_i E_i y_i\right)^2}}{\sum_i E_i} \tag{3.1}$$

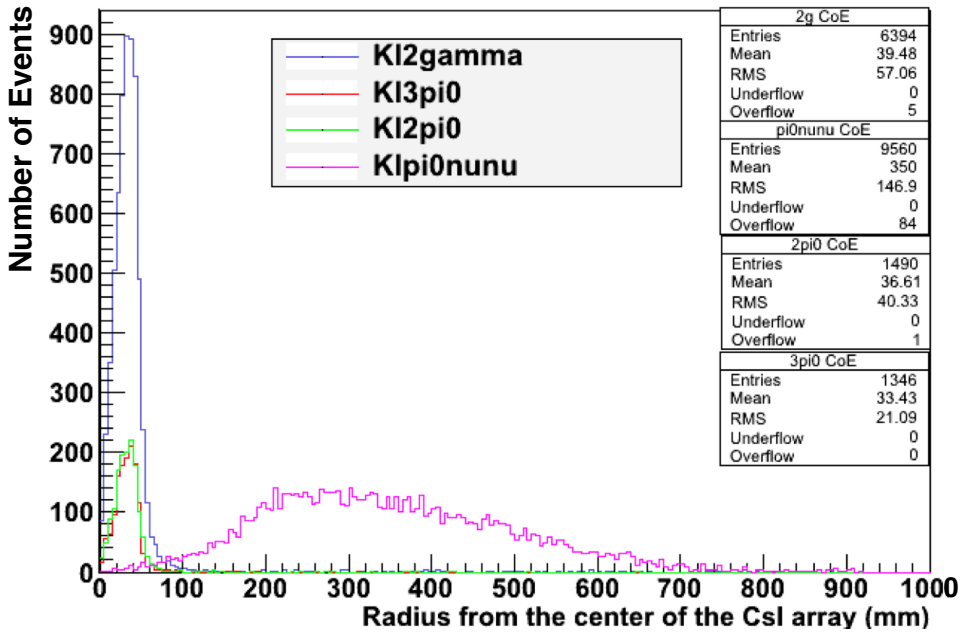

Figure 3.10: COE Distribution of neutral K_L decays. Decays without missing final particles ($K_L \to 3\pi^0$, $K_L \to 2\pi^0$, $K_L \to 2\gamma$) have lower COE distributions compare to decays with missing final particles ($K_L \to \pi^0\nu\bar{\nu}$).

The L2 trigger hardware shares the same design as the L1 trigger hardware. Figure 3.12 shows the data flow in the L2 trigger system. The ADC modules send compressed trigger data from the memory to the L2 trigger based on the L1A issued from MACTRIS. Each L2 board receives data packets from up to 16 ADC channels, stores them in a First-In-First-Out (FIFO) buffer, and calculate the total COE radius event by event[1]. Similar to the energy summing in the L1 trigger, the L2 trigger uses the VME P3 backplane daisy-chain to calculate the COE radius. Part of the COE radius was calculated inside the ADC firmware. The final COE radius is evaluated and received by the COE MACTRIS. The COE MACTRIS, located at the center of the L2 crate, makes the L2 trigger decision by placing a COE radius cut on the triggers, then issue the trigger decision to all L2 boards via the VME P2 backplane.

[1]Processed by the Vertex 5 XC5VFX70T Xilinx FPGA

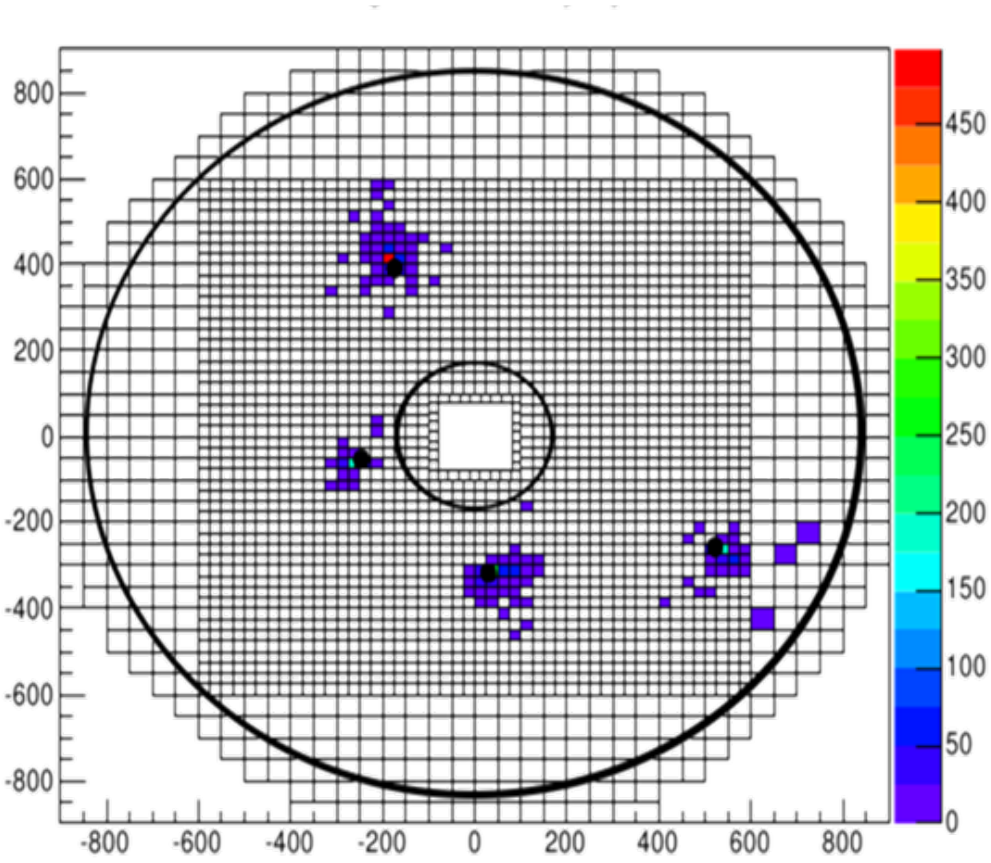

Figure 3.11: Event display on the CsI. The $K_L \rightarrow 2\pi^0$ decay yields four photons. There is no missing final particles hence the photon distributions are symmetric around the beamline.

Each L2 board either discards or reads out an event from the FIFO to a 2 Gb DDR2 on-board memory after the L2 trigger decision[1]. Events stored in the DDR2 memory will be read out to the L3 trigger in the next spill. We toggle events read-out and write-in between the two DDR2 memories for each spill to prevent overwriting events.

The COE radius is calculated one event at a time. During the calculation, each L2 board tracks the available buffer inside the FIFO and send a signal to the MACTRIS if there is not enough space to store the incoming triggers. The MACTRIS will stop issuing L1A if it receives the buffer-full signal from any L2 trigger board and resume when the buffer-full signal clears. Limitation of the L2 FPGA resources to allocate sufficient buffer space for receiving incoming triggers and the available DDR2 memory

[1]Processed by the Vertex 4 XC4VFX12 Xilinx FPGA

for storing data are the bottleneck of the L2 trigger system [47]. The compression of data inside the ADC greatly reduced the effect of the bottleneck and decreases the dead time generated when MACTRIS had to stop issuing L1 trigger accepts.

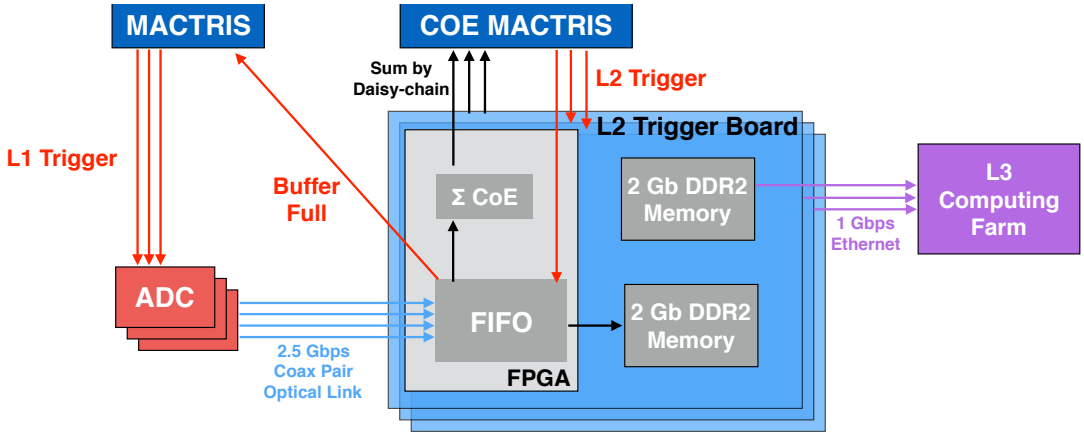

Figure 3.12: L2 trigger data flow.

3.6 Level 3

Data prior to reaching the L3 trigger are not collected into events. The trigger selections we can make with the event fragments are limited. To advance to the next level of trigger selection, a picture of a complete event is required. The L3 trigger is a computer cluster system, designed to accommodate software trigger selections. It is in charge of data collection, event building, online data analysis, and data structure rearrangement for offline storage.

The L3 computer cluster system, named "Banjo", consists of two head nodes (banjo and banjo-1)[1] and 47 worker nodes (banjo01-banjo47)[2]. Each computer node has two processors and eight CPU cores. The head nodes each has 8 TB storage[3] and a worker node has two 4 TB hard disks. The head nodes oversee and manage all the worker nodes. The 47 worker nodes are categorized into 17 Type 1 nodes and

[1] Dell 2950
[2] Dell 1950
[3] 2 TB RAID 1 system disk and 6 TB RAID 5 local disks.

30 Type 2 nodes. The Type 1 nodes receives data from the L2 boards and send them to the Type 2 nodes for event building and data processing. The Type 2 nodes build events, analyze the data, compress data packets, and save them to disks. The collected data files are further transferred from the local disk storage to the permanent tape storage[1] at KEK. Beyond the 4 TB storage on each worker node, the L3 computer system offers 18 stages of 16 TB RAID 5 disk array, which gives total of 384 TB local disk storage[2]. Figure 3.13 shows the data flow in the L3 trigger system and Fig. 3.14 is the L3 hardware system.

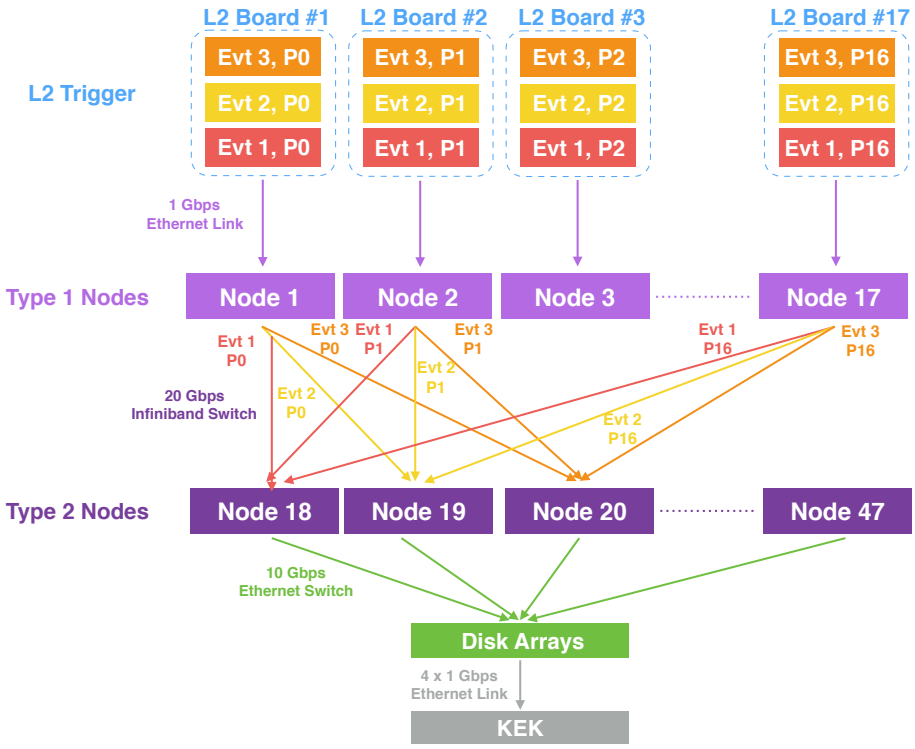

Figure 3.13: The L3 data flow.

The L3 computer system uses two types of networks to create mesh communication: the Ethernet network and the Message Passing Interface (MPI) network. The control signals use the Ethernet network and the data transmission uses the MPI network with the Infiniband hardware. Each computer node has a 10 Gbps Ether-

[1]Cassette tape storage is used due to its durability compared to the hard disks.

[2]This number of disk array stages and storage are doubled in summer 2015 between Run 63 and Run 64.

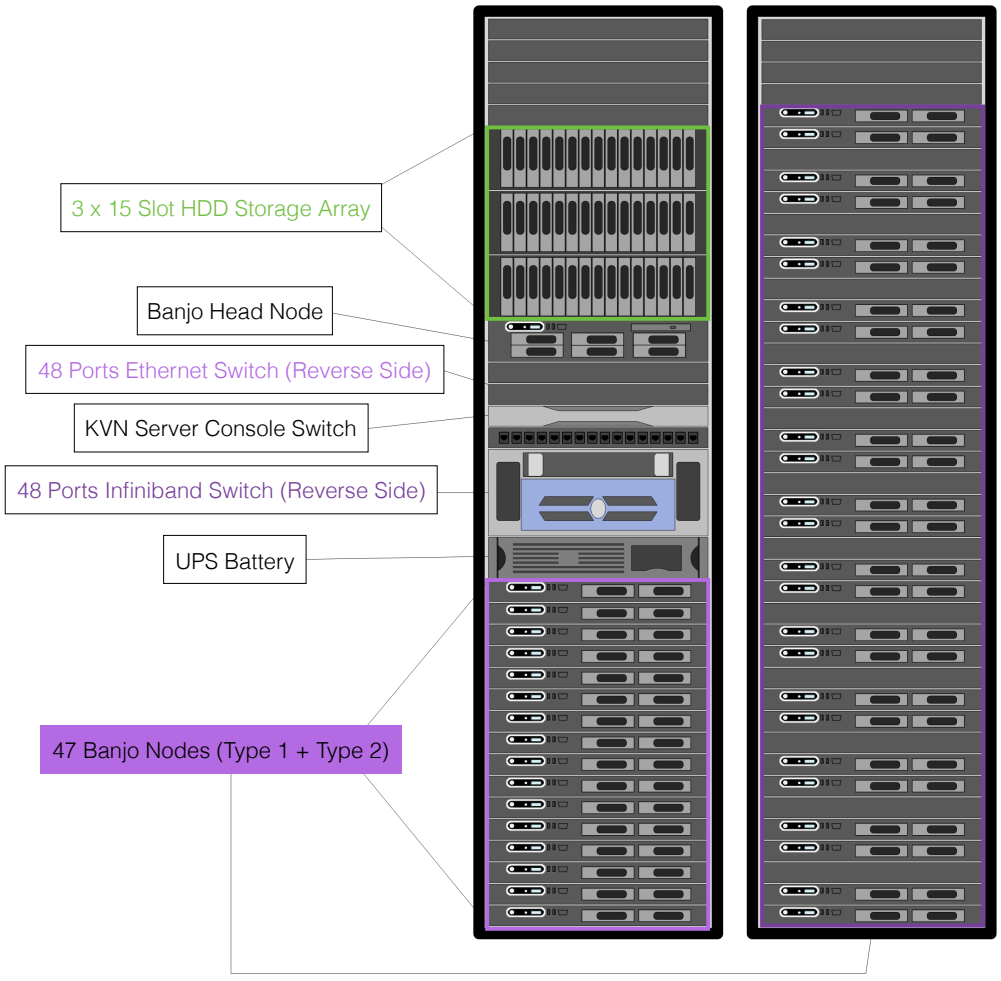

Figure 3.14: The L3 hardware system.

net connection to the Ethernet switch and a 20 Gbps Infiniband connection to the Infiniband switch. The switches are the backbone for the L3 trigger system as they provide direct communication between any computer nodes within the network.

To optimize high rate data processing, we take advantage of the computer nodes multi-core capabilities and use the MPI protocol to develop a multithreading MPI algorithm able to parallel process each task in the L3 trigger system. In addition, we use the Real Time Red Hat Linux operating system for all the computer nodes to prioritize our data processing tasks.

The L3 trigger system uses little-endian as the data packaging style. Each L2

trigger board is directly connected to a L3 Type 1 node. The L2 board sends event fragments to the Type 1 node using Ethernet UDP protocol for fast data collection. Each Type 1 node sends the event fragments to the designated Type 2 node using the unique spill and event ID information for event building. This process uses the Infiniband connection with the MPI network and the TCP/IP protocol to secure data delivery. The Type 2 nodes arrange the event fragments received from all the Type 1 nodes and build complete events. After events are built, the Type 2 nodes decompress the ADC-compressed data in order to further analyze the events, make trigger selections, and rearrange data structure for offline analysis. Data analysis subjected to the interests of data collection and trigger selections[1] are made followed by the data decompression. A lossless data compression algorithm is used to reduced event sizes for the disk storage prior to saving the data. Details of the algorithm will be discussed in Sec. 3.6.1. Data files saved on each Type 2 nodes are copied to the disk array stages and transferred to KEK via 4 Gbps SINET4 network[2], then removed after the data quality check on the transfer to KEK is secured. The format of the data files is binary. These raw data go through data production in KEK computer clusters and turn into ROOT format for offline analysis.

The difficulty of searching a rare decay cannot be stressed enough. The amount of data and its quality is especially vital. In the L3 computer system, different stages of online data quality check are implemented in the Type 1 nodes, the Type 2 nodes, and the online monitor to secure data integrity during the data collection.

3.6.1 Lossless Data Compression

The KOTO experiment collects vast amount of data to probe for a rare decay. The beam intensity increased from 24 kW in 2013 to 42 kW in 2015. The major bottleneck for the increasing trigger rate is the limitation on the available firmware logic buffers and the on-board memory storage in the L2 trigger. To maximize the

[1]This feature is not used until Run 74 in 2017.

[2]Science Information NETwork (SINET) is Japanese academic network for universities and research institutes.

data collection with limited resources in the trigger system and the offline disk storage, besides making effective trigger selections, we can reduce the data size. To find the middle ground between reducing the data size and keeping the full data content, a lossless data compression algorithm is desirable.

A lossless compression, in contrary to a lossy compression, is a data compression algorithm that allows the original data to be perfectly reconstructed from the compressed data. We use a bit-packing lossless compression algorithm in the L3 trigger to reduce event sizes. The compression algorithm encodes the data packets into a 16-bit word, with the last two bits reserved as headers for data type information, and arranges the compressed data by detector channels. For every detector channel, we record the minimum and maximum energy value among the 64 waveform sampling, the maximum number of bit-range required to store the energy difference in each sample to the minimum energy, and the individual difference in all 64 samples to the minimum energy. The bit-packing compressed data is arranged waveform by waveform with this corresponding sequence for the convenience of offline data analysis. This data compression method is implemented in the ADC firmware logic and the L3 algorithm but with different arrangement of waveform information. The ADC firmware organizes the data by waveform sample rather than by detector channels to maximize the data processing speed inside the firmware. There are more resources in the L3 computer system. Hence, we rearrange the data sequence by detector channels (all 64 channels from a complete waveform by waveform) after the decompression and analysis of the events.

3.7 Upgrades of the DAQ System

To anticipate future increasing beam power and to expand studies in the KOTO experiment, a series of upgrades in detectors and the DAQ system has been proposed or carried out beyond the 2015 runs.

We needed to expand the DAQ system to accommodate new detectors. The MACTRIS+, a new version of the MACTRIS, was implemented in the 2016 to collect

DAQ statistics and to include new detector channels in the DAQ system. A Clock Distribution and Trigger processor (CDT) hardware was added in 2017 to expand the varieties of trigger selections we can make. An upgrade of the L2 trigger system, the Reconfigurable Clustering Element (RCE) Platform Technology, is under development in preparation for data collection with beam power beyond 100 kW.

3.7.1 The MACTRIS+

A new detector, the Inner Barrel (IB), was added to the KOTO detector in June 2016 (Run 69). To include the IB in the DAQ system, we replaced the MACTRIS with the MACTRIS+, which expands the hardware connections to the DAQ system. Furthermore, the MACTRIS+ has the ability to collect and output DAQ statistics for more performance studies. A 32-channel fanout board was also added to provide more control signal connections for the new detector channels. Figure 3.15 is the picture of the MACTRIS+.

Figure 3.15: The front panel of the MACTRIS+. It provides up to four ribbon cable connections to the trigger crate. The current usage is for two L1 crates and one L2 crate. The extra Ethernet port is used to output DAQ statistics.

3.7.2 CDT Trigger

The CDT hardware was added to the DAQ system in April 2017. It uses cluster information on the CsI calorimeter to provide versatile trigger selections on the number of clusters. The new DAQ system flow chart is shown in Fig. 3.16. The scattered

K_L study[1] in this thesis uses data recorded from the CDT in the 2018 runs.

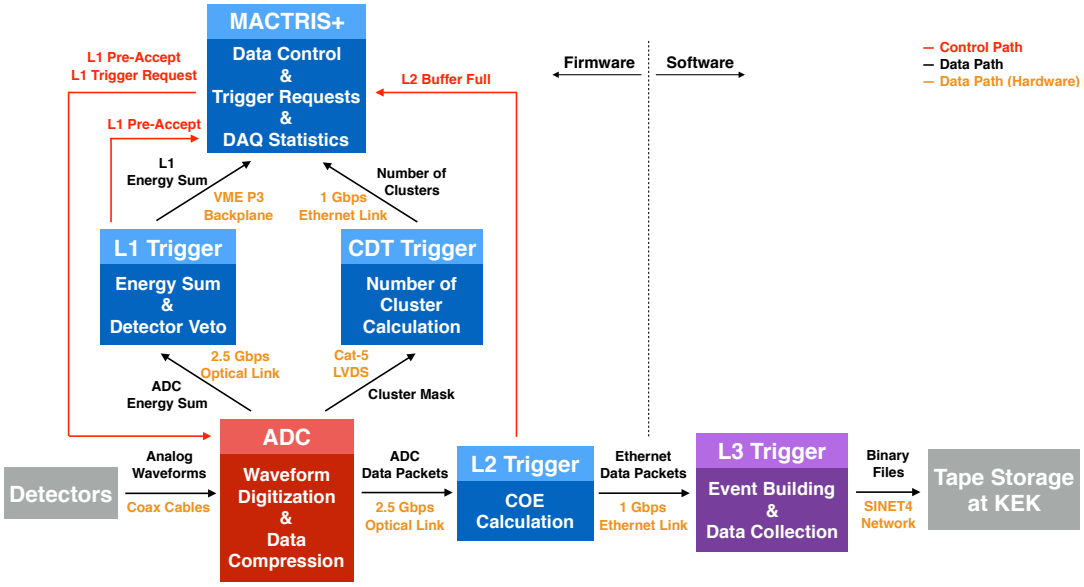

Figure 3.16: CDT DAQ flow chart.

3.7.3 RCE Platform Technology

We designed and constructed a reliable DAQ system for the KOTO data collection. With the increasing beam power, upgrades of the hardware are necessary to sustain the high rate data processing. The data rate projected for 100 KW beam power will highly affect the efficiency in the L2 trigger system. We were able to release the stress on the L2 buffers and the on-board memory resources by using lossless data compression. To resolve the challenges beyond 100 kW beam, we are upgrading the hardware in the L2 trigger system with the RCE Platform Technology (RPT).

The RPT was developed by SLAC [48]. The layout of the RPT hardware is shown in Fig. 3.17. It uses two types of board - a Cluster-on-board (COB) and a Rear Transition Module (RTM). An ATCA shelf is used to contain the RPT hardware where the COB is inserted at the front of the ATCA shelf and the RTM at the rear. The RTM is designed to receive data from a generic experiment and present it to the

[1] See Ch. 8.

COB via a 600-pin connector [1]. The COB is where the data processing take place. It contains five mezzanine boards - four Data Processing Modules (DPM) and one Data Transport Module (DTM). Each DPM has two RCEs and the DTM has one. A RCE is composed of a Zynq-7000 series Xilinx FPGA[2], a 1 GB micro SD card, and an ARM processor with Linux operating system. The on-board processors grant us more controls to the system remotely compare to the current L2 trigger system. The communications between the RCEs are routed through the Cluster Interconnect (CI) Ethernet switch. The CI has four lanes of 2.5 Gbps Rx/Tx pair connection to each RCE on the board and eight lanes of 2.5 Gbps Rx/Tx pair to the P2 backplane. It is the hub for the intra-board and the inter-board data transport. Furthermore, we use an ATCA shelf with mesh-backplane to mimic the current L3 trigger system. The Intelligent Platform Management Controller (IPMC) signal is used to monitor the COB status through the P2 backplane. Figure 3.18 is an illustration of the RPT block diagram. Each lane is a pair of 2.5 Gbps link.

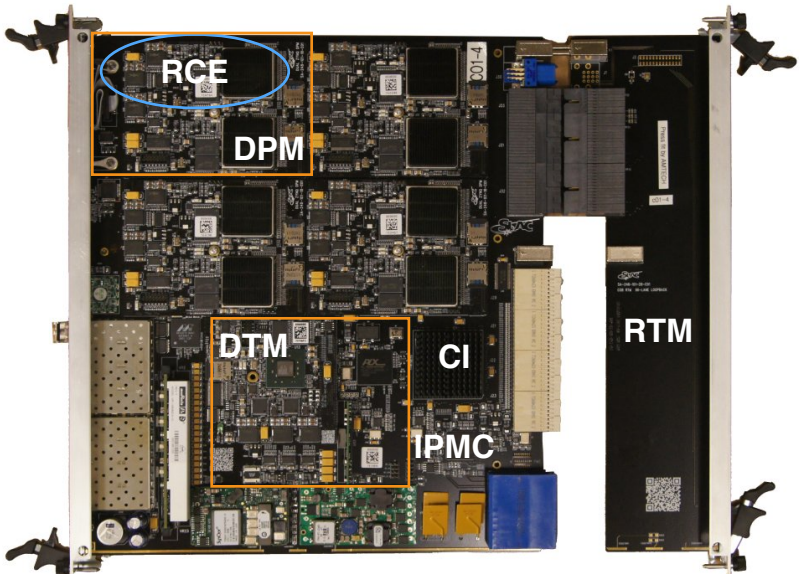

Figure 3.17: The RPT hardware layout. It consists of a COB (left) and a RTM (right). The mezzanine modules on the COB are removable and can be customized.

[1] 40×15 pins
[2] DPM RCE uses Zynq-7030 and DTM RCE uses Zynq-7045.

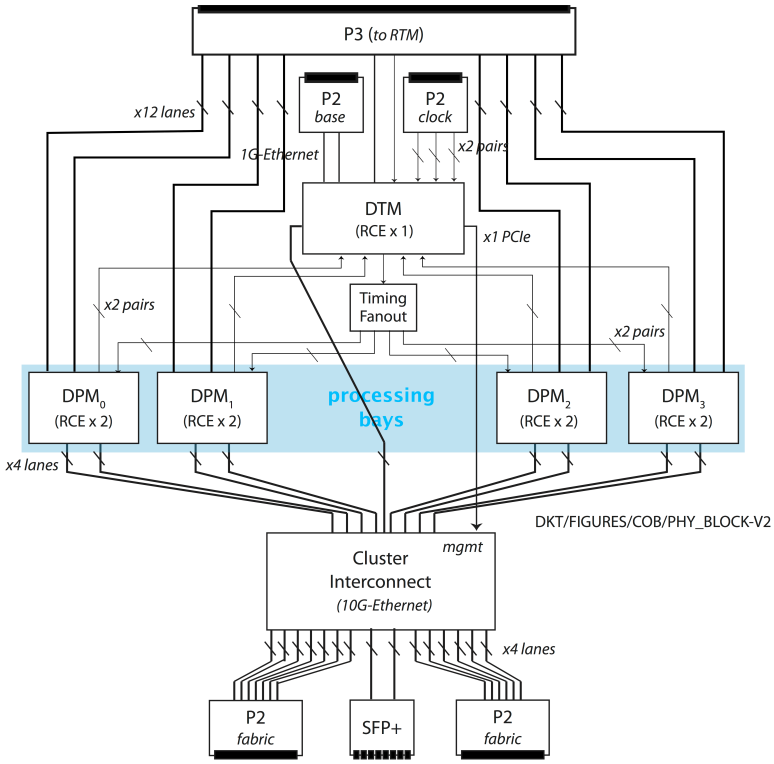

Figure 3.18: Block diagram of a COB. Each lane is a 2.5 Gbps Rx/Tx pair.

The COB supports Rx/Tx link with input/output rate up to 120 Gbps per RCE (12×10 Gbps link). Each RCE has 12 Rx/Tx transmission to the RTM. With the RPT hardware upgrade, we are able to contain all the detector information using a 6-slot ATCA shelf. The RPT with the mesh-backplane of the ATCA shelf creates a hardware mimicking of the software L3 trigger system. With more powerful computing power and resources available, we plan to move the event building from the current L3 trigger system onto the new L2 trigger system.

Each RCE will simultaneously serve as a Type 1 node and a Type 2 node in the current L3 trigger system. Eight out of the 12 links on each RCE will be dedicated to receiving data from the ADC modules from the RTM, one link will be used to transmit built events to the a L3 worker node. Each RCE serializes the received ADC data packets and sends it to the designated RCE via the CI and the ATCA P2 backplane using the current event building method with TCP/IP protocol. Trigger decisions on the COE or other potential cuts can be applied after event building and prior to

Table 3.2: DAQ System Timeline. Precise duration on the operation cycles and the beam power is in Table 4.1.

Run	Beam Power	Date	Comments
62	24 kW, 27 kW	04/2015	
63	27 kW, 29 kW, 32 kW	06/2015	
64	32 kW, 39 kW	10/2015	Added ADC compression, banjo-1, and nine more disk arrays
65	39 kW, 42 kW	11/2015	
69	44 kW	06/2016	Added MACTRIS+ and a 32-channel fanout board
74	45 kW	04/2017	Added CDT
75	37 kW	06/2017	Implemented CDT trigger cut on number of clusters and a L3 trigger cut
78	50 kW	01/2018	Implemented CDT veto on the veto detectors
80	50 kW	06/2018	

data transfer to the L3 trigger system. By moving the event building upstream in the DAQ system, we can dedicate the resources of all 47 computer nodes in the L3 trigger system fully to online data analysis.

The RPT upgrade will bring us more resources, computing power, and control in the L2 hardware and allow more dynamic analysis in the L3 trigger system.

3.8 Summary of the DAQ System for the Runs

The design and the upgrades of the KOTO DAQ system aims to improve the $K_L \to \pi^0\nu\overline{\nu}$ physics study, provide dynamic data collection for other valuable studies, and to enhance the DAQ system performance[1]. A summary of the stages of the DAQ system is shown in Table. 3.2.

[1]See Ch. 4

Chapter 4
Data Collection

This chapter describes the data collection conditions, triggers used for data recording, and the DAQ performance in all 2015 runs, which is the data set used in this thesis for the analysis of the $K_L \to \pi^0\nu\overline{\nu}$ study.

4.1 Accelerator Condition

The data collection periods are divided as "Runs", following the operation cycles of the J-PARC MR. The data collection within each "Run" in the KOTO experiment is distinguished as "runs", where different data recording methods can be adjusted between each "run". Data collected from Run 62∼65 were used to set the upper limit of the $K_L \to \pi^0\nu\overline{\nu}$ branching ratio in this thesis. The scattered K_L study in this thesis used special runs in Run 74∼75, after the CDT hardware was installed in the DAQ system[1]. In 2015, beam power from 23.7 kW to 42 kW were delivered to Hadron Hall with 2 s beam on and 4 s beam off over the repetition of 6 s (a spill), as shown in Fig. 2.3. The beam extraction occurred every 6 s prior to 2015 summer (Run 62, Run 63) and 5.52 s afterwards (Run 64, Run 65). The beam intensity was measured by SYIM and TMon, as shown in Fig. 2.2. The SYIM recorded the number of particles scattered off the vacuum window and TMon measured the number of secondary particles generated from the T1-target using plastic scintillators. Table 4.1 lists the details of physics data collection in 2015. Chronological beam operation conditions with the accumulated number of protons on T1-target (P.O.T.), beam

[1]See Table 3.2

Table 4.1: A list of KOTO 2015 physics data collection.

Run	Beam Power	Duration	Total Hours	P.O.T.	
				Delivered	Recorded
62	23.7 kW, 26.4 kW	04/24/15 ∼ 05/07/15	178	3.02×10^{18}	2.33×10^{18}
63	26.4 kW, 29.3 kW, 33 kW	06/05/15 ∼ 06/26/15	235.2	4.84×10^{18}	3.59×10^{18}
64	32 kW, 32.7 kW, 38 kW, 39 kW	10/15/15 ∼ 11/12/15	239	9.10×10^{18}	7.32×10^{18}
65	38.5 kW, 38.7 kW, 42 kW	11/15/15 ∼ 12/18/15	524.3	2.08×10^{19}	1.69×10^{19}

power, and physics data collected are shown in Fig. 4.1. In the 2015 runs, 3.78×10^{19} protons were delivered to the T1-target from the MR. We recorded 3.02×10^{19} P.O.T. considering the DAQ dead time.

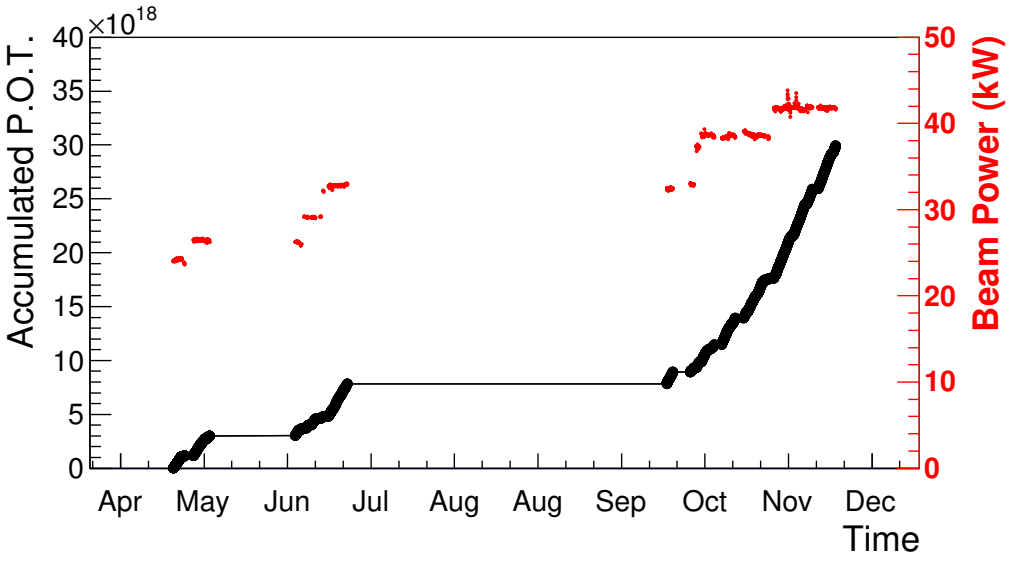

Figure 4.1: Accumulated P.O.T. recorded with beam power in the 2015 runs. Black data points show the accumulated P.O.T. over time. Red data points are the beam power at the time.

drive

4.2 Detector Condition

In the analysis, a few detector channels were excluded - they were either dead or unstable due to sparks from the applied high voltage. The positions of these channels are included in Fig. 4.2. There were two dead channels in the CsI calorimeter (ch 2071,

ch 1505) where the signals were completely unavailable. One MB channel (ch 39) and one CC04 channel (ch 44) went through several high voltage trips during data recording.

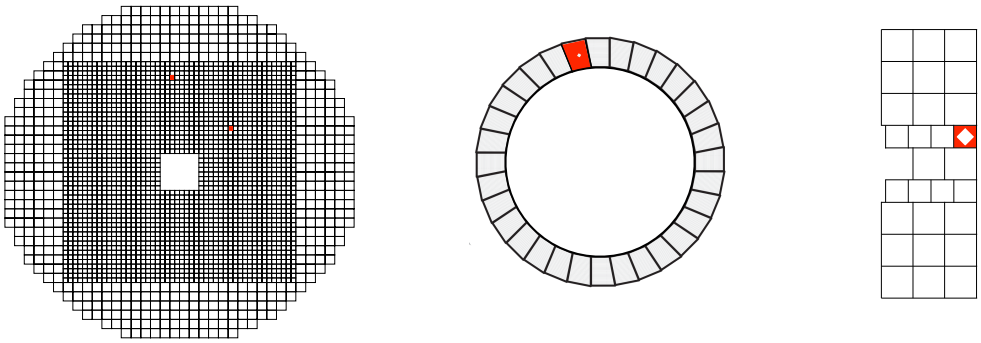

Figure 4.2: Detector channels excluded in the 2015 analysis. The left, middle, and right figures are upstream view of the CsI calorimeter, MB, and north side CC04 respectively. The channels excluded from the 2015 analysis were marked red. MB has dual-end readout and only the channel on the downstream side of the marked module was excluded.

4.3 Trigger Condition

Several types of trigger were developed to achieve various objectives in the analysis. Figure 4.3 shows the summary of beam usage for all the data collection in 2015. Triggers used in the 2015 runs include physics, normalization, minimum bias, and five external triggers for different analysis focuses, which will be introduced in the following subsections. A mixture of these triggers were used to simultaneously collect physics-triggered events for the main analysis of $K_L \to \pi^0\nu\overline{\nu}$, check on accidental activities, and monitor detector gain performance. Furthermore, we introduced prescaling factors to maintain the trigger rate from a combination of trigger types within the bandwidth of the DAQ trigger system while maximizing the data collection sensitive to $K_L \to \pi^0\nu\overline{\nu}$. Different prescaling factors were applied to different triggers. Within each Run period provided by the J-PARC accelerator, the KOTO experiment collected data every 500 spills, called "runs". Different combinations of

triggers, value of trigger thresholds, and prescaling factors were flexible to be adjusted for each run.

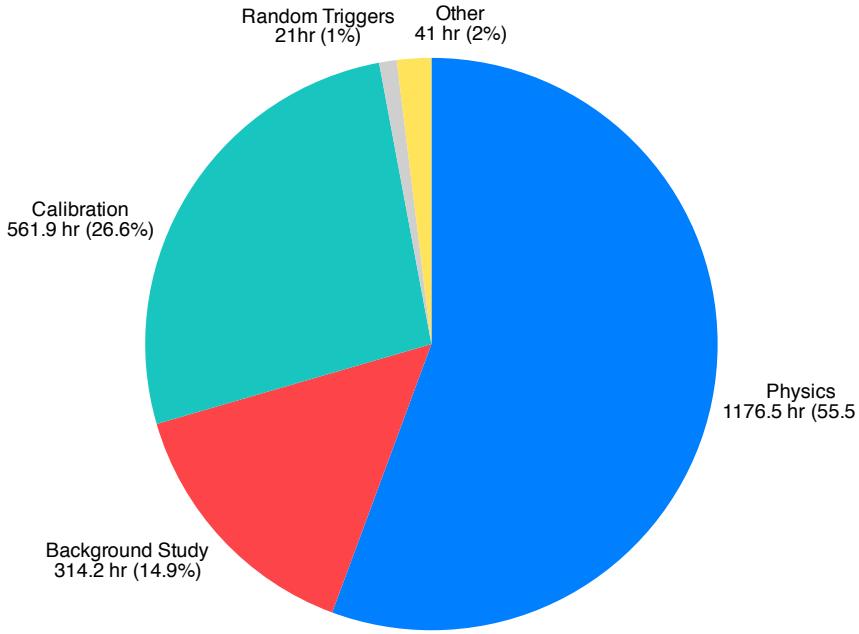

Figure 4.3: Summary of 2015 data collection. This figure included the data collection from beam and the cosmic muon runs which did not require beam usage ($\sim$ 485 hr in "Calibration" category). Physics runs are the data used for the $K_L \to \pi^0\nu\overline{\nu}$ analysis. Background study runs include Al-target runs and runs related to halo neutron measurements. Calibration runs include muon runs, LED runs, and certain detector-triggered runs. Random trigger runs used TMon trigger and clock trigger. Other runs enclose all the runs that are not categorized above, including collimator scans, trigger rate check, trigger study, etc.

4.3.1 Physics Trigger

The physics trigger was the main trigger designed for the $K_L \to \pi^0\nu\overline{\nu}$ event selection. We required large transverse momentum (P_T) from the two-photon system inside the CsI calorimeter and no activities in the veto detectors. The L1 trigger used the total energy sum (Et) in the calorimeter and veto detectors to perform online veto. The L2 trigger system used the COE to discriminate events with large transverse momentum. The thresholds used in the L1 and the L2 trigger system is

shown in Table 4.2. As we desired to collect all the candidates of $K_L \to \pi^0\nu\overline{\nu}$ event, a prescaling factor of 1 was applied in the physics trigger. Figure 4.4 shows a summary of the trigger conditions during data collection.

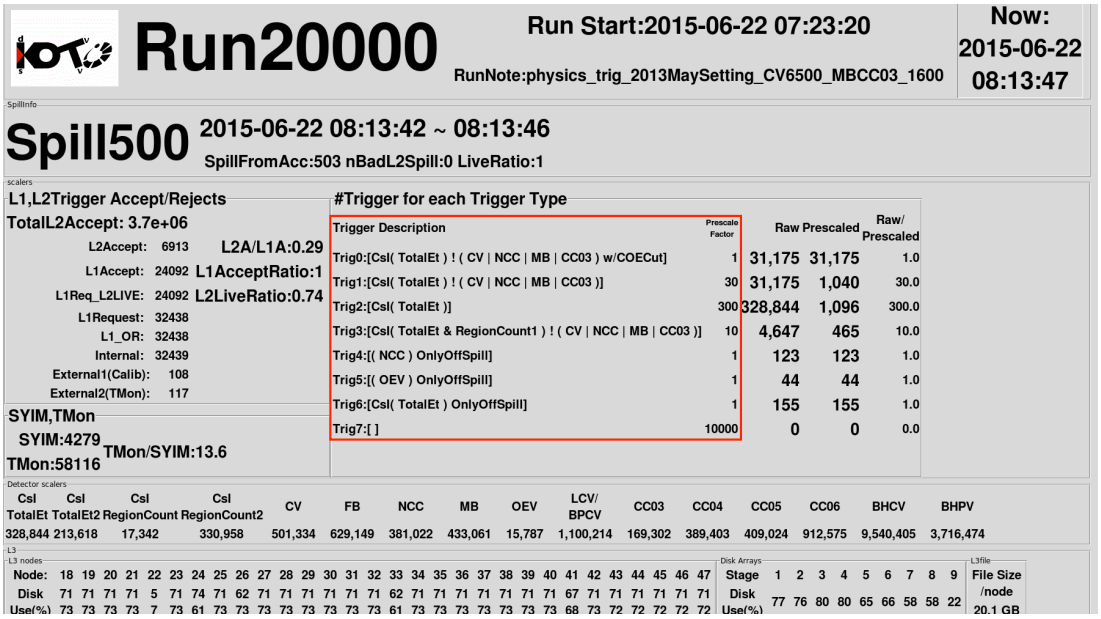

Figure 4.4: A screenshot summary of the trigger conditions for a physics run. This summary is updated every spill during data collection as part of DAQ status monitor. As shown in the red box, a combination of triggers with different prescaling factors were used in the physics run. Trig 0 is physics trigger, Trig 1 is normalization trigger, and Trig 2 is minimum bias trigger. These three triggers are critical to the physics analysis. The trigger rates before and after prescaling factors are to the right of the trigger descriptions.

4.3.2 Normalization Trigger

The normalization trigger had the same feature as the physics trigger, but without the COE radius cut. This trigger aimed to collect $K_L \to 3\pi^0$, $K_L \to 2\pi^0$, and $K_L \to 2\gamma$ decays for normalization in the analysis. We used these information to calculate the K_L flux and estimated the number K_L that entered our detector. To collect these events with prioritizing the physics trigger, a prescaling factor of 30 was used.

Table 4.2: A list of threshold requirements in the L1 and the L2 trigger system.

L1 Trigger System

Detector	Total Et Threshold
CsI	> 550 MeV
NCC	< 60 MeV
MB	< 50 MeV
CV	< 0.8 MeV
CC03	< 60 MeV

L2 Trigger System

Veto	Threshold
COE radius	> 165 mm

4.3.3 Minimum Bias Trigger

The minimum bias trigger was made based on the total energy deposited in the CsI calorimeter. This trigger was identical to the normalization trigger but without any online veto. A prescaling factor of 300 was used.

4.3.4 External Trigger

There are five external triggers - cosmic ray, clock, laser, LED, and TMon trigger. They were used for the following purposes: detector calibration, detector gain and noise monitoring, and accidental events collection.

Cosmic Ray Trigger (Calibration Trigger)

The cosmic ray trigger was used for detector calibration. This trigger was generated when NCC, CsI calorimeter, or OEV detected cosmic ray muon activities. A list of the requirement for each detector and the CsI calorimeter region segmentation are shown in Table 4.3 and Fig. 4.5. For constant check on detector stability, the cosmic ray trigger was issued during off-spill timing.

Table 4.3: A list of cosmic ray trigger requirement.

Detector	Requirement
NCC	Total Et > 60 MeV
CsI	Coincidence of hits in both top and bottom counters for each region
OEV	Number of hit modules > 2

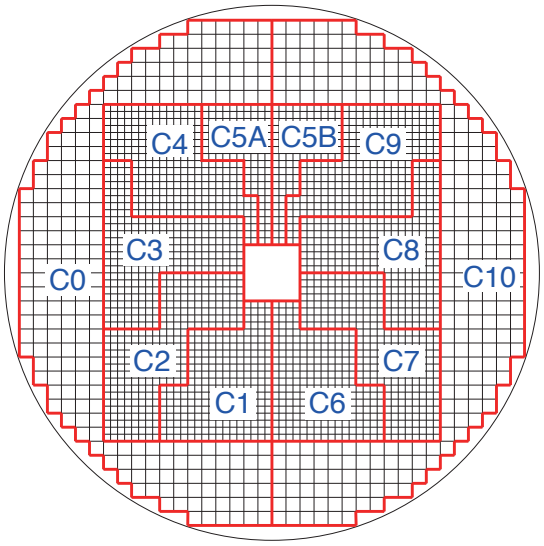

Figure 4.5: Segmentation of the CsI calorimeter for regional counting [52]. Each region corresponded to one L1 trigger, with 12 total regions. The labeling indicated the ADC crate ID to whom it belonged (ADC Crate 5 held two regions).

Clock Trigger (Random Trigger)

The clock trigger was known as "random" trigger. A 10 Hz periodic clock was used as a random trigger to take events for monitoring detector noise and counting rates.

Target Monitor Trigger (Accidental Trigger)

The target monitor (TMon) trigger, or "accidental" trigger, aimed to monitor accidental hits related to the beam using the target monitor, as shown in Fig. 2.5.

Laser Trigger (Gain Monitoring Trigger)

The laser trigger was used for the PMT gain correction and channel timing alignment in the CsI calorimeter. A 5 Hz laser was flashed and events were synchronized with this timing [49].

LED Trigger (Gain Monitoring Trigger)

The LED trigger served similar purpose as the laser trigger. It was used to evaluate gain stability on the PMTs and MPPCs, as well as to adjust timing offsets between detector modules. A 10 Hz clock, differed from that used in the clock trigger, was used to flash LEDs to each veto detector channel.

4.4 Special Runs

For certain detector calibration and background studies of $K_L \to \pi^0\nu\overline{\nu}$, different experimental setups and trigger combinations were used to collect data. The special runs used in 2015 were muon runs and Aluminum target (Al-target) runs. Details of these runs are described in the following subsections.

4.4.1 Cosmic Muon Run

The cosmic muon runs were taken before and after each accelerator Run period and during the accelerator maintenance for detector calibration and stability check. It triggered on data containing enough total energy (Et) in NCC, MB, and the CsI calorimeter. Externals triggers such as cosmic ray, laser, and LED triggers were used.

4.4.2 Beam Muon Run

Due to the geometry of the laser and LED systems, downstream detectors were not in position for calibration. We used beam muons to calibrate beam hole detectors. This was achieved by closing the beam plug, as shown in Fig. 2.6. When the beam plug was closed and the sweeping magnet was turned off, it leaves mostly charged muons as penetrating particles that entered the KOTO detector region. The detector counting rate decreased and we required a coincidence of hitting two detectors as the trigger requirement, such as BHPV. Another usage of the beam muon runs were to study how charged particle penetrate though detectors around or in the beam line,

Table 4.4: Al target properties.

	Z0 Al Target	DVU Al Target
Thickness	10 mm	5 mm
Diameter	100 mm	100 mm
Z Position	−634 mm	2795 mm

such as CV.

4.4.3 Aluminum Target Run

There were two circular Aluminum (Al) plates used as targets in the beam line during 2015 data collection. One was located in front of the FB, close to the origin of the z position (0 mm) and in front of the vacuum window[1], called Z0 Al target. The other one was located downstream of the FB, called Decay Volume Downstream (DVU) Al target. Remote control of the Al targets was available and the Al targets were inserted or removed from the beam depending on the purpose of data collection. The properties of the Al targets are listed in Table. 4.4.

The Al target runs were used for studies that require known z positions. The Z0 Al target runs were used for background studies of scattered neutrons and scattered K_L. Details of these background events are introduced in Sec. 8.4 and in Appx. A respectively. The DVU Al target runs were used to generate π^0 at the Al target, and $\pi^0 \to 2\gamma$ were used to calibrate the energy of the CsI calorimeter. Knowing the z position of the DVU Al target, which was the π^0 z generation position, we were able to reconstruct the invariant mass of two photons on the CsI calorimeter back to π^0 mass, as shown in Eq. 5.21. Contrarily, the energies of these photons can be obtained accurately by assuming the π^0 mass.

[1]See Sec. 2.3

4.5 DAQ Performance

The DAQ system was synchronized with the beam extraction cycle and collected data during LIVE, as shown in Fig. 2.3. Definition of some commonly used DAQ statistics are listed below:

- L1 Request (L1Req) - Events that passed the L1 trigger decision
- L1 Accept (L1A) - L1Req that are considered for a L2 trigger decision
- L2 Accept (L2A) - Events that passed the L2 trigger decision
- L2 Reject (L2R) - Events that failed the L2 trigger decision

4.5.1 ADC

The CsI calibration from the cosmic ray trigger, using the vertical cosmic ray penetrating the calorimeter and assuming an energy deposit per unit path length in the CsI to be 56 MeV/mm [8], provided an initial calibration factor of the ADC count rate to energy. This conversion factor in 2015 was 1 MeV = 8.89 ADC counts. This value was used to calculate trigger thresholds and make online trigger decisions.

The ADC lossless data compression was implemented in later 2015 to relax the L2 stress and to collect more events. The performance of the ADC data compression will be introduced in Sec. 4.5.3.

4.5.2 L1 Trigger Performance

The L1 trigger made trigger selections based on Et sum information. Figure 4.6 and Fig. 4.7 show the L1 trigger performance on the veto detectors and the calorimeter energy cut. The blue regions are the energy distribution prior to the L1 energy veto and red regions are after the cut. The L1 decision was made online, without calibration; hence leaving a tail for some energies beyond the threshold. A summary list of the L1 trigger threshold requirements is in Table 4.2.

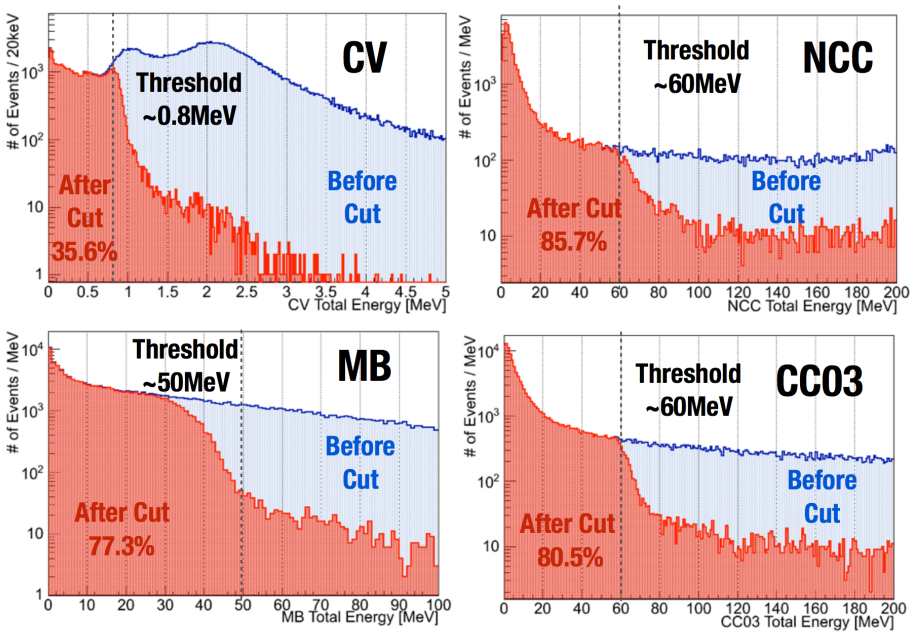

Figure 4.6: L1 trigger performance on the veto detectors. From left to right, top to bottom are the following detectors: CV, NCC, MB, and CC03. The blue regions are the energy distribution in the veto detectors prior to the L1 trigger veto. Red regions represent the energy distribution after the L1 veto. The dotted lines are the threshold values used in the L1 trigger system [50].

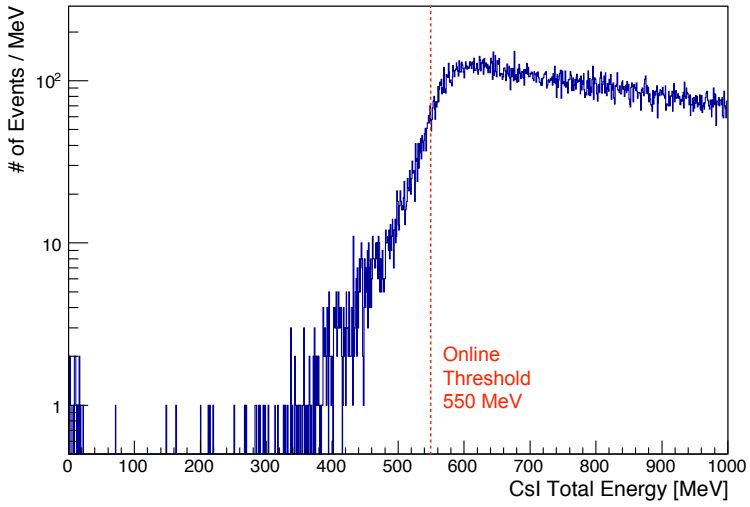

Figure 4.7: L1 trigger performance on CsI calorimeter. This is the energy distribution of the CsI calorimeter after L1 veto. The online threshold set in the L1 trigger was 550 MeV. Events above this threshold were accepted.

4.5.3 L2 Trigger Performance

The L2 trigger makes event selections using the Center-of-Energy (COE) radius obtained from the CsI calorimeter. The L2 online trigger performance is shown in Fig. 4.8. The blue and red regions are the COE radius distribution prior to and after the L2 trigger selection, respectively. On average, the COE radius selection rejected about 67% events.

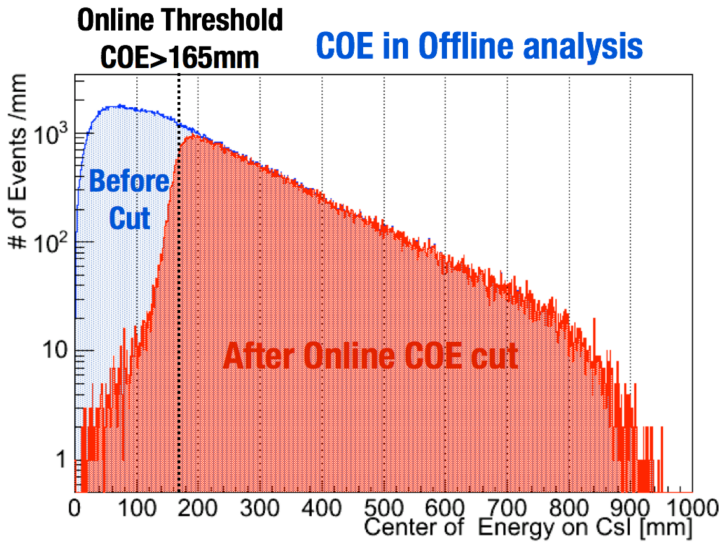

Figure 4.8: L2 trigger performance. The blue and red regions show the COE distribution before and after applying L2 veto [50].

4.5.3.1 L2 Livetime

The bottleneck of the KOTO DAQ system in 2015 was in the data passage between the ADC modules and the L2 trigger system. During high speed data recording, limited FIFO buffer size could lead to increase in DAQ system dead time. We introduced a variable to measure the performance of the L2 trigger system - L2 livetime.

The L2 livetime was determined by two trigger counting statistics - L1 Request and L1 Accepts. L1 Request (L1Req) refers to events that were triggered by detectors and passed the L1 trigger decisions. Due to the limitation of the FIFO buffer size and the L2 processing speed, as shown in Fig. 3.12, only part of the L1Req events

were considered for L2 trigger decisions. These events are L1 Accept (L1A). Among all the L1A events, triggers that passed the L2 trigger decisions are called L2 Accept (L2A). The L2 livetime is defined by the ratio of the L1A to the L1Req during a spill, as shown in Eq. 4.1. The L2 livetime was calculated spill by spill.

$$\text{L2 livetime} = \frac{\text{L1A}}{\text{L1Req}} \tag{4.1}$$

The L2 FIFO buffer size was designed to allocate space for 7 uncompressed total ADC data packets, which is the size of an uncompressed event and its equivalent to 17000 bits. A simulation study of the relationship between the L2 livetime, the L1 trigger rate, and the L2 FIFO fibber size was performed [47]. Figure 4.9 shows the results of simulation study for the 2015 runs. With data compression, we were able to improve the L2 livetime.

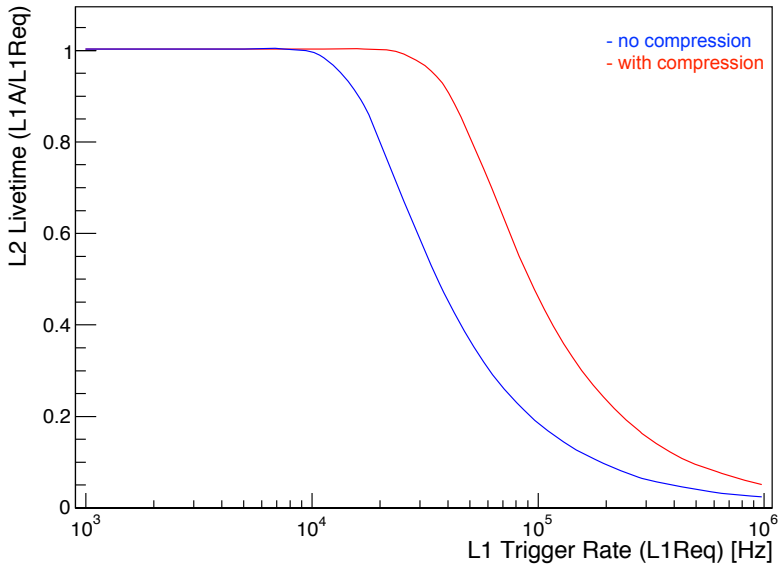

Figure 4.9: Simulation of L2 livetime with various L1 trigger rate. Blue curve shows the situation with uncompressed ADC data. Red curve is the scenario with compressed ADC data. Upon the same L1 trigger rate, a better L2 livetime can be achieved by using data compression.

We implemented lossless data compression algorithm inside the ADC firmware to reduce the data packets size in later half of the 2015 runs. This was to ease the

tension in the L2 trigger system and improve the L2 livetime, as shown in Fig. 4.10 and Fig. 4.11.

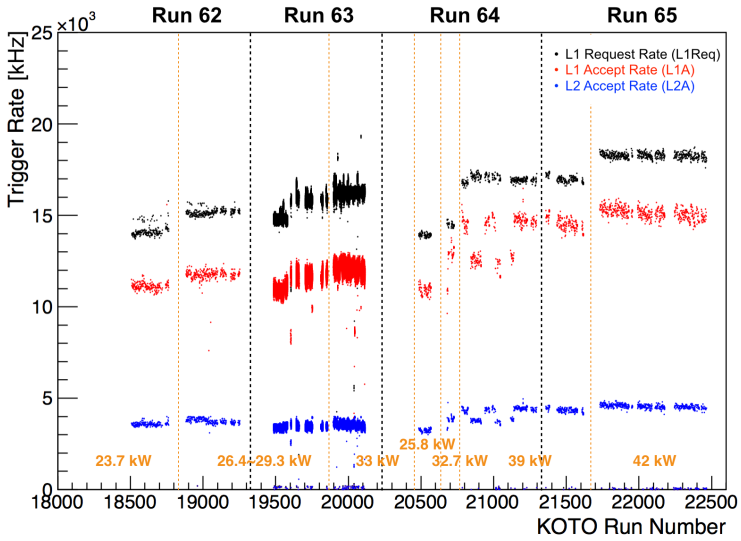

Figure 4.10: L1 and L2 trigger rates in 2015 runs. Black data points are the L1 trigger request rate (L1Req), red data points are the L1 trigger accept rate (L1A), and the blue data points are the number of L2 trigger accept rate (L2A). The L2 trigger accepted around 33% of L1A events.

4.5.4 L3 Trigger Performance

Event fragments arrived at the L3 trigger system, where complete events were built. Built events were decompressed for online analysis, though no event selections were used in 2015, and restructured for the data format required by offline data production. The lossless data compression ratio was 0.28, as shown in Fig. 4.12. An uncompresssed event has a compression ratio of 1. However, a fully compressed event does not have a compression ratio close to 0 since we used lossless data compression.

The L3 trigger system built, decompressed, compressed, and stored events. Similar to the L2 livetime, a L3 livetime is to measure the performance of the L3 trigger system and data quality. The L3 trigger system stored the events in the binary format, and was later produced as the analyzable ROOT files in KEK computer clusters. Eq. 4.2 defines the L3 livetime to be the number of events successfully produced from the

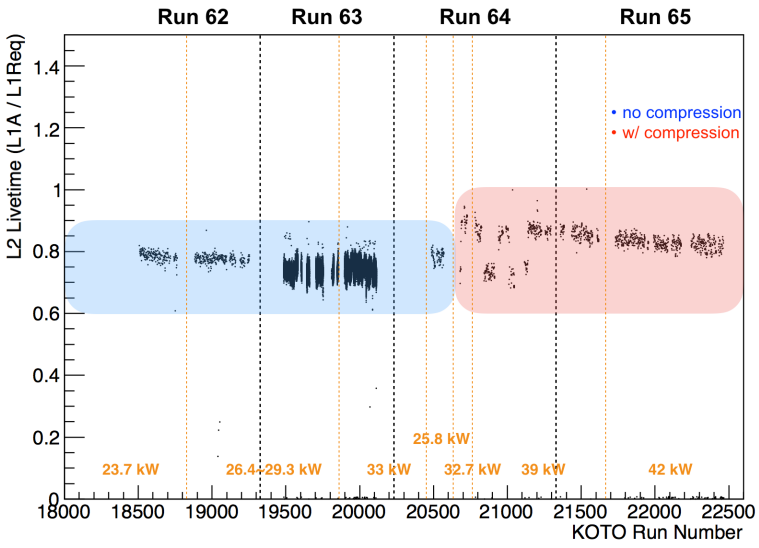

Figure 4.11: L2 Livetime in 2015 runs. Data compression inside the ADC was implemented during Run 64. The blue region indicates data collection without the ADC data compression and the red region shows that with ADC data compression. The beam power increased from Run 62 to Run 65, as indicated from the L1Req rate in Fig 4.10. The ADC data compression retained and improved the L2 livetime.

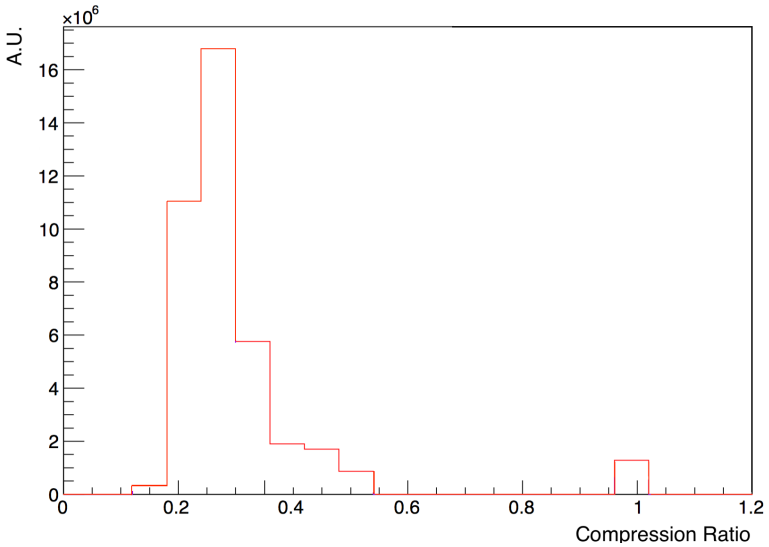

Figure 4.12: Lossless data compression ratio for physics runs. The compression ratio was 0.28.

stored L3 raw file to the number of events the L3 trigger system received from the L2 trigger system. The L3 livetime includes the following factors:

- Data packet lost between the L2 and the L3 trigger systems
- Data quality
- L3 event building performance

$$\text{L3 livetime} = \frac{\text{Events in offline production files}}{\text{L2A}} \tag{4.2}$$

Figure 4.13 shows the L3 livetime in the 2015 runs.

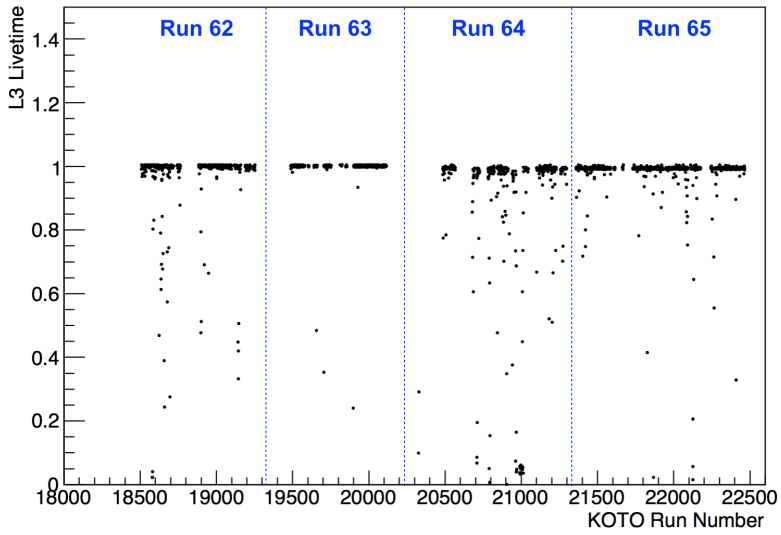

Figure 4.13: L3 livetime in 2015 physics runs. This livetime considers the event building performance in the L3 trigger, collected data quality, and successful rate of data production.

4.5.5 DAQ Livetime

To understand the DAQ performance and gauge the amount of data collected, DAQ livetime is an important index. The DAQ livetime takes each stage of the trigger performances as well as data quality check into consideration. Equation 4.3 defines the DAQ livetime. It is used in the normalization in the offline analysis to calculate the number of P.O.T. accumulated over the beam time.

$$\begin{aligned} \text{DAQ livetime} &= \text{L2 livetime} \times \text{L3 livetime} \\ &= \frac{\text{L1A}}{\text{L1Req}} \times \frac{\text{Events in offline production files}}{\text{L2A}} \end{aligned} \tag{4.3}$$

4.5.6 Improvement

Up to 2018, a series of DAQ upgrades were carried out. Currently, the L1 trigger is able to perform trigger selection based on the number of clusters on the CsI calorimeter using CDT[1]. To further relieve the stress on the L2 FIFO buffer, we expanded the FIFO size from equivalent of 7 ADC uncompressed data to 11. A optional trigger decision in the L3 trigger system towards flexible online analysis is also implemented. These upgrades all together were able to increase the DAQ livetime to 98% with the 50 kW beam. As mentioned in Ch. 3.7, moving event building from the L3 trigger to the L2 trigger will further utilize the DAQ system efficiently, which can shift the focus on the L3 trigger system towards versatile online analysis and event selections.

[1]See Ch. 3.7

Chapter 5
Analysis Strategies

This chapter describes the event reconstruction procedure, analysis methods used, and event selections for the $K_L \to \pi^0\nu\overline{\nu}$ study. Two studies that are necessary to set the upper limit of the $K_L \to \pi^0\nu\overline{\nu}$ ratio are the K_L measurements from normalization analysis (Ch. 7) and $K_L \to \pi^0\nu\overline{\nu}$ background estimation (Ch. 8). Events in these analysis often involve processes of a K_L decays to multiple π^0 and a π^0 decays into two photons. We used the waveform data recorded to reconstruct and study these events.

5.1 Event Reconstruction

As mentioned above, the event reconstruction mainly involves reconstruction of photons (γ) to pions (π^0), then to kaons (K_L). The event reconstruction flow is shown in Fig. 5.1. We obtained the energy and timing information from the waveform data and used them to identify photon clusters (γ clusters) on the CsI calorimeter. The γ clusters can be reconstructed to π^0s and further to a K_L using the energy information on the CsI calorimeter. Details of event reconstruction methods are described in the following subsections.

5.1.1 Waveform Energy and Timing Extraction

The event reconstruction was built upon the extracted energy and timing information from the waveform data. It is important to implement methods that lead to

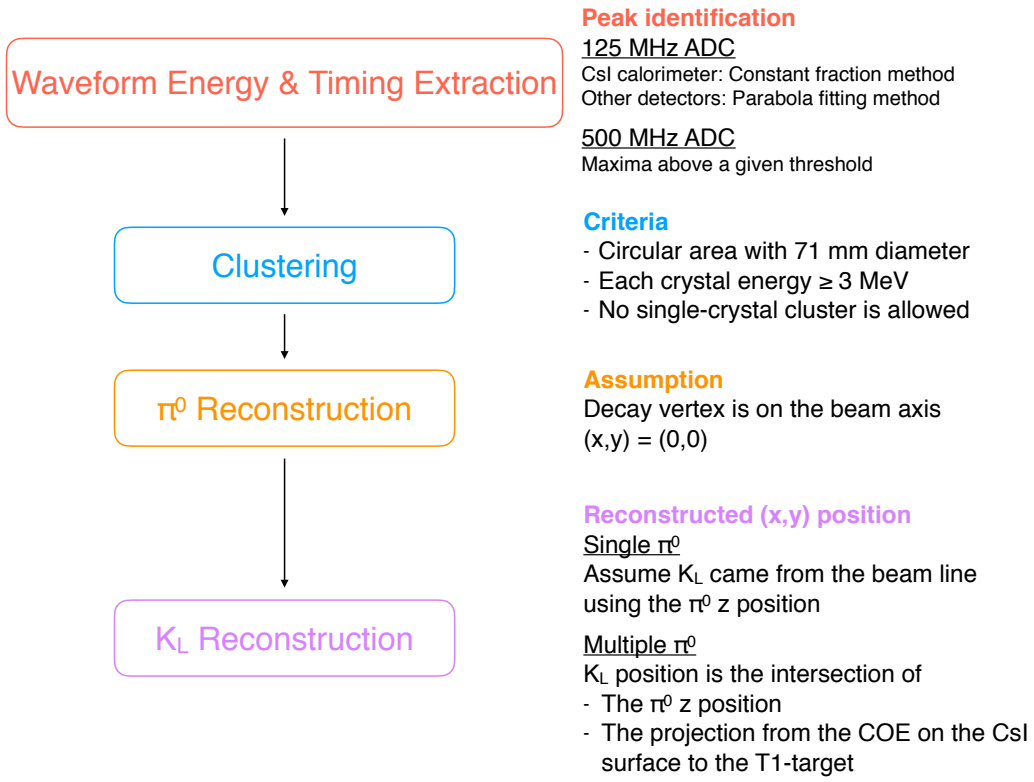

Figure 5.1: Event reconstruction flow and methods.

accurate energy and timing information.

As described in Sec. 3.3, waveform from each detector channel was digitized by two types of ADC modules. The energy and timing extraction for these two types of ADC modules are detailed below.

5.1.1.1 Detectors with 125-MHz ADC Modules

The 125-MHz ADC modules collected waveforms for 64 samples for every event, which correspond to a 512 ns event window. We expected a single pulse inside an event window, as its energy and timing information were defined. In case of multiple pulses appeared in an event window, the pulse closest to the trigger time ("nominal time") was chosen for timing extraction. A list of detectors using 125-MHz ADC modules can be found in Table 3.1.

Pedestal

Pedestal was defined as the baseline of a waveform. The average values and the standard deviations of the first 10 and the last 10 samples of the waveform were calculated. The average value with the smaller standard deviation was used as the pedestal for the corresponding detector channel. Each sample inside the waveform was subtracted by this pedestal value after the pedestal was defined.

Energy

The energy was defined by taking the integration of all 64 samples after pedestal subtraction and then multiplying by a calibration constant. The calibration constant converted the ADC counts to energy in MeV. The calibration constant was unique for each channel and was obtained from the cosmic muon runs, beam muon runs, and DVU Al target runs, as described in Sec. 4.4.

Timing

Two timing extraction methods were used to extract timing information from the waveforms: constant fraction method and parabola fitting method. Timing information is critical in the analysis, especially in veto decision making. The constant fraction method, which gave a better timing resolution, was used for the CsI calorimeter since good timing reconstruction for the π^0 reconstruction was desirable. The parabola fitting method, which was sensitive towards distinguishing overlapping pulses, was used for all the other detectors with 125-MHz ADC modules since pulse pileups were more severe and the veto timing was critical in the veto detectors for background reduction.

- **Constant Fraction Method**

  The constant fraction method defines the timing of the channel by checking the rising edge of the waveform when exceeds the half-peak-height. This method has better timing resolution compared to a leading edge threshold triggering.

However, it is less sensitive in obtaining correct timing with overlapping pulses scenario. The constant fraction method was only used in the CsI calorimeter because we wanted to achieve good timing resolution and there were less chances for occurrence of overlapping pulses due to the small cross sections of each CsI crystal[1]. The left plot in Fig. 5.2 shows an example of the constant fraction extracted waveform timing.

- **Parabola Fitting Method**

  As mentioned in Sec. 3.3, a 10-pole Bessel function filter was used in the 125-MHz ADC modules to shape the pulses into Gaussian waveforms. Therefore, the parabola fitting method can be used in these waveforms. The parabola fitting method assumes the pulse shape is parabolic and defines its timing based on the timing of the pulse peak. To fit a waveform, the waveform was first smooth out to reduce the fluctuation due to the noise by taking the moving average of consecutive 5 samples. The peak position was obtained from fitting a parabolic function around the peak. Equation 5.1 shows the definition of the parabolic function, where A, B, and C can be calculated analytically. The parameter B was the fitted peak time and used as the timing of the channel. In case of multiple pules existed in an event window, all pulses above a given threshold and with a local maximum point were fitted with the parabolic function. The one closest to the nominal time was chosen to be the timing of the channel. The right plot in Fig. 5.2 shows an example of the parabola fitting extracted waveform timing.

  $$y(t) = A(t - B)^2 + C \tag{5.1}$$

  Detectors other than the CsI calorimeter tended to have two or more pulses inside an event window. Hence, the parabola fitting method was more desirable.

Examples of wrong timing calculations using constant fraction method with multiple pulses are shown in Fig. 5.3. Details of timing extraction using both methods

[1]Small crystals: 2.5 cm×2.5 cm. Large crystals: 5 cm×5 cm

can be found in Ref. [51]. Regardless of the timing extraction methods used, the timing offsets were corrected by a timing calibration constant for each channel at the end.

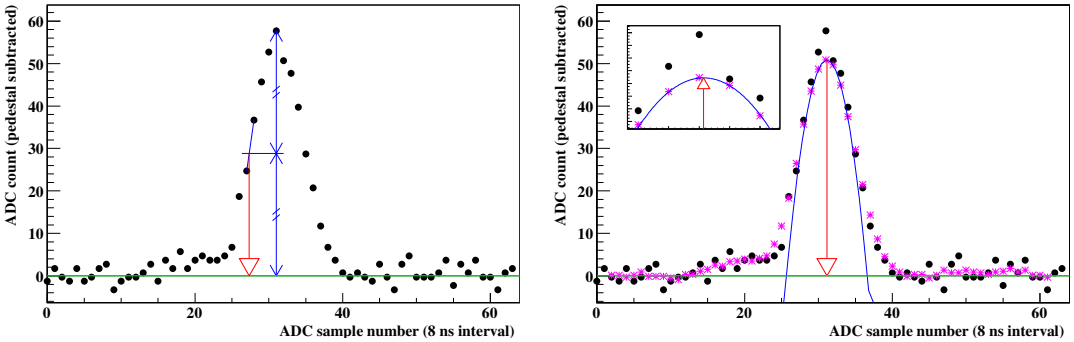

Figure 5.2: Waveform timing extraction with the constant fraction method (left) and the parabolic fitting method (right) [51]. The green lines and red arrows represent the pedestal values and the waveform timing, respectively. In the left figure, the blue line shows the peak of the waveform and the timing was defined to be the timing when the amplitude reaches half of the peak. In the right figure, the purple points show the moving average of the waveform and the blue line is the fitted parabolic function using the three points around the peak. The timing of the waveform was determined by the location of the peak, as shown in the zoomed in window on the top left corner.

5.1.1.2 Detectors with 500-MHz ADC Modules

As mentioned in Sec. 3.3, the 500-MHz ADC modules, which had a sampling rate four times of the 125-MHz ADC modules, were used to handle detectors with high trigger rate. As shown in Table 3.1, downstream detectors such as BHPV and BHGC used 500-MHz ADC modules. The 500-MHz ADC modules collected waveforms with 256 samples for every event, which corresponded to a 512 ns event window. In contrary to the single energy and timing extraction for detectors with the 125-MHz ADC modules, we expected multiple hits occurring inside an event window due to high counting rate. To avoid misidentifying an off-timing hit as a true hit, every pulse inside the event window was identified, and its corresponding energy and timing information was recorded. Figure 5.4 shows an example of the pulse identification for

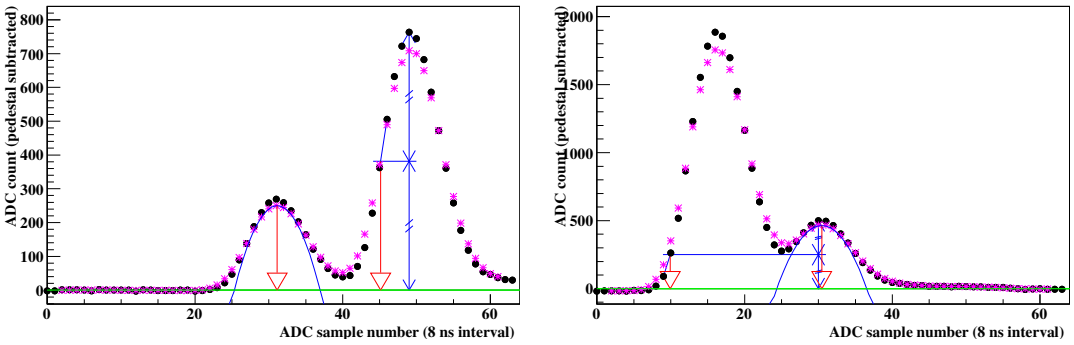

Figure 5.3: Pulse pileups timing determination [51]. Constant fraction method can lead to miscalculation of timing information when an event window contains multiple pulses. Both the constant fraction and parabola fitting methods were used in the figures. The green lines show the pedestal value, the red arrows are the timing defined by each method, and the purple data points are the moving average waveform. In the left figure, the constant fraction method identified the timing based on the largest peak in the 64 samples, while the actual timing should have be determined using the first pulse. If a restriction on the timing range was implemented, situation in the right figure could still occur, where the constant fraction method identified the waveform using first waveform, as where the half-peak-height was found. On the other hand, the parabola fitting method can exclude these situation by finding the peak closest to the "nominal time".

the BHPV detector.

Pedestal

Pedestal was defined using the most common value appeared in the waveform by fitting a Gaussian function to the histogram filled with the 256 samples of ADC count values. Similar to the detectors with 125-MHz ADC modules, each sample in the waveform was subtracted by the pedestal value after the pedestal value was defined.

Pulse Identification

Pulses were searched through 256 samples by identifying local maxima above a given threshold[1]. A range of samples was given to calculate the energy and timing for the pulses identified.

Energy

After the pulse identification, the energy was calculated by integrating a range of samples around a pulse[2]. The calibration constant used to convert the integrated ADC counts into energy in MeV was obtained from the beam muon runs.

Timing

In contrast to the 125-MHz ADC modules, the 500-MHz ADC modules did not use the 10-pole Bessel function filter and did not have Gaussian-like waveform shapes. Hence, the parabola fitting method was not suitable for pulse identification. We used constant fraction method to obtain the timing information for each pulse. A timing calibration constant was used to correct the timing offsets for each channel at the end.

5.1.2 Energy and Timing Reconstruction for Detector Modules

The energy and timing information were extracted differently for single-side readout and double-side readout detectors.

5.1.2.1 Single-Side Readout Detector

The energy and timing for each single-side readout detector channel were used as the energy and timing information for the detector module.

[1] new BHCV: 60 ADC counts, BHPV: 15 ADC counts, and BHGC: 15 ADC counts
[2] new BHCV: 60 samples, BHPV: 15 samples, and BHGC: 15 samples

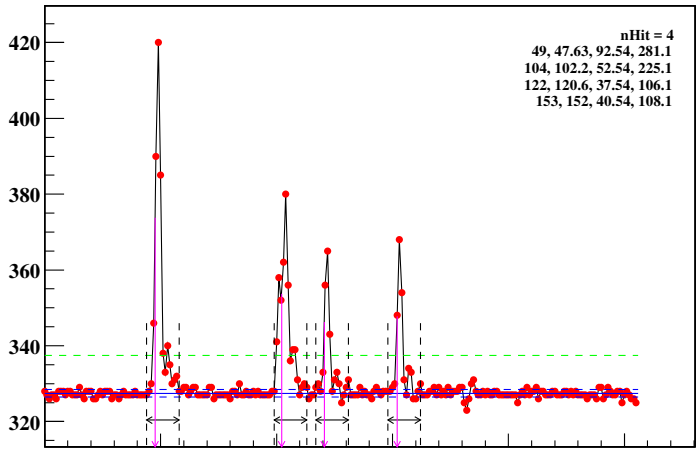

Figure 5.4: An example of the energy and timing extraction of the BHPV detector with the 500-MHz ADC module [51]. The blue solid and dashed line indicate the pedestal value and its 1σ region. The green line is the threshold used for peak searches. The purple arrows identify the timing and the black arrows show the range for energy integration.

5.1.2.2 Double-Side Readout Detector

For double-side readout detectors, each module contained two channels, one on each end of the module. The energy and timing information of the module were determined from both channels.

CV, CC03, and Downstream Collar Counters

For double-side readout detectors other than the MB and the BCV detectors, the energy of the module was defined to be the sum of the energy from both channels. The timing of the module was defined to be the mean timing for both channels.

MB and BCV

The MB and the BCV detectors used Wave-Length Shifting (WLS) optical fibers to read out scintillating lights. Due to the length of the detector modules[1], we considered the attenuation of light propagation inside the WLS fibers when calculating the energy and timing. In the following calculations, the readout z position of the module is

[1]See Sec. 2.3.2 and Sec. 2.3.3

define to be z_{up} (z_{down}) for the upstream (downstream) channels. The variable z_{hit} is defined to be the hit z position from the particle, where $z_{up} < z_{hit} < z_{down}$. The propagation speed of the scintillating light in the WLS is represented as v.

- **Timing**

  The timing of upstream and downstream channels are defined in Eq. 5.2 and Eq. 5.3. We used these equations to calculate the module timing (t_{mod}) and module hit position (z_{mod}).

$$t_{up} = \frac{z_{hit} - z_{up}}{v} \tag{5.2}$$

$$t_{down} = \frac{z_{hit} - z_{down}}{v} \tag{5.3}$$

  The timing of the module, t_{mod}, is obtained by averaging the timing from both the upstream and the downstream channels, as shown in Eq. 5.4. The module timing is independent on the hit position.

$$\begin{aligned} t_{mod} &= \frac{t_{up} + t_{down}}{2} \\ &= \frac{z_{down} - z_{up}}{v} \end{aligned} \tag{5.4}$$

  The module hit position, z_{mod}, and the center of module position, z_{center}, are defined in the first and the second term of Eq. 5.5, respectively.

$$\begin{aligned} z_{hit} &= \frac{v}{2}(t_{up} - t_{down}) + \frac{z_{up} - z_{down}}{2} \\ &= z_{mod} + z_{center} \end{aligned} \tag{5.5}$$

- **Energy**

  The amount of energy observed through the PMTs was affected by the attenuation in the WLS fibers. Figure 5.5 shows the number of ADC counts with the dependence of detector z positions. This relationship can be fitted by exponential functions defined in Eq. 5.6 and Eq. 5.7, where the energy of the module is

defined in Eq. 5.8. The variables E_{up} (E_{down}) are the original energy deposited on the upstream (downstream) detector. The energies of the detector channels observed by the PMTs are e_{up} (e_{down}) for the upstream (downstream) detector. The fitted constants for Fig. 5.5 are in Table 5.1.

$$e_{up} = E_{up} \exp\left(\frac{-z_{mod}}{\Lambda + \alpha z_{mod}}\right) \tag{5.6}$$

$$e_{down} = E_{down} \exp\left(\frac{z_{mod}}{\Lambda - \alpha z_{mod}}\right) \tag{5.7}$$

$$\begin{aligned} E_{mod} &= E_{up} + E_{down} \\ &= \frac{e_{up}}{\exp\left(\frac{-z_{mod}}{\Lambda+\alpha z_{mod}}\right)} + \frac{e_{down}}{\exp\left(\frac{z_{mod}}{\Lambda-\alpha z_{mod}}\right)} \end{aligned} \tag{5.8}$$

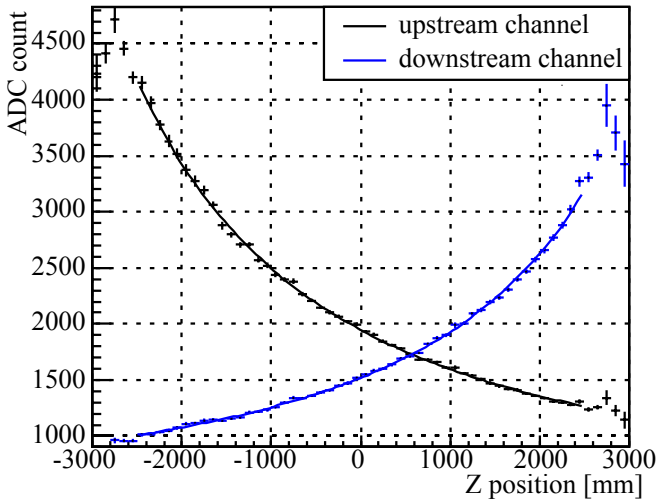

Figure 5.5: Attenuation

Table 5.1: Parameters for attenuation

Parameters	Values
v	168.1 mm/ns
Δ	4920.5 mm
α	0.495

5.1.3 Event Reconstruction with the CsI Calorimeter

When a high energy photon hit the CsI calorimeter, an electromagnetic shower was created and spread through several crystals because the cross section of the CsI crystals (2.5 cm) was smaller than the Molière radius (3.57 cm) [8]. This group of crystals were referred as a "cluster". Clusters with enough total energy were treated as γ clusters and were used for π^0 or K_L reconstruction. In the event reconstruction, we assumed $\pi^0 \to 2\gamma$, $K_L \to 2\gamma$, $K_L \to 2\pi^0 \to 4\gamma$, or $K_L \to 3\pi^0 \to 6\gamma$.

5.1.3.1 Clustering

Clustering refers to the processing of finding clusters. We selected CsI crystals with more than 3 MeV energy as cluster seeds and started with one that had the maximum energy deposited as a core cluster seed. If any other cluster seeds were found within 71 mm centered at the core cluster seed, they were grouped together to form a cluster, as shown in Fig. 5.6.

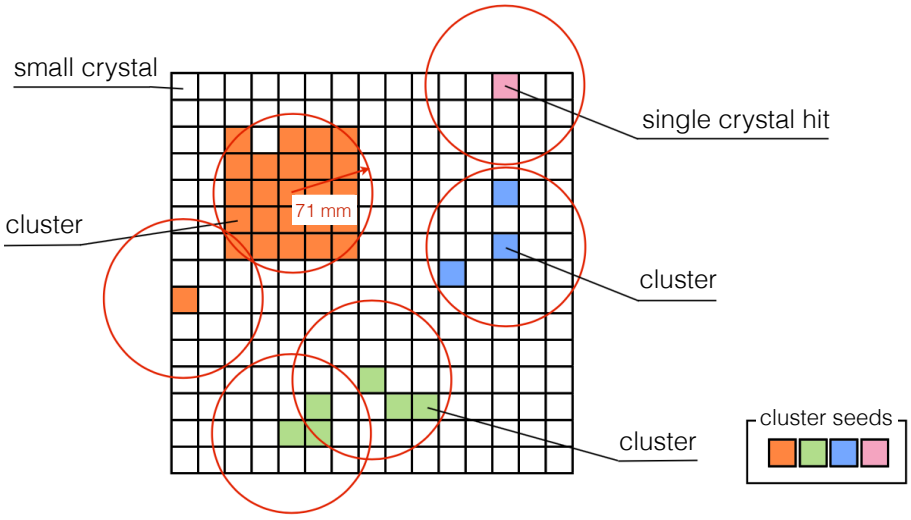

Figure 5.6: Examples of clustering [52]. The cluster finding used crystals above the 3 MeV threshold as seeds and seek for other seeds within their 71 mm radius. Different seed colors correspond to different clusters. However, single seed (pink) was not allowed to form a cluster.

After the first cluster was found, process iterated until all seeds were assigned to

be part of the cluster. In the case of a single crystal seed with no other crystals above 3 MeV in the circular area with the 71 mm radius, it was not considered as a cluster. We referred it as "isolated hit crystal" and used it for vetoing. Detail of such veto is described in Sec. 5.3.4.1.

After defining a cluster, its energy, positions, and timing of a cluster can be calculated from the individual crystals contained within the cluster:

$$E_{cluster} = \sum_{i=0}^{n} e_i \,, \tag{5.9}$$

$$x_{cluster} = \frac{\sum_{i=0}^{n} e_i x_i}{\sum_{i=0}^{n} e_i} \,, \tag{5.10}$$

$$y_{cluster} = \frac{\sum_{i=0}^{n} e_i y_i}{\sum_{i=0}^{n} e_i} \,, \tag{5.11}$$

$$t_{cluster} = \frac{\sum_{i=0}^{n} t_i/\sigma_t^2(e_i)}{\sum_{i=0}^{n} 1/\sigma_t^2(e_i)} \,, \tag{5.12}$$

where $E_{cluster}$, $x_{cluster}$, $y_{cluster}$, and $t_{cluster}$ are the energy, x position, y position, and timing of the cluster, respectively. Variable n denotes the total number of crystals contained within a cluster. For each individual crystal i, its deposited energy, x position, y position, and timing are represented as e_i, x_i, y_i, and t_i. The timing resolution $\sigma_t(e)$ was measured in the past beam test [53] to be

$$\sigma_t(e) = \frac{5}{e} \oplus \frac{3.63}{\sqrt{e}} \oplus 0.13 \,, \tag{5.13}$$

where σ_t is in the unit of ns, e is in the unit of MeV, and $\oplus$ represents quadrature addition.

In case an accidental hit were grouped into a cluster, we required the crystal hit

time (t_i) to be in the range of $t_{cluster} \pm 5\sigma(e)$. The process iterated until all the accidental hit crystals were removed from the cluster. Figure 5.7 shows the timing difference between crystals and the cluster.

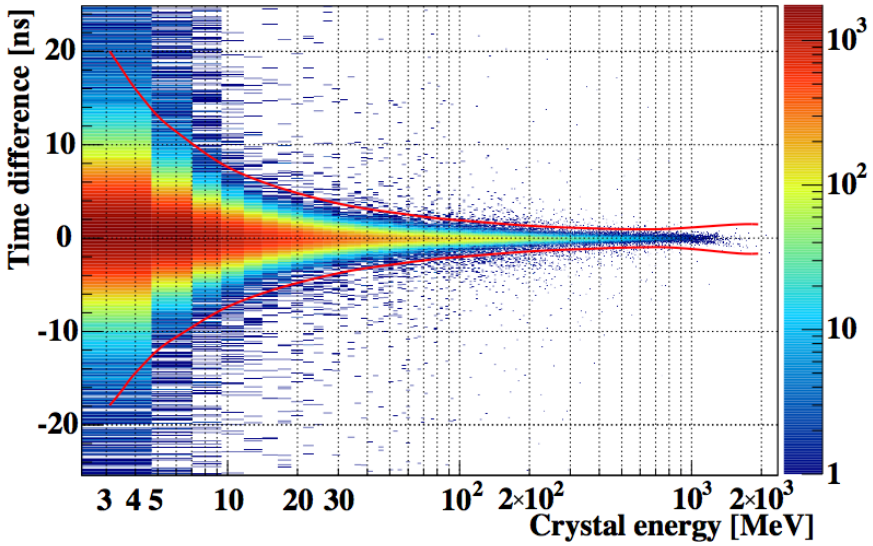

Figure 5.7: Rejection of accidental hits inside a cluster [52]. This figure shows the timing difference between the crystals to the cluster time, with the energies of the crystals. The colors represent the number of events in arbitrary unit. Crystals outside the timing difference (on top of the upper red line and below the lower red line) were treated as accidental hits and were rejected.

The clusters used for event reconstructions were assumed to be "γ clusters", as introduced below.

5.1.3.2 γ Cluster Selection

Clusters with energy larger than 20 MeV were identified as γ clusters and were used to reconstruction π^0s.

5.1.3.3 π^0 Reconstruction

To reconstruction a π^0, we used a two-body system of $\pi^0 \to 2\gamma$ with the invariant mass of $M_{\pi^0} = 134.9766$ MeV/c^2 [8] and assumed the π^0 decay vertex was on the beam axis, where both the x and the y positions were zeros. The assumption of the π^0 decay

vertex on the beam axis was to compensate the insufficient number of constraints we have to reconstruct a two-body decay. The π^0 transverse momentum (P_T) and decay vertex time ($T^{\pi^0}_{vtx}$) can be calculated using the π^0 decay vertex position.

Decay Vertex Position

The π^0 decay vertex can be obtained using the conservation of four momentum and the law of cosine. Figure 5.8 illustrated the schematics of a π^0 reconstruction, where the four momentum of the two-body system of two γ clusters (γ_1, γ_2) and their parent decay particle π^0 can be expressed as $\{(E_1, x_1, y_1, Z_{CsI}), (E_2, x_2, y_2, Z_{CsI})\}$, and $(E, x, y, Z^{\pi^0}_{vtx})$, respectively. Due to the π^0 beam-axis decay assumption, the four momentum of π^0 can also be written as $(E, 0, 0, Z^{\pi^0}_{vtx})$. The following equations describe the geometry in the schematics and were used in the π^0 reconstruction.

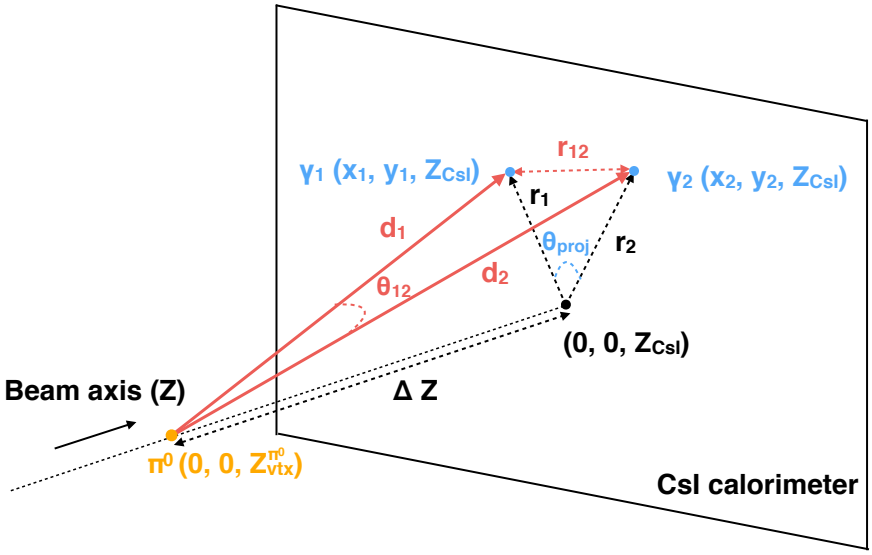

Figure 5.8: Schematic view of π^0 reconstruction. A π^0 (orange) decayed into two photons (blue) on the CsI calorimeter. The reconstruction was performed using the red triangle.

$$r_{12}^2 = d_1^2 + d_2^2 - d_1 d_2 \cos\theta_{12} \tag{5.14}$$

$$r_{12}^2 = (x_1 - x)^2 + (y_1 - y)^2 \tag{5.15}$$

$$d_1 = \sqrt{(\Delta Z)^2 + r_1^2} \tag{5.16}$$

$$d_2 = \sqrt{(\Delta Z)^2 + r_2^2} \tag{5.17}$$

$$r_1 = \sqrt{x_1^2 + y_1^2} \tag{5.18}$$

$$r_2 = \sqrt{x_2^2 + y_2^2} \tag{5.19}$$

$$\Delta Z = Z_{CsI} - Z_{vtx}^{\pi^0} \tag{5.20}$$

- Conservation of four momentum

  We can write the two-body decay system, $\pi \to 2\gamma$, as Eq. 5.21. Using the π^0 invariant mass, we can express Eq. 5.21 in terms of the opening angle θ_{12}.

$$\begin{aligned} M_{\pi^0}^2 &= (E_1 + E_2)^2 - (\vec{p_1} + \vec{p_2})^2 \\ &= 2E_1E_2(1 - \cos\theta_{12}) \end{aligned} \tag{5.21}$$

- Law of cosine

  The law of cosine equation was formed, given three sides of an triangle and an opening angle between two sides. Using the triangle formed by the sides of d_1, d_2, r_{12}, and the opening angle θ_{12} in Fig. 5.8, we constructed a quadratic equation for $(\Delta Z)^2$, as shown in Eq. 5.22 and Eq. 5.23.

$$(1 - \cos^2\theta_{12})(\Delta Z)^4 + (2\vec{r_1}\cdot\vec{r_2} - (r_1^2 + r_2^2)\cos^2\theta_{12})(\Delta Z)^2 + (\vec{r_1}\cdot\vec{r_2})^2 - r_1^2 r_2^2 \cos^2\theta_{12} = 0 \tag{5.22}$$

$$\Delta Z = Z_{CsI} - Z_{vtx}^{\pi^0} \tag{5.23}$$

  Two solutions of $(\Delta Z)^2$ are possible when requiring $Z_{vtx}^{\pi^0}$ to be positive and real. We choose the solution with $Z < Z_{CsI}$ to be the reconstructed π^0 decay z vertex

$(Z_{vtx}^{\pi^0})$.

Decay Vertex Momentum

After determining the π^0 decay vertex position, the π^0 transverse momentum can be calculated using the vector sum of transverse momentum from each γ cluster, as shown in Eq. 5.24.

$$P_T^{\pi^0} = \left| \sum_{i=1,2} E_i \frac{\vec{r_i}}{\sqrt{r_i^2 + (\Delta Z)^2}} \right| \tag{5.24}$$

As shown in Fig. 5.8, E_i denotes the cluster energy of the i-th γ cluster. The two-dimensional distance on the surface of the CsI calorimeter is defined to be $\vec{r_i} = (x_i, y_i)$ and $r_i = |\vec{r_i}|$. The unit for the transverse momentum is in MeV/c.

Decay Vertex Time

The π^0 decay vertex time can be obtained after knowing the π^0 decay vertex position. We compute the vertex time of each i-th cluster ($T_{vtx,i}$) using the positions of the π^0 decay vertex and the position of the i-th cluster on the surface of the CsI calorimeter, as shown in Eq. 5.25, where c is the speed of light.

$$T_{vtx,i} = t_i - \frac{\sqrt{r_i^2 + (\Delta Z)^2}}{c} \tag{5.25}$$

The π^0 decay vertex time, $T_{vtx}^{\pi^0}$, is given by the weighted average of i-th γ cluster time for total N number of γ clusters.

$$T_{vtx}^{\pi^0} = \sum_{i=1}^{N} \frac{T_{vtx,i}/\sigma_T^2(E_i)}{\sum_{j=1}^{N} 1/\sigma_T^2(E_j)} \tag{5.26}$$

The resolution for the vertex time with a given function of energy is as follows.

$$\sigma_T(E) = \frac{3.8}{\sqrt{e}} \oplus 0.19 \tag{5.27}$$

The units are MeV for energy and ns for vertex time.

5.1.3.4 K_L Reconstruction

In the analysis for the normalization modes, $K_L \to 3\pi^0$, $K_L \to 2\pi^0$, and $K_L \to 2\gamma$ were used to for calibration, normalization, and background studies. The K_L was reconstructed from π^0s or photons. We selected events with number of clusters (N') which was equal or greater than the number of photons (N) needed to reconstruct a K_L as candidates. The clusters with the closest cluster timing were selected for reconstruction and others were used for vetoing. The number of clusters selected to reconstruct K_L was 2, 4, and 6 for $K_L \to 2\gamma$, $K_L \to 2\pi^0$, and $K_L \to 3\pi^0$ respectively. The remaining clusters, if any, not used in the reconstruction were used for vetoing. These clusters were "extra clusters" and details of such veto is described in Sec. 5.3.4.1.

Reconstruction of $K_L \to 2\gamma$

The procedure is identical to the $\pi^0 \to 2\gamma$ reconstruction, but replacing the π^0 mass of $M_{\pi^0} = 134.9766$ MeV/c^2 with the K_L mass of $M_{K_L^0} = 497.614$ MeV/c^2 [8].

Reconstruction of $K_L \to 2\pi^0$ and $K_L \to 3\pi^0$

The steps for K_L reconstruction are as follows.

- **γ Cluster Pairing**

  In case of $K_L \to 2\pi^0$ and $K_L \to 3\pi^0$ decays, the K_L was reconstructed from π^0s. The number of possible combinations of γ cluster pairing to reconstruct to π^0s then to K_L are evaluated in Eq. 5.28, where $\prod$ is the product notation, C is the combination notation, and N is the total number of γ clusters used in the K_L reconstruction. The number of possible photon pairing combinations

are three for the two π^0s in $K_L \to 2\pi^0$ and 15 for the three π^0s in $K_L \to 3\pi^0$.

$$\prod_{i=1}^{\frac{N}{2}} \frac{C_2^{2i}}{\left(\frac{N}{2}\right)!} \tag{5.28}$$

Similar to the π^0 decay vertex reconstruction, in the first stage of the K_L reconstruction, we assumed the K_L decay vertex to be on the beam axis. It was reconstructed using the weighted average of each γ-pairing combination, as shown in Eq. 5.29. The variable Z_{k_L} is the possible reconstructed K_L vertex z position. For each i-th π^0, the reconstructed π^0 vertex z position ($Z_{vtx}^{\pi^0}$) and its position resolution ($\sigma_{z,i}$) were calculated.

$$Z_{K_L} = \sum_{i=1}^{\frac{N}{2}} \frac{Z_{vtx,i}^{\pi^0} \,/\, \sigma_{z,i}^2}{1 \,/\, \sigma_{z,i}^2} \tag{5.29}$$

Out of all the γ cluster pairing combinations, we found the best pairing by defining the "paring χ_z^2" in Eq. 5.30. The γ cluster pairing with the smallest χ_z^2 was chosen to be the best combination and its Z_{k_L} was assigned to be the reconstructed K_L z position, $Z_{vtx}^{K_L}$.

$$\chi_z^2 = \sum_{i=1}^{N} \frac{(Z_{vtx,i}^{\pi^0} - Z_{K_L})^2}{\sigma_{z,i}^2} \tag{5.30}$$

- ***K_L* Decay Vertex Correction**

  The K_L decay vertex may not be on the beam axis and can be corrected after knowing $Z_{vtx}^{K_L}$. The K_L decay x and y positions, can be obtained by interpolating the center of energy on the surface of the CsI calorimeter to the T1-target. The

intercept of the interpolation and $Z_{vtx}^{K_L}$ defines the K_L x and y positions:

$$X_{vtx}^{K_L} = X_{COE}\,\frac{Z_{vtx}^{K_L} - Z_{Target}}{Z_{CsI} - Z_{Target}}, \tag{5.31}$$

$$Y_{vtx}^{K_L} = Y_{COE}\,\frac{Z_{vtx}^{K_L} - Z_{Target}}{Z_{CsI} - Z_{Target}}, \tag{5.32}$$

$$X_{COE} = \frac{\sum_{i}^{N} E_{cluster}^{i}\, x_{cluster}^{i}}{\sum_{i}^{n} E_{cluster}^{i}}, \tag{5.33}$$

$$Y_{COE} = \frac{\sum_{i}^{N} E_{cluster}^{i}\, y_{cluster}^{i}}{\sum_{i}^{n} E_{cluster}^{i}}, \tag{5.34}$$

where K_L decay vertex $(x, y) = (X_{vtx}^{K_L}, Y_{vtx}^{K_L})$ and the center of energy on the surface of CsI calorimeter $(x, y) = (X_{COE}, Y_{COE})$. N is the number of clusters used in the K_L reconstruction.

After determining the K_L decay vertex, the energy and position corrections for π^0 and K_L were recalculated using this updated information. The process described in Sec. 5.1.3.3 was carried out again with slight modification. The energy and obtained vertex position information were used as constraints instead of the π^0 and K_L mass. Hence, we were able to obtain the distributions of the reconstructed invariant mass for π^0 and K_L. Calculations and corrections from this second event reconstruction was used as the final results.

Reconstruction of $K_L \to \pi^0\nu\overline{\nu}$

The $K_L \to \pi^0\nu\overline{\nu}$ decay contains one π^0. Its reconstruction procedure is identical to the π^0 reconstruction. The K_L decay vertex position and timing was treated to be the same as that of π^0, as the lifetime of π^0 is short and decays almost immediately after its decay from K_L.

5.2 Analysis steps for the $K_L \to \pi^0\nu\overline{\nu}$ decay

The analysis flow for the $K_L \to \pi^0\nu\overline{\nu}$ study is shown in Fig. 5.9. The analysis was performed by making event selections on the physics data, the number of clusters, the kinematics, and the detector vetos. Details of event selection criteria is discussed in Sec. 5.3. To avoid human bias on cut selections, data within the region sensitive to the signature of the $K_L \to \pi^0\nu\overline{\nu}$ decay were removed during the production stage and the result was covered with a black box ("blind region") throughout the analysis. Using the rest of the data, along with the Monte Carlo (MC) simulation studies, we optimized the event selection cuts based on various background studies. Consistency between the data and MC simulation was cross-checked throughout the analysis. Meanwhile, the study of the K_L flux measurement was carried out using the "normalization modes", which included $K_L \to 3\pi^0$, $K_L \to 2\pi^0$, and $K_L \to 2\gamma$ decays. This was to estimate the number of K_L produced by the protons hitting the T1-target. We used the normalization scale factor from the studies to calculate the upper limit of the $K_L \to \pi^0\nu\overline{\nu}$ branching ratio. Chapter 7 and Chap. 8 present the studies of the normalization modes and the MC background studies, respectively. Different cut sets and event sensitivities were evaluated with various signal region options. After finalizing all studies and cuts, we included previously removed data sets and reproduced all data, preformed all event selections on data, scaled the remaining number of events to the normalization factor, and revealed the black box ("open the box") to see the result. Ultimately, the number of events observed in the "signal region" determines the upper limit of the $K_L \to \pi^0\nu\overline{\nu}$ branching ratio calculation. The analysis for the given data set cannot be revised beyond this stage.

5.2.1 Signal Region and Blind Region

Figure 5.10 shows the definition of the signal region and and blind region on the $P_T^{\pi^0} - Z_{vtx}^{\pi^0}$ plane in the 2015 final analysis.

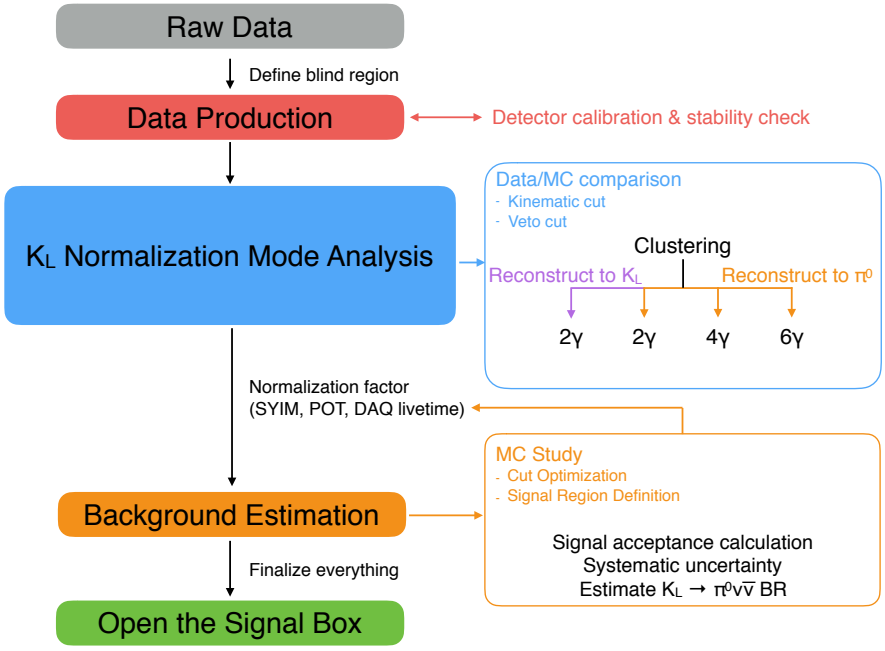

Figure 5.9: The $K_L \to \pi^0\nu\overline{\nu}$ analysis flow. Raw data was produced for analysis usage. Several versions of production data were made during the calibration. The data went through clustering and were categorized into different categories for different studies. The normalization analysis was carried out, followed by the background MC studies. After finalizing the analysis, considering all studies, we opened the box to reveal the result.

Signal Region

To identify $K_L \to \pi^0\nu\overline{\nu}$ events, a region sensitive to the large transverse momentum from the decay signature was drawn and set to be the signal region. Events within the signal region were considered to be $K_L \to \pi^0\nu\overline{\nu}$ event candidate and the upper limit of the $K_L \to \pi^0\nu\overline{\nu}$ branching ratio was calculated using the number of events observed in the signal region.

Several signal region was proposed and evaluated during the last stage of the analysis. The final decision was made to minimize the number of background events using the MC studies, while keeping the sensitivity to the signal. The signal region used in the 2015 analysis is as follows.

- 130 MeV/c < $P_T^{\pi^0}$ < 250 MeV/c,

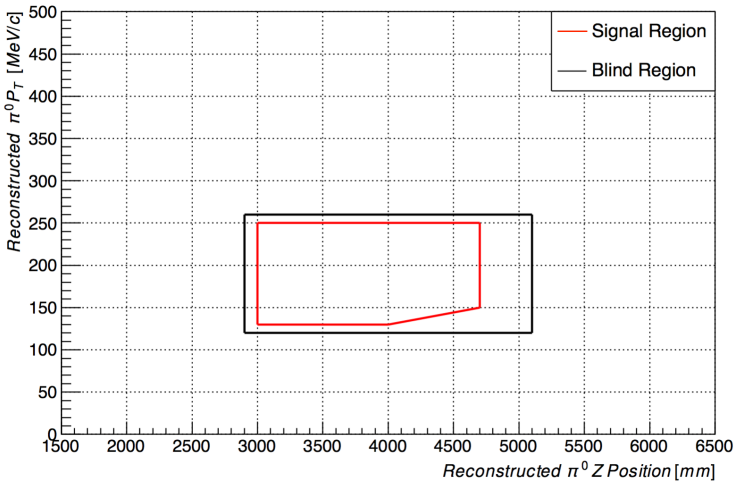

Figure 5.10: $K_L \to \pi^0\nu\overline{\nu}$ signal and blind region.

and a line from 130∼150 MeV/c for the $4000 \leq Z^{\pi^0}_{vtx} \leq 4700$ mm region

- 3000 mm $< Z^{\pi^0}_{vtx} <$ 4700 mm

The low $P^{\pi^0}_T$ region was bounded by the normalization events and the maximum $P^{\pi^0}_T$ from the $K_L \to \pi^+\pi^-\pi^0$ decay. The clip at the bottom right corner of the signal region was to remove downstream $K_L \to \pi^+\pi^-\pi^0$ background events. The bounds in the $Z^{\pi^0}_{vtx}$ were to reject π^0 or η generated at the detectors surrounding the decay region, such as the FB, NCC, and CV detectors.

Blind Region

As previously introduced, part of the data was removed during the analysis and regions that were sensitive to the $K_L \to \pi^0\nu\overline{\nu}$ decay signature was covered with a black box. Blinding the data prevented human bias on optimization of the cuts to reduce the number of events around the signal region. The blind region is defined as follows and is outlined in black in Fig. 5.10.

- 120 MeV/$c < P^{\pi^0}_T <$ 260 MeV/c
- 2900 mm $< Z^{\pi^0}_{vtx} <$ 5100 mm

5.3 Event Selections for the $K_L \to \pi^0\nu\overline{\nu}$ Analysis

Several event selection criteria was developed to reduce the background events and to identify $K_L \to \pi^0\nu\overline{\nu}$ events. This section describes the event selections used for the $K_L \to \pi^0\nu\overline{\nu}$ analysis. Some selection variables and the cut values were determined using the results from the normalization analysis and the background estimation in Ch. 7 and Ch. 8.

The event selection and cuts were performed on three categories: data selection, kinematic cuts, and veto cuts. The purpose for data data selection was to ensure analysis on data with good quality. The kinematic cuts were performed mainly using the information from the CsI calorimeter. The veto cuts were performed using other detector information. The summary of the cuts for the 2015 $K_L \to \pi^0\nu\overline{\nu}$ analysis can be found in Table 5.2∼5.3.

In this section, in case of two photons representations ($\gamma_k, k = 1, 2$), the cluster energy, positions, and time are $E_{\gamma k}$, $(x_{\gamma k}, y_{\gamma k})$, $t_{\gamma k}$. For single photon cluster representation, the subscript γ is used instead of k.

5.3.1 Data Selection

Number of Clusters

Events with two clusters were selected for the analysis, as shown in the 2γ data set under the π^0 reconstruction category (orange) in Fig. 5.9.

Data Quality

To carry out valid analysis, we ensured the data quality by checking the data taking conditions and errors for each run and each spill. Data with a chance of subjecting to corruption or unstable data taking conditions were excluded from the analysis. We required events to satisfy good run, good spill, and no error conditions.

Trigger

As mentioned in Sec. 4.3, multiple triggers were used during data taking for various purpose of studies. The trigger cut selected physics trigger events during the spill on period for data analysis.

5.3.2 Trigger Bias Removal

Event selections associated with triggering were carried out to prevent bias in the analysis.

Total γ Energy ($E_{tot,\gamma}$)

The sum of γ cluster energy ($E_{tot,\gamma} = E_{\gamma 1} + E_{\gamma 2}$) was required to be larger than 650 MeV to prevent trigger bias. As discussed in Sec. 4.5, Fig. 4.7 and Fig. 4.8 showed a smear on the online trigger threshold due to lack of calibration information online. The different timing and gain performance for each detector channel led to the trigger bias.

COE Radius

The online COE radius was defined in Eq. 3.1. Similar to the *Total γ Energy* cut, to reduce the online trigger bias, we required the offline COE to be no less than 200 mm. The offline COE is defined in Eq. 5.35.

$$\text{COE offline radius} = \frac{\sqrt{(E_{\gamma 1}x_{\gamma 1} + E_{\gamma 2}x_{\gamma 2})^2 + (E_{\gamma 1}y_{\gamma 1} + E_{\gamma 2}y_{\gamma 2})^2}}{E_{\gamma 1} + E_{\gamma 2}} \tag{5.35}$$

Average γ Cluster Time

In case two triggers arrived too closed to each other, as shown in Fig. 5.11, both waveforms would appear in its own 64-sample window. These two events could use the same peak for the timing identification, resulting in forming the identical clusters. As mentioned, in Sec. 5.1.1.1, the actual timing of the γ cluster should be around the "nominal time". To prevent duplicating identical events, the average of the two γ cluster timing was restricted to be within 215 ± 15 ns.

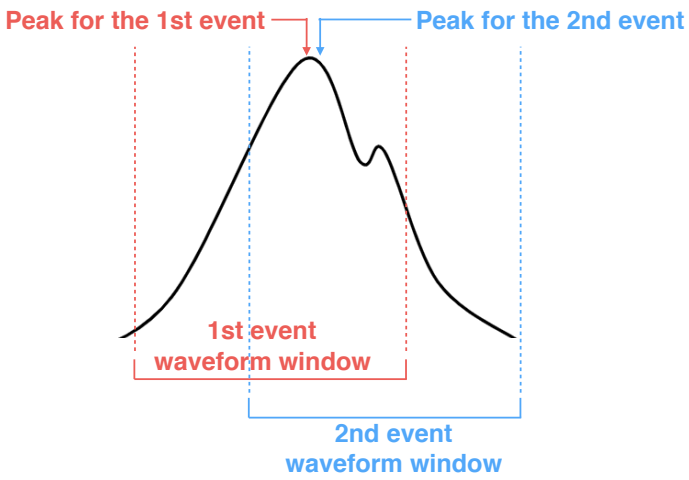

Figure 5.11: Example of two overlapping pulses in the average γ cluster time cut. The first event (red) would use the left peak as its timing. The latter event (blue), due to how the waveforms were overlapped, would choose the same peak as the first event as its timing. In this case, both events yield the same waveform information for the channel and results in cluster duplication.

5.3.3 Kinematic Cuts

The kinematic cuts used the CsI calorimeter information for event selection and two types of cuts were applied. One was to ensure γ cluster quality by checking the agreement of data with the MC simulation. The other type of cut sets served to distinguish $K_L \to \pi^0\nu\overline{\nu}$ from other background events.

5.3.3.1 γ Cluster Quality Selections

γ Energy (E_γ)

The energy of each photon was required to be greater than 100 MeV and smaller than 2000 MeV, in order not to use photons with poor energy and position resolution.

γ Cluster Position (x_γ, y_γ)

To prevent the electromagnetic shower leakage of the γ clusters towards outside

of the CsI calorimeter, we rejected γ clusters located near the inner or outer edges of the CsI calorimeter. This cut was also referred as the "CsI fiducial cut". For each γ cluster, its hit positions, x_γ and y_γ, each was required to be at least 150 mm away from the beam axis, and the distance to the beam axis ($\sqrt{x_\gamma^2 + y_\gamma^2}$) was required to be no more than 850 mm.

γ Cluster Distance

Distance between two γ clusters on the surface of the CsI calorimeter was required to be no less than 300 mm to prevent misidentification of one γ cluster into two.

γ Cluster Distance from Dead Channels

To prevent miscalculation of photon energies and positions in the reconstruction, the minimum distance between a γ cluster to its nearest dead channel was required to be at least 53 mm apart.

5.3.3.2 Background Sources Distinction

γ Projected Opening Angle ($\theta_{proj,\gamma}$)

The projected opening angle measured the opening angle of two γ tracks projected on the surface of the CsI calorimeter, shown in Fig. 5.8 as θ_{proj}. It can be calculated as

$$\theta_{proj} = \cos^{-1}\left(\frac{\vec{r_1}\cdot\vec{r_2}}{|\vec{r_1}||\vec{r_2}|}\right), \tag{5.36}$$

and was required to be less than 150°, where the i-th photon position from the beam axis is $\vec{r_i} = (x_i, y_i)$. It aimed to reduce the background from $K_L \to 2\gamma$, where the two photons from such decay gave a projected opening angle of 180° due to the zero transverse momentum from the K_L.

$E_\gamma\theta_\gamma$

Mispairing of photons can occur in the $K_L \to 2\pi^0$ decay during the reconstruction, where photons originated from different π^0s were paired for reconstruction, called the "odd pairing", as detailed in Sec. 8.3.2. An effective rejection to "odd

pairing" events was to require a minimum value for the product of the energy (E_γ) and the angle created by the reconstructed photon tracks (θ_γ, equivalent to θ_{12} in Fig. 5.8). The value of the product was required to be no less than 2500 MeV·deg.

E_γ Ratio

Energies for two photons are generally not extremely asymmetric. Similar to the $E_\gamma\theta_\gamma$ cut, the E_γ ratio cut was to reduce the "odd pairing" backgrounds from $K_L \to 2\pi^0$ decays, as detailed in Sec. 8.3.2. It required the ratio of the energies for two photons (E_1/E_2) be no less than 0.2, where $E_2 > E_1$.

π^0 Kinematic

This cut was designed to suppress backgrounds resulted from halo neutrons hitting the CV detector and generate $\eta \to 2\gamma$ decays. These background events were referred as "CV-η" events. The cut was applied on the regions in the $P_T^{\pi^0}/P_z^{\pi^0}$ – $Z_{vtx}^{\pi^0}$ plot and the E_{π^0} – $Z_{vtx}^{\pi^0}$ plot, as shown in Fig. 5.12. The variables $P_z^{\pi^0}$ is the longitudinal π^0 momentum and E_{π^0} is the π^0 energy.

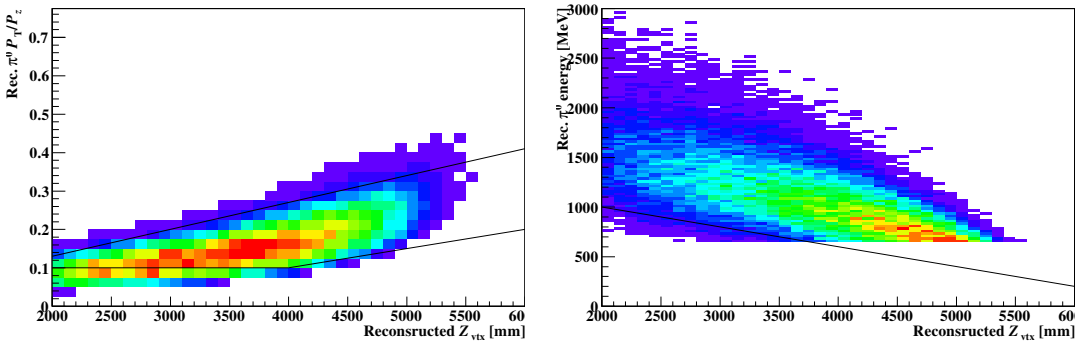

Figure 5.12: Accepted regions on the π^0 kinematic cut [51]. The figures show the MC simulation of $K_L \to \pi^0\nu\overline{\nu}$. In the left figure, region between two black lines were accepted. In the right figure, region above the black line was accepted.

γ Cluster RMS (RMS_γ)

To reject clusters created by hadronic shower, the root mean square (RMS) of the cluster, represented as RMS_γ, was calculated using each crystal's energy and distance from the COE radius, as shown in Eq. 5.37. The variable e_i

denotes the energy of the i-th crystal contained in the cluster. The variable R_i is the distance between the i-th crystal position (x_i, y_i) to the COE position $(x_{COE,\gamma}\ ,\ y_{COE,\gamma})$ of the corresponding crystal, as defined in Eq. 5.38 to Eq. 5.40. The variable e_i represents the energy of the i-th crystal.

$$RMS_\gamma = \sqrt{\sum_i \frac{e_i R_i^2}{\sum_j e_j}} \tag{5.37}$$

$$R_i^2 = (x_i - x_{COE,\gamma})^2 + (y_i - y_{COE,\gamma})^2 \tag{5.38}$$

$$x_{COE,\gamma} = \sum_i \frac{e_i x_i}{\sum_j e_j} \tag{5.39}$$

$$y_{COE,\gamma} = \sum_i \frac{e_i y_i}{\sum_j e_j} \tag{5.40}$$

Hadronic clusters, such as neutron clusters, tend to have a small cluster RMS and can be rejected by requiring the cluster RMS to be no less than 10 mm.

γ Cluster Size

Same methodology as the γ *Cluster RMS* cut. To reject potential hadronic clusters, this cut required a cluster to contain at least 5 CsI crystals.

Vertex Time Difference ($\Delta T_{vtx,\gamma}$)

To ensure two photons originated from a common π^0, difference of each γ cluster reconstructed vertex time (Eq. 5.25) to the reconstructed event vertex time (Eq. 5.26), $\Delta T_{vtx,\gamma} = |T_{vtx,\gamma} - T_{vtx}^{K_L}|$, was required to be no more than 1 ns. In the case of $K_L \to \pi^0\nu\overline{\nu}$ decay, the vertex time and position of the K_L was the same as π^0, as described at the end of Sec. 5.1.3.4. Event reconstruction involving treating accidental hits such as charged particles or neutrons as the clusters often result in a difference in the reconstructed vertex time. This cut guaranteed all photons were generated at the same time.

γ Cluster Shape χ^2 ($\chi^2_{shape,\gamma}$)

This cut variable was represented as χ^2_{shape}. A study on γ cluster transversal

shapes was carried out to reject clusters that did not originate from a single photon. Various single photon energy, position, and angle were used in the MC simulation and compared to the templates. Detail of the study can be found in Ref. [54]. This cut was effective in differentiate clusters formed by a single photon from other particles such as charged pions, neutron, and multiple photons. The maximum of the shape χ^2_{shape} value was required to be less than 4.6.

γ Cluster Shape Discrimination Value (CSD_γ)

The cut used neural network to distinguish photon clusters from neutron clusters using kinematics and cluster shape. The neutral network study used the results from the MC simulations as photon training samples and the Z0 Al target data as neutron samples. Variables of photon/neutron energy, position, and incident angle were used. Similar to the χ^2_{shape} *Cut*, this cut can be used to distinguish clusters formed by a single photon from other particles such as charged pions, neutron, and multiple photons. A value larger than 0.8 was required to reduce neutron clusters.

γ Cluster Pulse Shape Discrimination (PSD_γ)

A study of waveform pulse shape on the CsI calorimeter was carried out to distinguish photons from neutrons. The 10-pole Bessel function filter inside the ADCs turned the waveforms into Gaussian shapes. To study the change of the pulse shape, especially in the tail region of the waveforms, an asymmetric Gaussian function shown in Eq. 5.41 was used for fitting.

$$A(t) = |A| \exp\left(-\frac{(t-t_0)^2}{2\,\sigma^2(t)}\right) \tag{5.41}$$

$$\sigma(t) = \sigma_0 + a(t-t_0) \tag{5.42}$$

The variable $|A|$ is the pulse height of the Gaussian waveform, t_0 is the timing of the peak, σ_0 represents the width of the pulse shape, and a is the "asymmetric parameter" which represents the asymmetry of the pulse shape. Using

template fitting with photon cluster from $K_L \to 3\pi^0$ decay and neutron cluster from Z0 Al target data as control samples, the fit parameter σ_0 and a can be obtained to determine the likelihood of the cluster type. The pulse shape likelihoood was defined using these fitted parameters for every crystal inside each cluster. The variable that distinguishes the most between photon and neutron clusters was the energy-based likelihood calculation using the accumulated energy distribution in each CsI crystal as a probability density function [55]. It was used in combination with the minimum χ^2 estimation, which used total energy and cluster timing information, as inputs to the neural network [56] with a single output variable to distinguish between electromagnetic shower (e.g. photon cluster) and hadronic shower (e.g. neutron cluster). This output variable, pulse shape likelihoood ratio (PSLR), was required to be larger than 0.1. Detail studies are described in Sec. 8.4.1 and in Ref. [50].

γ Incident Angle χ^2 ($\chi^2_{\theta,\gamma}$)

The variable was expressed as χ^2_θ. To reduce events from halo neutrons hitting the CV detector and generating π^0 or η which further decay into 2 photons. These events were referred as "CV-π^0" and "CV-η" backgrounds. The reconstructed photon incident angle was compared to the output of the neural network training. This cut required a value to be less than 4.5.

$\eta - \theta$ χ^2

To remove the same background source as the γ *Incident Angle* χ^2 (χ^2_θ cut, a study on the opening angle using both the π^0 mass and the η mass was carried out. Manipulating Eq. 5.21, the opening angle can be represented in Eq. 5.43.

$$\cos\theta_{\pi^0} = 1 - \frac{M^2_{\pi^0}}{2E_{\gamma 1}E_{\gamma 2}} \tag{5.43}$$

Different coordinates on the CV detector were used in the opening angle study. Difference between the opening angles that are less than 0.1 was considered to be the η vertex candidate. The χ^2 was calculated using the same method as

that in χ^2_θ. This cut required a value larger than 17.

Table 5.2: A list of trigger bias and kinematic cut requirements for $K_L \to \pi^0\nu\overline{\nu}$.

Cut	Requirement
Trigger Bias Removal	
$E_{tot,\gamma}$	≥ 650 MeV
Offline COE Radius	≥ 200 mm
Average γ Cluster Time	$< 215 \pm 15$ ns
Kinematic Cuts	
γ Cluster Quality Selections	
E_γ	$100 \text{ MeV} \leq E_\gamma \leq 2000 \text{ MeV}$
(x_γ, y_γ)	$\lvert x_\gamma \rvert \geq 150$ mm, $\lvert y_\gamma \rvert \geq 150$ mm $\sqrt{x_\gamma^2 + y_\gamma^2} \leq 850$ mm
γ Cluster Distance	≥ 300 mm
γ Cluster Distance from Dead Channels	≥ 53 mm
Background Sources Distinction	
$K_L \to 2\gamma$ *Background*	
$\theta_{proj,\gamma}$	$\leq 150°$
$K_L \to 2\pi^0$ *Background*	
$\mathrm{E}_\gamma\theta_\gamma$	$\geq 2500\,\mathrm{MeV}\cdot\mathrm{deg}$
E_γ Ratio	≥ 0.2
Neutron Background	
π^0 Kinematic	$(P_T^{\pi^0}/P_z^{\pi^0}) - Z_{vtx}^{\pi^0}$ and $E_{\pi^0} - Z_{vtx}^{\pi^0}$ shown in Fig. 5.12
RMS_γ	≥ 10 mm
γ Cluster size	≥ 5
$\Delta T_{vtx,\gamma}$	≤ 1 ns
$\chi^2_{shape,\gamma}$	< 4.6
CSD_γ	> 0.8
PSD_γ	> 0.1
$\chi^2_{\theta,\gamma}$	< 4.5
$\eta - \theta$ χ^2	> 17

5.3.4 Veto Cuts

Other than event selection using kinematic variables, the CsI calorimeter and the veto detectors can be used for vetoing, as described in this section. The signature of the $K_L \to \pi^0\nu\overline{\nu}$ decay is to observe "π^0 and nothing". Hence, we shall see no

activities on the veto detectors. The veto cuts used in the analysis were exclusive - if an event has the energy on the threshold or on the edge of the timing window, it will not be vetoed. The energy and timing veto were applied based on different detectors and some were adjusted to remove certain backgrounds. Detail background studies are discusses in Ch. 8.

5.3.4.1 CsI Calorimeter Veto

Extra Cluster

In a $K_L \to \pi^0\nu\overline{\nu}$ decay, two γ clusters should be observed on the CsI calorimeter. Extra clusters may appear due to accidental hits not related to the K_L activity, or resulted from photons originated from $K_L \to 3\pi^0$ or $K_L \to 2\pi^0$ decay. To reject such events, timing of extra clusters was required to be at least 10 ns apart from the reconstructed K_L (π^0) vertex time. Since no single-crystal cluster was allowed and the minimum energy for a cluster seed was 3 MeV[1], the minimum energy of an extra cluster was 6 MeV (formed by two crystals).

Isolated Hit Crystal

As described in Sec. 5.1.3.1, isolated hit crystal was used as veto. Isolated crystals could be resulted from the accidental hits not related to K_L activities, or from the electromagnetic showers of photon hits. A MC simulation study of the characteristics on the isolated hit crystal around photon clusters was carried out to reduce such events, as shown in Fig. 5.13. Isolated hit crystals with its timing no more than 10 ns apart from its nearest cluster time were rejected using the criteria in Eq. 5.44, where $E_{isolate}$ is the energy of the isolated hit crystal and d is the distance to its nearest cluster.

$$E_{isolated} = \begin{cases} 10 \text{ MeV}, & d \leq 200 \text{ mm} \\ 13.5 - 0.0175\, d \text{ MeV}, & 200 \text{ mm} < d < 600 \text{ mm} \\ 3 \text{ MeV}, & d \geq 600 \text{ mm} \end{cases} \tag{5.44}$$

[1]See Sec. 5.1.3.1

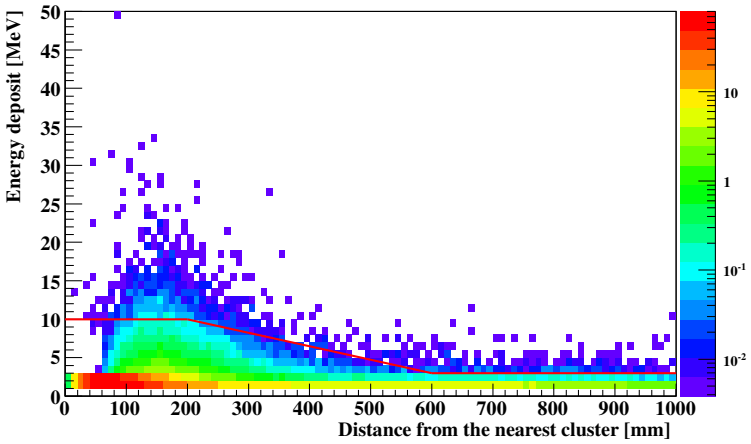

Figure 5.13: Isolated hit crystal veto [51]. This figure shows the distribution of the energy and distance from the nearest cluster to the isolated hit crystal using the $K_L \to \pi^0\nu\overline{\nu}$ MC simulation. Red line shows the isolated hit crystal cut described in Eq. 5.44. Events above the red line was rejected.

5.3.4.2 Other Detectors Veto

The detector energy and timing identification process was discussed in Sec. 5.1.2. The "veto timing", t_{mod}^{veto}, was calculated for each detector module to reject events with extra particles hitting on the veto detectors. Considering the time of flight (TOF), the t_{mod}^{veto} was calculated using Eq. 5.45, where t_{mod} is the detector module time, T_{vtx} was defined in Eq. 5.26, L is the distance between the reconstructed photon track length and the detector module, and c is the speed of light. The definition of L varied upon different detector designs.

$$t_{mod}^{veto} = t_{mod} - \left(T_{vtx} + \frac{L}{c}\right) \tag{5.45}$$

MB and BCV

In case of the MB and the BCV detector, the L value was calculated as

$$\begin{aligned} L &= \sqrt{r_{mod}^2 + (z_{hit} - Z_{vtx}^{\pi^0})^2} \\ &= \sqrt{r_{mod}^2 + (z_{mod} + z_{center} - Z_{vtx}^{\pi^0})^2}, \end{aligned} \tag{5.46}$$

where r_{mod} is the inner radius of the MB and BCV detectors.

CV

In the CV detector, L was defined as

$$L_i = \sqrt{x_i^2 + y_i^2 + (z_i - Z_{vtx}^{\pi^0})^2}, \tag{5.47}$$

where for the i-th module, its corresponding L and position are represented as L_i and (x_i, y_i, z_i).

Upstream Detectors

For other detectors located upstream of the CsI calorimeter, especially the FB and NCC detectors, t_{mod}^{veto} was sensitive to the event decay vertex position $Z_{vtx}^{\pi^0}$. To avoid miscalculating of $Z_{vtx}^{\pi^0}$ due to incorrect photon pairing, L was replaced by the distance between the CsI calorimeter and the decay vertex z position (ΔZ), which was defined in Eq. 5.23. Equation 5.48 shows the definition of t_{mod}^{veto} for upstream detectors, which was the difference between the module timing and the averaged clusters time $t_{cluster}$, as defined in Eq. 5.12.

$$\begin{aligned} t_{mod}^{veto} &= t_{mod} - \left(T_{vtx} + \frac{\Delta Z}{c} \right) \\ &\sim t_{mod} - \left(t_{cluster} - \frac{\Delta Z}{c} + \frac{\Delta Z}{c} \right) \\ &= t_{mod} - t_{cluster} \end{aligned} \tag{5.48}$$

Downstream Detectors

For the downstream detectors, L was defined as the distance between the corresponding detector (z_{det}) and the decay vertex ($Z_{vtx}^{\pi^0}$), as shown below.

$$L = z_{det} - Z_{vtx}^{\pi^0} \tag{5.49}$$

The veto requirements varied due to different detector designs. The new BHCV and the BHPV detector veto requirements are discussed below and are shown in Table 5.3.

new BHCV

The satisfy the veto condition in the new BHCV detector, hits on more than one new BHCV module with energy above the threshold was required.

BHPV

The hits in the BHPV detector were defined by "coincidence". The number of coincidence was defined the number of modules a photon hit with in a 10 ns window. Detail of the BHPV detector can be found in Ref. [51].

5.3.4.3 Special Detector Treatment

The veto thresholds were adjusted for certain detector channels due to their performance during data taking, as mentioned in Sec. 4.2. The MB detector ch 39 was a low-gain channel, and the veto timing veto was widen from 30 ns to 100 ns.

Table 5.3: A list of CsI and detector veto requirements for the $K_L \to \pi^0\nu\overline{\nu}$ analysis. Events greater than the energy threshold and located inside the veto timing window were rejected.

Detector	Energy Threshold [MeV]	Veto Timing Window [ns]
CsI (Extra Cluster)	≤ 6	$\lvert t_{cluster} - T_{vtx}^{K_L} \rvert \geq 10$
CsI (Isolated Hit Crystal)	shown in Fig. 5.13	nearest $t_{cluster} \pm 10$
FB	≤ 1	$(35.08 - 20) \leq t_{FB}^{veto} < 66$
FB	≤ 30	35.40 ± 75
NCC	≤ 1	9.32 ± 20.0
MB	≤ 1	38.8 ± 30
MB ch 39	≤ 1	38.8 ± 100
BCV	≤ 1	37.9 ± 30.0
CV	≤ 0.2	53.7 ± 40.0
LCV	≤ 0.6	14.9 ± 15.0
OEV	≤ 1	19.5 ± 10.0
CC03	≤ 3	32.2 ± 15.0
CC04 (Crystal)	≤ 3	4.31 ± 15.0
CC04 (Scintillator)	≤ 1	4.31 ± 15.0
CC05 (Crystal)	≤ 3	-24.3 ± 15.0
CC05 (Scintillator)	≤ 1	-24.3 ± 15.0
CC06 (Crystal)	≤ 3	-21.8 ± 15.0
CC06 (Scintillator)	≤ 1	-21.8 ± 15.0
BHPV	> 2 coincidence	-76.2 ± 7.5
BPCV	≤ 1	21.4 ± 12.0
new BHCV	$\leq 2.21 \times 10^{-6}$ (> 1 module)	-88 ± 12.5
BHGC	≤ 2.5	-77.4 ± 7.5

Chapter 6
Monte Carlo Simulations

In the $K_L \to \pi^0\nu\overline{\nu}$ blind analysis, it is important to understand the Monte Carlo (MC) simulation well and to reproduce data consistent to what was collected before revealing the blinded region. The MC simulation was used to

- Evaluate the normalization mode (Chap. 7)
- Measure the signal acceptance (Chap. 9)
- Estimate the background contribution (Chap. 8).

Details of generating simulations and methods used are discussed in this chapter.

6.1 Overview of the Monte Carlo Simulation

The MC simulation was performed using Geant4 package [57] with version 9.5.2. The procedure of the MC simulations are described as the following steps:

1. Generate a primary beam particle with a pre-known spectrum (Sec. 6.2)
2. Simulate K_L decay and its daughter particles, as well as their interaction with the detectors (Sec. 6.2.3)
3. Convert the simulation results considering detector responses (Sec. 6.4)

A "step" in the simulation represents a stage of a process. When particle interaction or decay occurs, the simulation proceeds to the next "step". The particle information for each "step" i such as energy (e_i), timing (t_i), and interaction or decay positions (x_i, y_i, z_i) were recorded.

Under certain circumstances, simulations cannot be generated realistically either due to limitation of disk storage or the time required to produce the simulation. We used several methods to generate MC simulations efficiently and realistically, as described below.

Full Simulation

Full simulation records all three steps mentioned in the MC generation above. It is the most complete and the most computation expansive simulation.

Fast Simulation

There are five kinds of fast simulations based on detector response[1], detector online thresholds, orders of particle track stacking, and end points of particle tracks. Different requirements and cuts within the five kinds of fast simulations can be made and only the events that satisfied these requirements are fully simulated and saved. Time and data storage required for the fast simulation are less than that of the full simulation.

Recycling Method

The "recycling method" was used to increase statistics. A normal set of MC samples were generated and events that survived under certain requirements, as described in the fast simulation, were selected as random seeds to generate more events of the same kind.

Accidental Overlay

The waveform "masking effect" from accidental activities would be a source of background contribution. An event will not be vetoed if the waveform from the accidental particle (1st event in Fig. 5.11) is larger than that from the real hit (2nd

[1]Two out of five kinds of the fast simulations were used at this level

event in Fig. 5.11), and locates outside the veto timing window. Details are discussed in Sec. 8.2.

The TMon trigger data mentioned in Sec. 4.3.4 were used as for accidental overlay. Random amount of files were chosen and random event in the file was selected as the start of the accidental event seed. The energy of each event in the file was added onto the MC waveform channel by channel. The waveform simulation is described in Sec. 6.5. For detectors using 500-MHz ADC modules, if the hit time in the event from the TMon data was within 10 ns compared to the MC event, the hit energies were merged and the timing was set to be the timing of the first hit. This method was used to reproduce noise from each detector channel.
These methods were not exclusive. Multiple methods can be combined and used in the MC simulation.

6.2 K_L Generation

Due to the complexity and inefficiency of generating K_L produced in the interaction of protons with the T1-target, the K_L was generated at the beam exit. The beam exit was defined to be the end of the second collimator, located 18.493 m downstream from the T1-target.

6.2.1 K_L Momentum Spectrum

The K_L momentum distribution was measured with a spectrometer and the CsI calorimeter in the engineering run in February, 2012, prior to the installation of the other detectors [54]. The K_L momentum spectrum was obtained and converted to that at the end of the second collimator by reconstructing $K_L \to \pi^+\pi^-\pi^0$ and $K_L \to \pi^+\pi^-$ events. The result is shown in Fig. 6.1.

The K_L momentum spectrum was fitted with an asymmetric Gaussian waveform defined Eq. 6.1 and Eq. 6.2, where dN/dp denotes the K_L momentum distribution, N_0 is the arbitrary scale factor, p is the incident K_L momentum, μ is to the peak of the

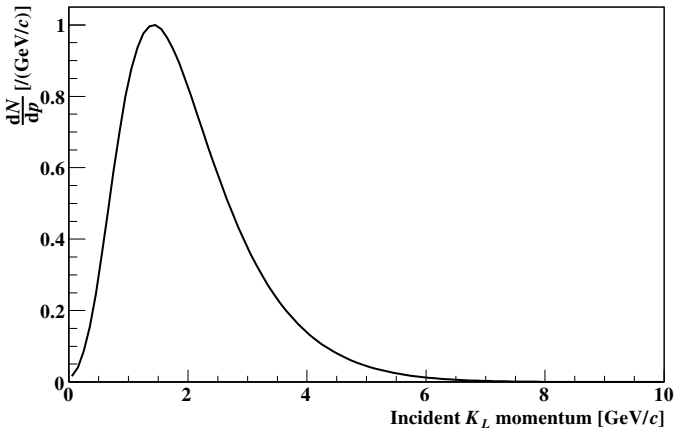

Figure 6.1: The K_L momentum spectrum used in the MC simulation [51].

Gaussian distribution, and σ_0 is the width of the Gaussian distribution corresponding to the peak value μ. The variables A and S are the asymmetric parameters for the Gaussian function. The fitted values are described in Table 6.1.

$$\frac{dN}{dp} = N_o \exp\left(-\frac{(p-\mu)^2}{2\sigma^2}\right) \tag{6.1}$$

$$\sigma = \sigma_0 \left(1 - (A + S \times p)(p - \mu) \right) \tag{6.2}$$

Table 6.1: Fit parameters.

Fit Parameter	Value	Unit
μ	0.05 ± 0.02	GeV/c
σ_0	0.02 ± 0.02	GeV/c
A	0.02 ± 0.01	–
S	0.01 ± 0.01	$(\mathrm{GeV/c})^{-1}$

6.2.2 K_L Incident Position and Direction

A simplified optical simulation was used to generate K_L incident position and direction. The "target image" was used to uniformly generate K_L, as shown in Fig. 6.2.

It had the dimension of ±9.1 mm in the x direction, and ±1.0 mm in the y direction. An imaginary aperture was placed at the narrowest position of the collimator, which corresponded to z = 7 mm. The extrapolated x and y ranges were required to be within ±7.7 mm and ±12.5 mm, respectively. The K_L vertex and direction were randomly generated and the track was extrapolated towards downstream detectors.

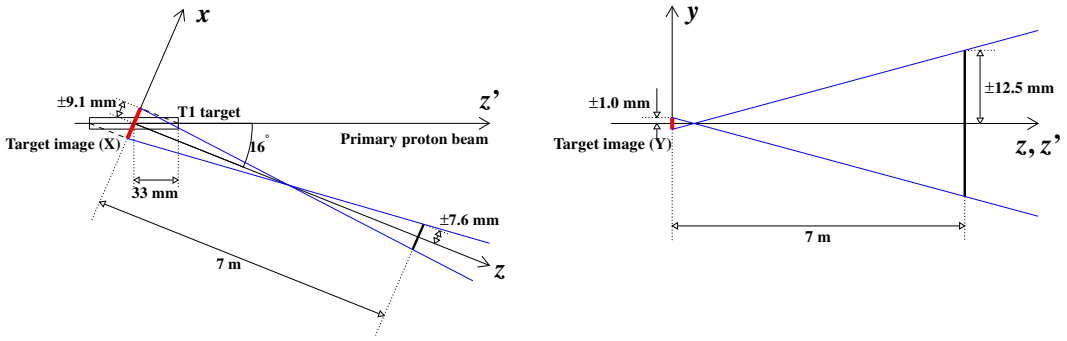

Figure 6.2: Illustration of the target images [51]. The left figure shows the target image on the x-z plane and the right is the y-z plane. The K_L mesons that passed the imaginary aperture (black bar) were used as incident K_L.

6.2.3 K_L Decay and Particle Interaction with Material

The K_L decays, daughter particle decays, and particle interactions with materials were simulated using the Geant4 package. The K_L decay vertex was randomly generated with the probably function in Eq. 6.3, where L is the K_L flight length, c is the speed of light in vacuum, τ is the lifetime of K_L in its own reference frame, and γ is the Lorentz factor, where $\gamma = \frac{1}{\sqrt{1-\beta^2}} = \frac{1}{\sqrt{1-\left(\frac{v}{c}\right)^2}}$ and v is the speed of K_L.

$$P(L) = \exp\left(\frac{L}{c\gamma\tau}\right) \tag{6.3}$$

Different K_L decay modes and their branching ratio was considered in the K_L

simulation. Each decay mode was analyzed separately for different studies mentioned in Chap.7 and Chap. 8. The interaction with air and detector materials, such as energy loss, scattering, regeneration of secondary particles, decays, and absorption were also taken into account. The cross section and momentum of initial and daughter particles were considered in each "step" in the simulation. The same procedure was repeated until the energy dissipated or the particle went outside the decay volume. Due to the difficulty of predict hadronic interaction and the energy range of our interests were in or below GeV levels, we used the Geant4 QGSP_BERT package [58] to simulate hadronic interaction.

6.3 Neutron Beam Generation

To simulate halo neutron that came along with the beamline, fast simulation technique was adopted and neutrons with energy of 1 GeV were generated at position of (1, 3.5, -1507) mm and propagated downstream. Neutron background from interaction with the NCC detector was simulated. For downstream neutron-induced background, detailed in Sec. 8.4.1, Z0 Al target data mentioned in Sec. 4.4 were used as neutron samples to generate the simulation.

6.4 Detector Responses

The MC simulation generated by the Geant4 package was ideal. In order to study the realistic interaction with detectors, we considered detector responses including position resolutions, timing shift due to light propagation, detector timing resolution, and photon statistics effect in the PMT.

For detectors other than the BHPV and the BHGC detector, which are Cherenkov detector, a timing difference between the timing of particle-detector interaction and detection of the particle exists. Scintillation light inside the detectors from the energy deposited by an incident particle travels slower than the speed of the incident particle due to light propagation process, as illustrated in Fig. 6.3. This effect was

considered in each simulation "step" by adding proper time delay according to the interaction position and readout direction. The "effective speed of light", which is the propagation speed of the scintillation light, was measured for each detector and summarized in Table. 6.2. As for Cherenkov detectors, particle travels faster than the speed of light inside the detector material and effective speed of light correction is not needed. Considering detector responses, the energy and timing observed in each detector PMT (e'_i, t'_i) can be obtained from the information of each "step" i, $(e_i, t_i, x_i, y_i, z_i)$, as mentioned in Sec. 6.1. Detector response at "step" i, where the particle interaction with detectors occurs, are discussed in this section. The detector energy and timing resolution are denoted as σ_e and σ_t. Detectors name and positions corresponded to these notations are denoted in the subscripts or superscript, if indicated. These representations are used throughout this section.

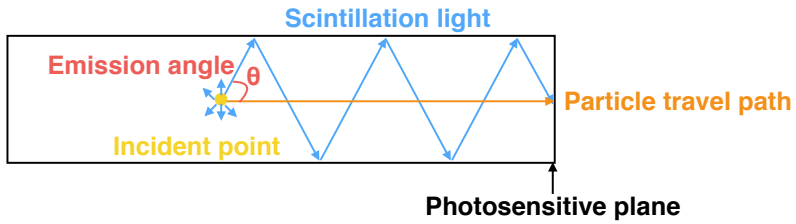

Figure 6.3: Illustration of light propagation inside a detector. Scintillating light traveled in a longer path compared to the incident particle travel path to the photosensitive plane, where the PMT was located. The effective speed of light was corrected by the index of refraction (n) and the emission angel θ.

Table 6.2: A list of effective speed of light for each detector.

Detector	Notation	Effective Speed of Light [mm/ns]
CsI (small crystal)	v_{CsI}^{small}	91.0
CsI (large crystal)	v_{CsI}^{large}	95.9
MB/BCV	$v_{MB/BCV}$	168.1
CV/LCV/OEV	$v_{CV/LCV/OEV}$	177
FB	v_{CC03}	181
CC03	v_{CC03}	88.3
BPCV	v_{BPCV}	168.1

6.4.1 CsI Calorimeter

Timing Correction

The simulated timing for the CsI calorimeter is described in Eq. 6.4 and Eq. 6.5.

$$t_i' = t_i + \Delta t_i + \text{Gaussian}(\sigma_t(E)) \tag{6.4}$$

$$\Delta t_i = \frac{|z^{CsI}_{downstream} - z_i|}{v_{CsI}} \tag{6.5}$$

The parameter Δt_i is the time delay due to light propagation, $z^{CsI}_{downstream}$ represents the z position of the downstream edge of the CsI calorimeter, where the PMT is located. The Gaussian function was used as the smearing effect. It gave a distribution of the timing resolution based on energy defined in Eq. 6.6. The σ_t is in unit of ns, E is the detector measured energy in the unit of MeV, $\oplus$ represents the quadrature sum, $a = 3.63318$, and $b = 5.00$. The performance on the CsI calorimeter and its timing and energy resolution were evaluated. Detailed studies can be found in Ref. [59, 60].

$$\sigma_t(E) = \frac{a}{\sqrt{E}} \oplus \frac{2b}{E} \tag{6.6}$$

Energy Correction

Light yield has a position dependence based on the hit positions. To study this attenuation effect, a study was performed using ^{137}Cs radioactive source which emits photon with 662 MeV. Detailed studies can be found in Ref. [51, 59, 61]. Equation 6.7 describes the energy observed at the detector PMT after correction, where C is the calibration constant, $Y_k(z)$ is the light yield at the k^{th} CsI crystal with a z dependence, and $\bar{Y}(z)$ is weighted averaged light yield with positions[1]. This energy correction considered both the light yield propagation and the photon statistic effect.

[1]Light yield was 9 photonelectron (p.e.) / MeV

$$e'_i = C \times \frac{\text{Poisson}(e_i \times Y_k(z))}{\overline{Y}(z)} \tag{6.7}$$

Equation 6.8 defines the energy resolution of the CsI calorimeter, where $\oplus$ is a quadrature sum and the values of the fitted parameters are listed in Table 6.3 [60].

$$\frac{\sigma_E}{E} = \frac{a}{\sqrt{E}} \oplus \frac{b}{E} \oplus c \tag{6.8}$$

Table 6.3: Fit parameters of the energy resolution of the CsI caloriemter.

Fit Parameter	Value
a	$(1.26 \pm 0.03)\%$
b	$(0.13 \pm 0.03)\%$
c	$(0.76 \pm 0.09)\%$

6.4.2 MB and BCV

Timing Correction

The MB and the BCV detectors are dual-end readout system. The light propagation and attenuation effect were more significant in these detectors compared to others due to the length of these long modules. Timing for each end of the PMT readout was corrected with effective speed of light, v_{MB}, and used for both the MB and the BCV detectors. This value was determined from the cosmic ray data [52]. The timing correction is the same for both detector, as described in the following equations:

$$t'_{i,\,upstream} = t_i + \frac{|z_i - z^{MB\,/\,BCV}_{upstream}|}{v_{MB}} \tag{6.9}$$

$$t'_{i,\,downstream} = t_i + \frac{|z^{MB\,/\,BCV}_{downstream} - z_i|}{v_{MB}} \tag{6.10}$$

where $t'_{i,\,upstream}$ ($t'_{i,\,downstream}$) are the upstream (downstream) PMT readout timing

for the detector, and $z^{MB\,/\,BCV}_{upstream}$ ($z^{MB\,/\,BCV}_{downstream}$) is the z position of the upstream (downstream) edge of the MB or the BCV detector.

Energy Correction

The energy was equally shared by the two PMT readout ends and weighted based on the interaction z position. The energy correction for each end, $e'_{i,\,upstream}$ ($e'_{i,\,downstream}$), are described in the following equations:

$$e'_{i,\,upstream} = \frac{e_i}{2}\,\exp\left(\frac{-\Delta z_i}{\Lambda + \alpha\,\Delta z_i}\right) \tag{6.11}$$

$$e'_{i,\,downstream} = \frac{e_i}{2}\,\exp\left(\frac{\Delta z_i}{\Lambda - \alpha\,\Delta z_i}\right) \tag{6.12}$$

$$\Delta z_i = z_i - \frac{z^{MB\,/\,BCV}_{upstream} + z^{MB\,/\,BCV}_{downstream}}{2} \tag{6.13}$$

The coefficients in shared the same value as that listed in Table. 5.1.

6.4.3 CV

Timing Correction

The CV detector also had dual-end readout system, with a short-fiber side and a long-fiber side on each module. Two sets of timing and energy correction were evaluated. In real data, the timing calibration was adjusted so that the timing detector from each side of the readout are the same when energy deposit occurs at position $(x_0, y_0) = (0, 0)$. Variables Δx and Δy in Fig. 6.4 denote the distance between the incident position to x_0 and y_0, respectively. The signs of Δx and Δy are defined to be positive if the incident position is located on the short-fiber side and negative for the long-fiber side. The readout timing correction for the short-fiber side (Δt^s_i) and the long-fiber side (Δt^l_i) are defined in Eq. 6.14 and Eq. 6.15, respectively. The variable v_{CV} is the effective speed of light inside the fiber. The same equations were used for

the timing correction in both x and y direction, by simply substituting the direction variable.

$$\Delta t_i^s = \frac{-\Delta x}{v_{CV}} \tag{6.14}$$

$$\Delta t_i^s = \frac{\Delta x}{v_{CV}} \tag{6.15}$$

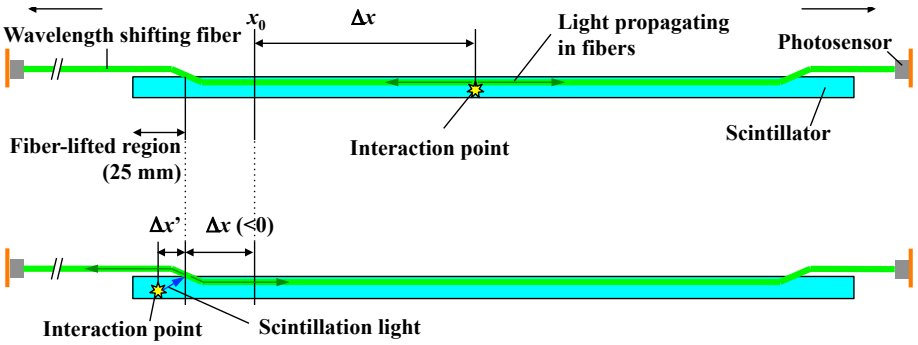

Figure 6.4: Schematic view of light propagation in the CV detector. The short-fiber side is located on the right and the long-fiber side is located on the left. The photosensors on each end are where the PMT received signals from the scintillating light. The timing is adjusted to be the same as the incident point locates at x_O. Propagation path of scintillator light was considered based on the incident positions (Δx and $\Delta x'$). The same illustration applied to (Δy and $\Delta y'$) as well.

The timing correction assumed the interaction time of the incident particle was the same as the emission time in the wavelength shifted fibers. However, the timing corrections were adjusted in case of the incident particle hit the edge of the CV module, where the fiber did not exist. The timing delay due to light propagation in the scintillator was added in Eq. 6.14-6.15 and describes as follows:

$$\Delta t_i^s = \frac{\Delta x'}{v'_{CV}} - \frac{\Delta x}{v_{CV}} \tag{6.16}$$

$$\Delta t_i^s = \frac{\Delta x'}{v'_{CV}} + \frac{\Delta x}{v_{CV}} \tag{6.17}$$

where the effective speed of light in the scintillators was assumed to be the same of

that in the wavelength shifted fibers in the CV detector ($v'_{CV} = v_{BCV}$).

The corrected timing for the short-fiber side (t'^{s}_{i}) and the long-fiber side (t'^{l}_{i}) can be written as

$$t'^{s,l}_{i} = t_i + \Delta t^{s,l}_{i} + \text{Gaussian}(\sigma_t), \tag{6.18}$$

where t_i is the incident timing for the i-th "step" of the simulation. A Gaussian function was used to smear the timing correction. The timing resolution for the CV detector, σ_t, is independent of the energy deposited and has a value of 1.28863 ns.

Energy Correction

The energy correction took the position dependence of the incident particle as well as photon statistics in consideration. The Poisson distribution with energy and light yield dependence was used for energy correction, described as follows:

$$e'^{s,l} = \text{Poisson}(e_i \times Y^{s,l}_{CV}) \times c^{s,l}\, Q^{s,l}_{1\,p.e.}, \tag{6.19}$$

where $e^{s,l}$ is the corrected energy readout for each side or the detector, $e^{s,l}_{i}$ is the incident energy at the i-th "step" in the simulation, $Y^{s,l}_{CV}$ is the absolute light yield per unit energy deposited at the corresponding position and module. The light yield at different position within each module with 50 mm increments were measured prior to the construction of the KOTO detector system [35]. The parameter $c^{s,l}$ denotes the calibration constant for each module and has a unit in MeV/ADC-count. The parameter $Q^{s,l}$ is the gain factor which converted the photoelectron (p.e.) into energy and has a unit of ADC-count/p.e. The energy detected in the CV detector is shared between both sides of the readout.

6.4.4 Other Detectors

Detector responses were not implemented for the NCC, CC04, CC05, and CC06 detectors. Accidental overlay added in the detector response for the beam hole detec-

tors such as new BHCV and BHPV. Detail studies of timing and energy correction can be found in Ref. [41, 51].

Timing Correction

Detectors with single-end readout system used similar timing correction method. The readout system was located at the upstream side for the FB and the BPCV detector, and on the downstream side for the LCV, OEV, and CC03 detector. The timing correction for these detectors are described in Eq. 6.20∼6.24.

$$\text{FB}: \quad t_i' = t_i + \frac{|z_i - z^{FB}_{upstream}|}{v_{FB}} \tag{6.20}$$

$$\text{LCV}: \quad t_i' = t_i + \frac{|z^{LCV}_{downstream} - z_i|}{v_{LCV}} + \text{Gaussian}(\sigma_t(e_i)) \tag{6.21}$$

$$\text{OEV}: \quad t_i' = t_i + \frac{|z^{OEV}_{downstream} - z_i|}{v_{OEV}} \tag{6.22}$$

$$\text{CC03}: \quad t_i' = t_i + \frac{|z^{CC03}_{downstream} - z_i|}{v_{CC03}} \tag{6.23}$$

$$\text{BPCV}: \quad t_i' = t_i + \frac{|z_i - z^{BPCV}_{upstream}|}{v_{BPCV}} + \text{Gaussian}(\sigma_t) \tag{6.24}$$

The parameter t_i' and t_i are the timing measured by the detector and the particle incident timing at the i-th "step" in the simulation. In the representation of parameters $z^{Detector}_{upstream}$, the *Detector* superscript indicates the name of the detector and *upstream* or *downstream* subscripts represent the position of the upstream or downstream edge of the corresponding detector. The parameter $v_{Detector}$ is the effective speed of light for the corresponding detector, where the LCV and the OEV detector shared the same value as the CV detector. In the LCV detector, smearing effect with

a Gaussian function was used, where its timing resolution is defined as follows:

$$\sigma_t^{LCV}(e) = \begin{cases} \frac{a}{\sqrt{e}} \oplus b & , e \geq 0.1 \text{ MeV} \\ \frac{a}{\sqrt{0.1}} \oplus b & , e < 0.1 \text{ MeV} \end{cases} \tag{6.25}$$

where σ_t is the timing resolution in unit of ns and e is the energy deposited in unit of MeV. The parameters are $a = 1.7656 \text{ ns} \cdot \text{MeV}^{1/2}$ and $b = 1.1984$ ns.

The Gaussian smearing effect in the BPCV detector did not have a dependence on energy. The timing resolution for the BPCV detector was $\sigma_t = 2.02$ ns. The value was obtained from comic run where scintillator counters were placed above the BPCV top module and below the BPCV bottom module. The timing resolution was calculated from timing difference distribution between the top and the bottom module.

Energy Correction

No energy correction was implemented for the OEV detector. The corrected energy for the FB and the CC03 detector are described in Eq. 6.26∼6.23 and others are detailed in Ref. [43, 51].

$$\text{FB}: \quad e_i' = e_i \exp\left(-\frac{z_i - z_{calib}^{FB}}{\lambda_{FB}}\right) \tag{6.26}$$

$$\text{CC03}: \quad e_i' = e_i \, Y(z_i) \tag{6.27}$$

where z_{calib}^{FB} is the z position used to obtain the calibration constant and λ_{FB} is the attenuation length of the FB detector. The variable $Y(z_i)$ is the light yield of the corresponding detector at "step" i in the simulation.

6.5 Waveform Simulation

To study the timing shifts due to waveform pileups from the accidental activities, the simulation outputs were converted into 64-sample waveforms, which were the same as the ADC outputs. The simulated waveform was obtained by sampling the asymmetry Gaussian function, described in Eq. 6.28, every 8 ns.

$$f(t) = \exp\left(-\frac{(t-\mu)^2}{(\sigma_0 + a(t-\mu)^2)^2}\right) \tag{6.28}$$

$$\mu = \mu_0 + t'_i - \delta t + t_{offset}, \tag{6.29}$$

The variable t denotes the timing of the waveform. The parameter μ_0, σ_0, and a are the peak timing, width, and the tail of the waveform obtained by fitting the waveform of the real data channel by channel. In Eq. 6.29, t'_i is the timing response of the i^{th} simulation "step", δt is the timing calibration constant, and t_{offset} is the timing offset adjustment to match the MC simulation timing output to the data timing. The waveform of each i^{th} "step" can be represented as a collection, $a^i_n = (a^i_0, a^i_1, a^i_2, \cdots, a^i_j \cdots, a^i_{63})$, which contained the information of (e'_i, t'_i). Equation 6.30 is a mathematical representation of the waveform collection. Complete waveform information can be obtained by summing over all 64 samples in this collection.

$$a^i_j = e'_i \frac{f(8j)}{\sum_{k=0}^{63} f(8k)}, \ (j = 0, 1, \cdots, 63) \tag{6.30}$$

Chapter 7
Normalization Analysis

Prior to the $K_L \to \pi^0\nu\overline{\nu}$ analysis, the normalization analysis was carried out using minimum bias and normalization triggers of $K_L \to 3\pi^0$, $K_L \to 2\pi^0$, and $K_L \to 2\gamma$ decays, and compare to the MC simulations. The normalization analysis was used to check the MC reproducibility with data, to estimate the total number of K_L, and to study event selection and cut efficiencies. These were further used to evaluate the signal acceptance, validate background estimations from the MC simulations, and convert the number of events observed in the final $K_L \to \pi^0\nu\overline{\nu}$ analysis into the upper limit of its branching ratio.

7.1 MC Simulation Samples

The MC simulations generated for the normalization studies included the main four decay modes of K_L that have contributed to the largest branching ratios: $K_L \to \pi^{\pm}e^{\mp}\nu_e$ ($Ke3$), $K_L \to \pi^{\pm}\mu^{\mp}\nu_e$ ($K\mu3$), $K_L \to 3\pi^0$, and $K_L \to \pi^+\pi^-\pi^0$ decay. It also simulated the normalization modes of $K_L \to 2\pi^0$ and $K_L \to 2\gamma$ decays separately. Table. 7.1 lists the decay modes generated in the MC simulation for the normalization studies and their branching ratios.

7.2 Normalization Factor

The normalization factor is the "effective" number of incident K_L at the beam exit, where "effective" considered the DAQ efficiency. The definition of the normalization

Table 7.1: Decay modes generated for the normalization studies and their branching ratios [8].

Decay mode	Branching Ratio (BR)
$K_L \to \pi^{\pm} e^{\mp} \nu_e$ (K_{e3})	$(40.55 \pm 0.11)\%$
$K_L \to \pi^{\pm} \mu^{\mp} \nu_e$ ($K_{\mu 3}$)	$(27.04 \pm 0.07)\%$
$K_L \to 3\pi^0$	$(19.52 \pm 0.12)\%$
$K_L \to \pi^+ \pi^- \pi^0$	$(12.54 \pm 0.05)\%$
$K_L \to 2\pi^0$	$(8.64 \pm 0.06) \times 10^{-4}$
$K_L \to 2\gamma$	$(5.47 \pm 0.04) \times 10^{-4}$

factor (N_{norm}), or the "number of K_L yield", is the in Eq. 7.1.

$$N_{norm} = \frac{p \times N_{data} \times Purity}{A \times BR} \tag{7.1}$$

$$Purity = \frac{A_{mode} \times BR(mode)}{\sum\limits_{i=All\ modes} A_i \times BR(i)} \tag{7.2}$$

The variable p, N_{data}, $Purity$, A, and BR, are the prescaling factor, the number of remaining events after all selection cuts, purity of data, the acceptance, and the branching ratio of the corresponding normalization mode used in the study. In Eq. 7.2, *mode* is the normalization mode used in the study.

The prescaling factor p had a value of 30 for normalization trigger and 300 for minimum bias trigger, as shown in Sec. 4.3. To purify the normalization decay modes for the study, various kinematic and veto cuts were applied. The same event selection cuts were applied on the MC simulations to check the consistency and to calculate the acceptance, A. The acceptance was defined as the probability of a single incident K_L at the beam exit being detected after applying all event selection cuts. It can be calculated using Eq. 7.3, where the "#" sign represents "number".

$$A = \frac{\#\text{ of events after all cuts}}{\#\text{ of incident } K_L \text{ in MC at beam exit}} \tag{7.3}$$

Validation of the detector system functionality can be done by checking the consistency between three normalization decay modes. Analysis on various measurements in the MC simulations was carried out, scaled to the normalization factor, and compared

to data for consistency check. Detail of these studies are shown in Sec. 7.3. After obtaining the normalization factor and the signal acceptance (A_{sig}), the branching ratio of the $K_L \to \pi^0\nu\overline{\nu}$ can be calculated as

$$BR(K_L \to \pi^0\nu\bar{\nu}) = \frac{N_{sig}}{A_{sig} \times N_{norm}}, \tag{7.4}$$

where N_{sig} is the number of events observed with no background exist in the signal region and N_{norm} was defined in Eq. 7.1. Using the normalization scale factor, common systematic uncertainties in acceptance between the signal and the normalization mode can be cancelled, such as decay probability, veto detector response, DAQ efficiency, accumulated P.O.T., and event selection cuts. The remaining discrepancy between the signal and the normalization mode became the systematic uncertainty, as calculated in Sec. 9.1. To reduce the systematic uncertainties, the normalization mode with the most similar momentum spectrum on the CsI calorimeter after all event selections compared to the $K_L \to \pi^0\nu\overline{\nu}$ decay was chosen to for the normalization factor calculation. The $K_L \to 2\pi^0$ decay satisfied this criteria the most out of the three normalization modes.

7.3 Event Selections for the Normalization Modes

To retain similar event acceptance to that of the $K_L \to \pi^0\nu\overline{\nu}$ decay, some of the event selection requirements between the normalization studies and the $K_L \to \pi^0\nu\overline{\nu}$ analysis were similar. The veto event selection cuts were the same as that used in the $K_L \to \pi^0\nu\overline{\nu}$ analysis, as described and shown in Sec. 5.3.4 and Table. 5.3. They were selected to suppress background and to reduce accidental loss.

The kinematic cuts applied in the normalization analysis can be categorized in three categories: γ, π^0, and K_L. To increase the acceptance, some kinematic cuts were loosen in the normalization analysis. Details of the event selections are described in the following subsections. A summary of the kinematic event selection cuts on the normalization analysis is shown in Table. 7.2.

7.3.1 γ Kinematic Cut

Common event selection variables shared among the normalization studies and the $K_L \to \pi^0\nu\overline{\nu}$ analysis were *Total* γ *Energy* ($E_{tot,\gamma}$), γ *Cluster Position* (x_γ, y_γ), γ *Energy* (E_γ), and γ *Cluster Distance*. The definition of these variables can be found in Sec. 5.3.

7.3.2 π^0 Kinematic Cut

ΔM_{π^0}

This cut aimed to eliminate events reconstructed using the wrong photon combinations in the $K_L \to 3\pi^0$ and $K_L \to 2\pi^0$ decays. As described in Sec. 5.1, the reconstructed π^0 mass was calculated in the second event reconstruction, using the z vertex information obtained from the nominal π^0 mass. The reconstructed π^0 mass was required to be consistent within 10 MeV/c^2 of the nominal π^0 mass (134.9766 MeV/c^2 [8]).

ΔZ_{π^0}

Similar to the goal of the ΔM_{π^0} cut, the reconstructed z positions of the most upstream π^0 and the most downstream π^0 was required to be within 400 mm.

7.3.3 K_L Kinematic Cut

Common event selection variables shared among the normalization studies and the $K_L \to \pi^0\nu\overline{\nu}$ analysis were *Vertex Time Difference* ($\Delta T_{vtx,\gamma}$) and γ *Cluster Shape* χ^2 ($\chi^2_{shape,\gamma}$). The definition of these variables can be found in Sec. 5.3.

ΔM_{K_L}

In the $K_L \to 3\pi^0$ and $K_L \to 2\pi^0$ decays, the reconstructed K_L mass was required to be consistent within 15 MeV/c^2 of the nominal K_L mass (497.614 MeV/c^2 [8]). This cut was not required in the $K_L \to 2\gamma$ decay, as the distribution of the reconstructed K_L mass was not available due to using the nominal K_L mass as constraint in the event reconstruction.

K_L P_T

As described in Sec. 2.2, due to the collimators and efforts to produce the pencil beam, K_L entered the KOTO detector did not possess much transverse momentum (P_T). The transverse momentum of all three normalization modes were required to be no more than 50 MeV/c.

χ^2_{Z,K_L}

The definition of χ^2_{Z,K_L} was described in Eq. 5.30. Similar to the purpose of the ΔM_{π^0} *and the* ΔZ_{π^0} cut described in Sec. 7.3.2, the χ^2_{Z,K_L} cut required the maximum χ^2 value of the z position to be no more than 20.

Reconstructed K_L Z Vertex ($Z^{K_L}_{vtx}$)

To ensure analysis on pure K_L events from the three normalization modes, we required the reconstructed K_L to be inside the decay region to avoid interaction with the detectors, as described in Sec. 2.3. The cut required the reconstructed K_L z vertex ($Z^{K_L}_{vtx}$) to locate within 3000 $\sim$ 5000 mm.

K_L Beam Exit Position ($X^{K_L}_{BeamExit}$, $Y^{K_L}_{BeamExit}$)

The reconstructed K_L incident position located at the beam exit was denoted as ($X^{K_L}_{BeamExit}, Y^{K_L}_{BeamExit}$). The K_L x and y positions at the beam exit can be calculated using similar methods described in Eq. 5.31$\sim$5.34, with the numerators $Z^{K_L}_{vtx}$ and Z_{Target} replaced by Z_{CsI} and $Z^{K_L}_{BeamExit}$. Equation 5.31 and Eq. 5.32 can be rewritten as follows.

$$X^{K_L}_{BeamExit} = X_{COE}\,\frac{Z_{CsI} - Z^{K_L}_{BeamExit}}{Z_{CsI} - Z_{Target}} \tag{7.5}$$

$$Y^{K_L}_{BeamExit} = Y_{COE}\,\frac{Z_{CsI} - Z^{K_L}_{BeamExit}}{Z_{CsI} - Z_{Target}} \tag{7.6}$$

Table 7.2: A list of kinematic cuts used in the normalization analysis. The dash symbol, –, indicates the cut was not used in the corresponding normalization mode. The cut values were shared among all three normalization modes unless otherwise indicated. Symbol * and † represent the cuts commonly used in the $K_L \to \pi^0\nu\overline{\nu}$ analysis, former with the same cut value and latter with different cut value. Detailed $K_L \to \pi^0\nu\overline{\nu}$ event selections and the summary of the cuts and be found in Sec. 5.3 and Table 5.2.

Cut	$K_L \to 3\pi^0$	$K_L \to 2\pi^0$	$K_L \to 2\gamma$
$\boldsymbol{\gamma}$			
$^*E_{tot,\gamma}$		≥ 650 MeV	
$^*(x_\gamma, y_\gamma)$		$\lvert x_\gamma\rvert \geq 150$ mm, $\lvert y_\gamma\rvert \geq 150$ mm $\sqrt{x_\gamma^2 + y_\gamma^2} \leq 850$ mm	
$^\dagger E_\gamma$		≥ 50 MeV	
$^\dagger\gamma$ Cluster Distance		≥ 150 mm	
$\boldsymbol{\pi^0}$			
ΔM_{π^0}	≤ 10 MeV	≤ 6 MeV	–
ΔZ_{π^0}	≤ 400 mm	≤ 400 mm	–
$\boldsymbol{K_L}$			
$^\dagger\Delta T_{vtx,\gamma}$		≤ 3 ns	
$^\dagger\chi^2_{shape,\gamma}$	–	≤ 7	≤ 7
ΔM_{K_L}	≤ 15 MeV/c^2	≤ 15 MeV/c^2	–
K_L P_T		≤ 50 MeV/c	
χ^2_{Z,K_L}	≤ 20	≤ 20	–
$Z^{K_L}_{vtx}$		$3000 \leq Z_{K_L} \leq 5000$ mm	
$(X^{K_L}_{BeamExit}, Y^{K_L}_{BeamExit})$	–	$\lvert X^{K_L}_{BeamExit}\rvert, \lvert Y^{K_L}_{BeamExit}\rvert \leq 50$ mm	–

7.4 Analysis Results of Three Normalization Modes

7.4.1 $K_L \to 3\pi^0$

The $K_L \to 3\pi^0$ decay has six photons and it is relatively free from other background compared to other decay modes. Along with its large branching ratio, it is a good candidate for normalization check.

Figure 7.1 shows reconstructed K_L mass distribution with and without the veto cut. Background events such as accidental hits can be removed. Figure 7.2 shows some of the event selection properties. Data in the accepted region, as listed in Table 7.2, were used for the $K_L \to 3\pi^0$ normalization study.

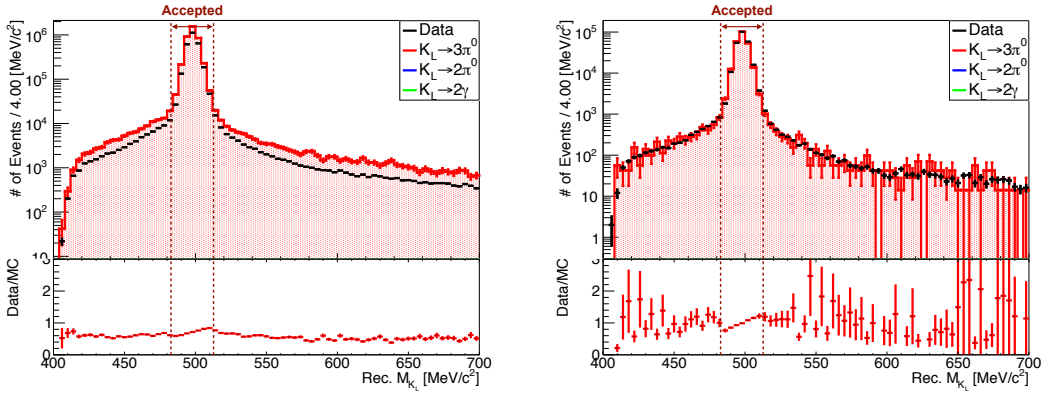

Figure 7.1: $K_L \to 3\pi^0$ reconstructed K_L mass distribution with (right) and without (left) veto cuts.

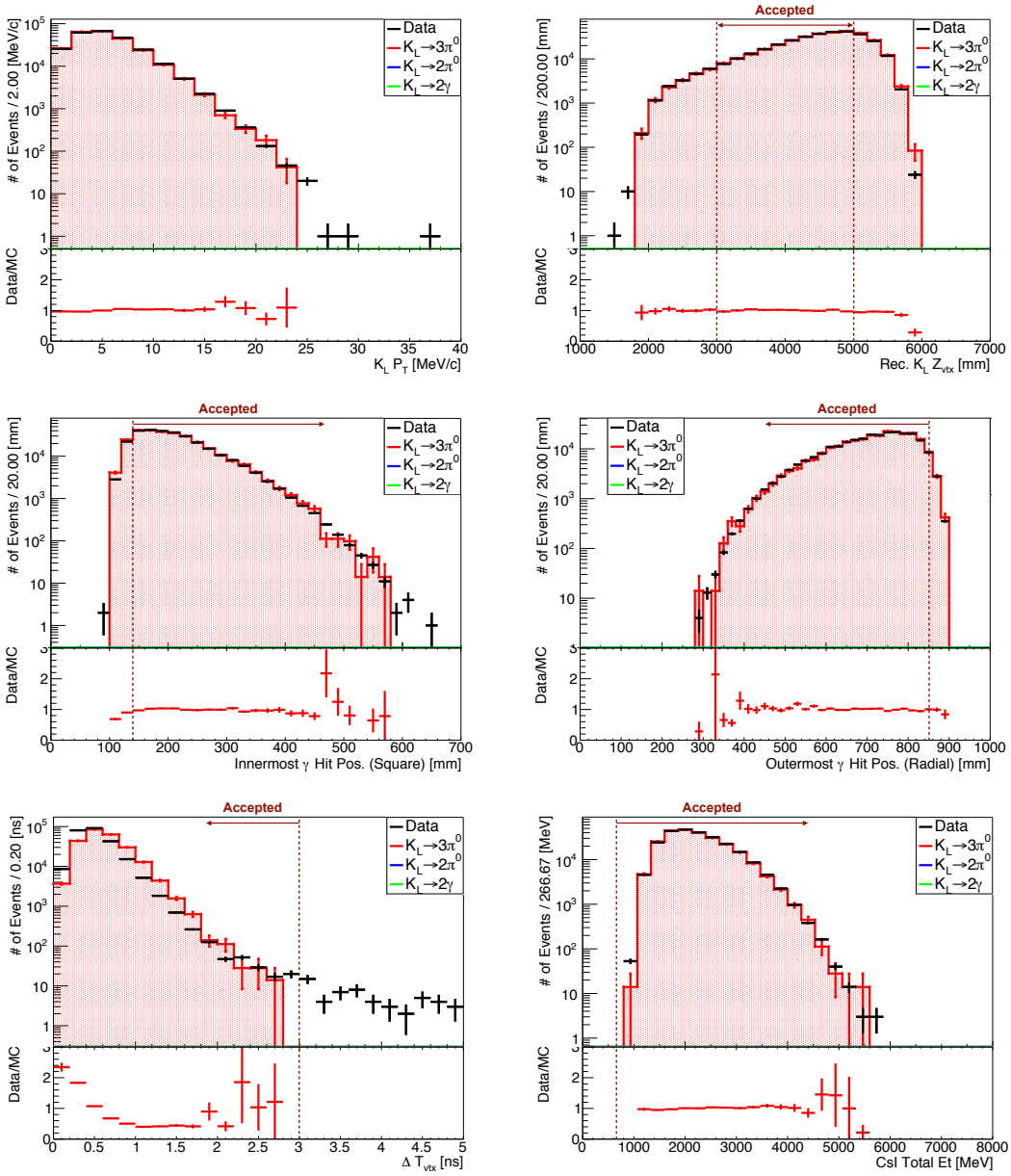

Figure 7.2: Event properties of $K_L \to 3\pi^0$ normalization mode. From left to right, top to bottom are the reconstructed K_L transverse momentum ($P_T^{K_L}$), reconstructed K_L z vertex ($Z_{vtx}^{K_L}$), the innermost photon hit x or y position ($\min(|x_\gamma|, |y_\gamma|)$), outermost photon hit position ($\sqrt{x_\gamma^2 + y_\gamma^2}$), time difference between reconstructed K_L and vertex of each photon ($\Delta T_{vtx,\gamma}$), and total photon energy on the CsI calorimeter ($E_{tot,\gamma}$).

7.4.2 $K_L \to 2\pi^0$

The $K_L \to 2\pi^0$ decay plays the most significant role among the three normalization modes. It decays into four final particles and has similar intrinsic properties and momentum distribution to that of $K_L \to \pi^0\nu\overline{\nu}$ decay, which also has four final particles.

A $K_L \to 3\pi^0$ decay is a source of background contribution in this mode. If fusion cluster occurs, where two photon clusters were to merge into one cluster on the CsI calorimeter, the reconstruction vertex will move towards upstream direction since it can be treated as a $K_L \to 2\pi^0$ decay with high energy. A $K_L \to \pi^+\pi^-\pi^0$ decay where two photons and both π^+ and π^- were to deposit on the CsI calorimeter can lead to the same situation. Branching ratio from these decay modes are at least two orders of magnitude greater than that of $K_L \to 2\pi^0$ decay. Therefore, veto cut selections are important in the study of this normalization mode. In Fig. 7.3, the $K_L \to 3\pi^0$ decay background in the $K_L \to 2\pi^0$ normalization study can be reduced by applying veto cuts. The veto detector energy and timing distribution of the MB and the CV detectors are shown in Fig. 7.4. They can remove extra particle backsplashes other than four photons from the CsI calorimeter. The veto cut selections were made by including the peak of the timing and evaluating the balance between excluding background (narrowing the veto timing window) and keeping the acceptance of the signal (widen the veto timing window). The veto cut values can be found in Table 5.3.

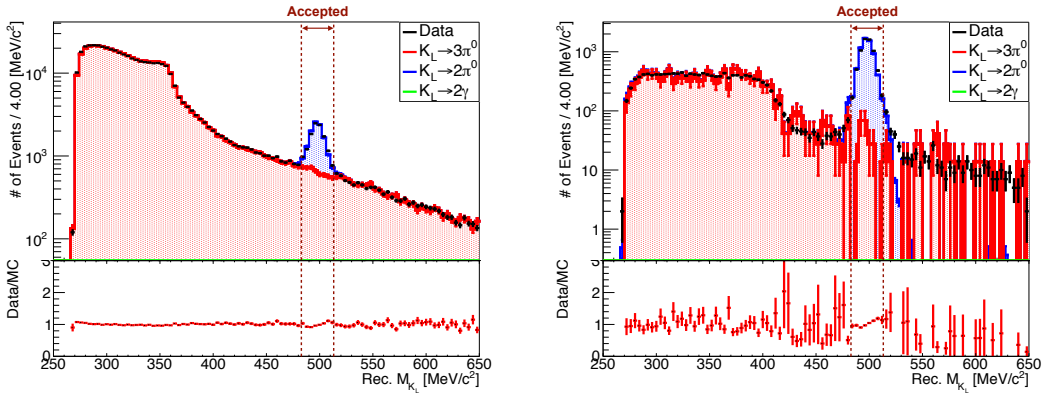

Figure 7.3: $K_L \to 3\pi^0$ reconstructed K_L mass distribution with (right) and without (left) veto cuts.

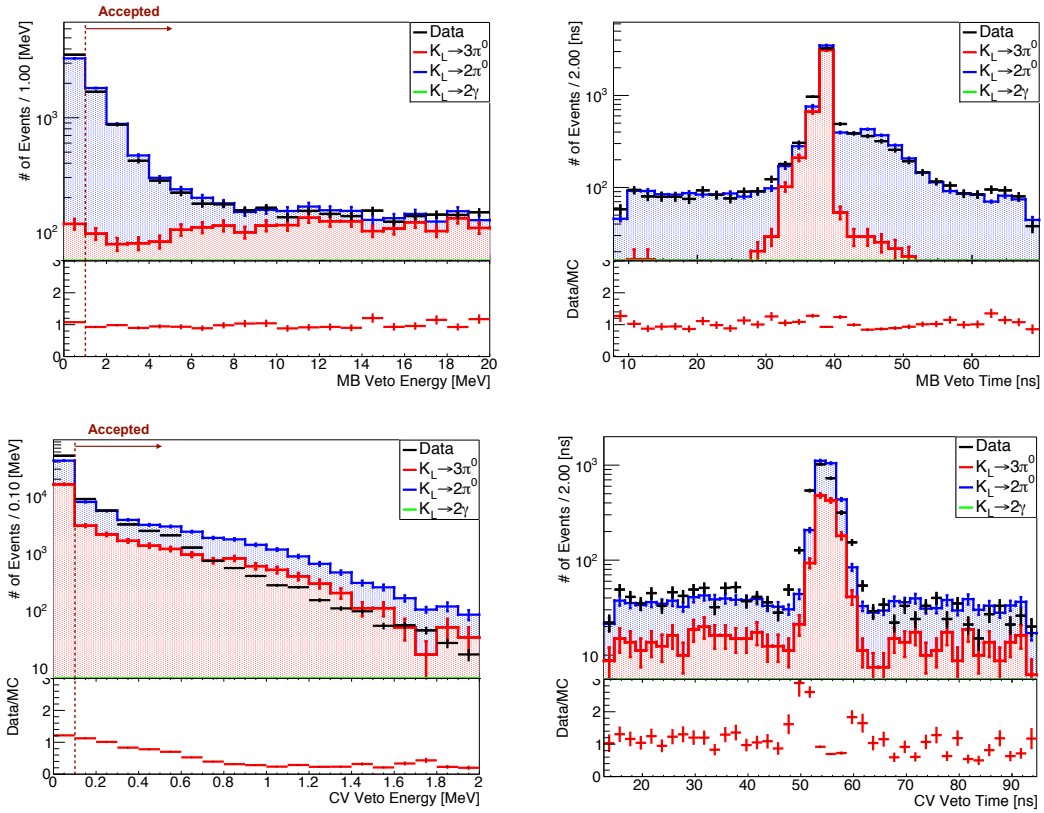

Figure 7.4: Energy and timing distribution of the MB and the CV detectors in $K_L \to 2\pi^0$ normalization study.

The reconstructed K_L transverse momentum and z vertex distribution are shown in Fig. 7.5. The distribution of the reconstructed K_L x and y position at the beam exit came from the structure of the beam and the geometry of the target, where the beam hit a region of the target in the x direction and a point source in the y direction[1].

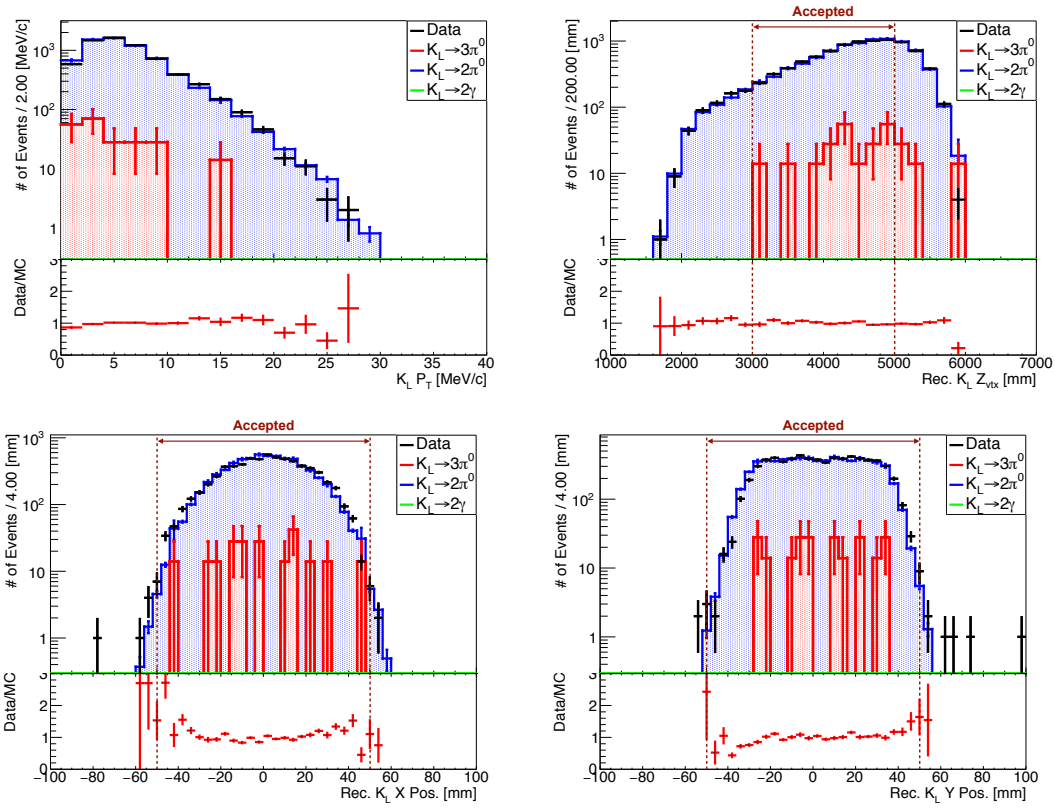

Figure 7.5: Event properties of $K_L \to 2\pi^0$ normalization mode. From left to right, top to bottom are the reconstructed K_L transverse momentum ($P_T^{K_L}$), reconstructed K_L z vertex ($Z_{vtx}^{K_L}$), reconstruct K_L x position at the beam exit ($X_{BeamExit}^{K_L}$), and reconstructed K_L y position at the beam exit ($Y_{BeamExit}^{K_L}$).

7.4.3 $K_L \to 2\gamma$

Figure 7.6 shows the reconstructed K_L transverse momentum and z vertex distribution in the $K_L \to 2\gamma$ normalization study.

[1]See Fig. 2.4

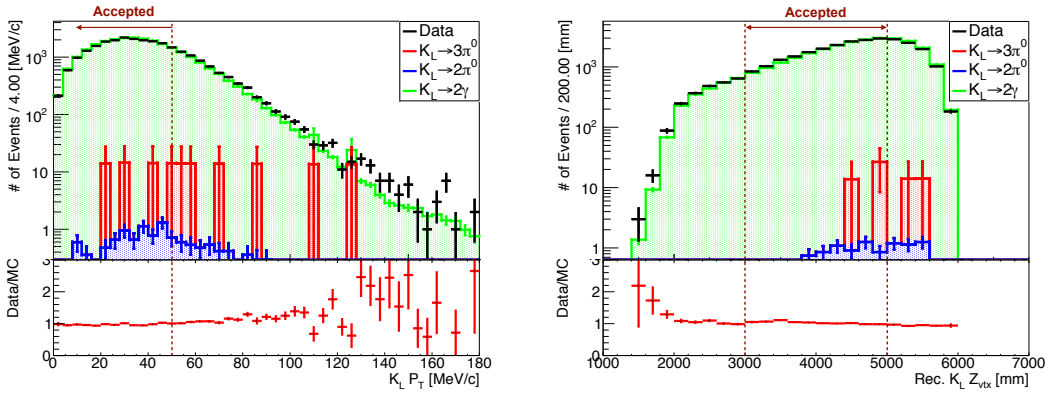

Figure 7.6: $K_L \to 2\gamma$ reconstructed K_L transverse momentum (left) and z vertex (right) distribution.

7.5 K_L Yield and K_L Flux Calculation

The consistency between the three modes was checked. The K_L flux can be calculated using the the number of K_L yield at the beam exit, which was N_{norm} in Eq .7.1. This is the number of events used in the normalization studies after applying the kinematic and the veto cuts. The calculation of acceptance used the same mechanism as that of the $K_L \to \pi^0\nu\overline{\nu}$ decay. Details are described in Sec. 9.1. The K_L flux calculation is described in Eq. 7.7. The K_L flux is in units of "2×10^{14} P.O.T.", which is the J-PARC design value for the number of protons on target per spill. The number of effective P.O.T. (P.O.T.$_{eff}$) took the DAQ dead time into consideration. This number is the integrated P.O.T. for the run period that was used in the study.

$$\begin{aligned} K_L \text{ Flux} &= \frac{N_{norm}}{\text{P.O.T.}_{eff}} \\ &= \frac{p \times N_{data} \times Purity}{A \times BR \times \text{P.O.T.}_{eff}} \end{aligned} \tag{7.7}$$

Data for each beam power in each Run period were evaluated. Table 7.3 lists a summary of the number of K_L at the beam exit, the acceptance, and the K_L flux

calculated for the normalization study in each beam power and Run cycle. Figure 7.7 shows the combined result of K_L yield for each mode from all 2015 runs, which was calculated by taking the weighted average on three normalization modes. The result was $(4.62 \pm 0.02) \times 10^{12}$ for $K_L \to 3\pi^0$, $(4.58 \pm 0.04) \times 10^{12}$ for $K_L \to 2\pi^0$, and $(4.38 \pm 0.02) \times 10^{12}$ for $K_L \to 2\gamma$. In the combined results of all 2015 runs, the total number of K_L yield at the beam exit was 4.62×10^{12} and the K_L flux was $(3.90 \pm 0.10) \times 10^7 K_L$/P.O.T. As mentioned in Sec. 7.4.2, the $K_L \to 2\pi^0$ mode has the closest momentum distribution to that of the $K_L \to \pi^0\nu\overline{\nu}$ decay among all three normalization modes. To reduce the systematic uncertainties, the K_L yield from the $K_L \to 2\pi^0$ normalization study was used to normalize the events in the background studies, which are introduced in Chap. 8.

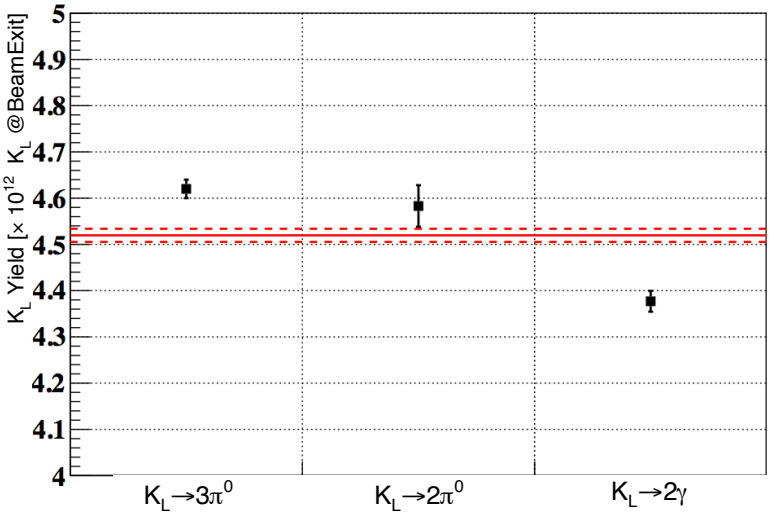

Figure 7.7: Combined K_L yield in all 2015 runs. The solid and dotted red lines show the average and the uncertainty of the K_L yield from three normalization modes.

Table 7.3: Summary of the normalization study for each beam power in each Run period.

Run Condition	$K_L \to 3\pi^0$		$K_L \to 2\pi^0$		$K_L \to 2\gamma$	
	K_L Yield $[\times 10^{12} K_L]$	K_L Flux $[10^7 K_L/2 \times 10^{14}$ P.O.T]	K_L Yield $[\times 10^{12} K_L]$	K_L Flux $[10^7 K_L/2 \times 10^{14}$ P.O.T]	K_L Yield $[\times 10^{12} K_L]$	K_L Flux $[10^7 K_L/2 \times 10^{14}$ P.O.T]
Run 62 24 kW	3.50 ± 0.03	3.35 ± 0.04	3.60 ± 0.13	3.42 ± 0.12	3.32 ± 0.07	3.32 ± 0.08
Run 62 27 kW	3.67 ± 0.03	3.58 ± 0.05	3.79 ± 0.11	3.82 ± 0.12	3.39 ± 0.06	3.38 ± 0.05
Run 63 27 kW	3.56 ± 0.03	3.37 ± 0.04	3.71 ± 0.16	3.64 ± 0.17	3.53 ± 0.09	3.30 ± 0.10
Run 63 29 kW	4.31 ± 0.05	4.34 ± 0.06	4.22 ± 0.20	4.44 ± 0.23	4.25 ± 0.11	4.17 ± 0.12
Run 63 32 kW	4.39 ± 0.04	4.35 ± 0.05	4.39 ± 0.13	4.41 ± 0.12	4.10 ± 0.07	4.13 ± 0.09
Run 64 32 kW	4.23 ± 0.04	3.97 ± 0.05	4.10 ± 0.16	3.83 ± 0.17	3.99 ± 0.09	3.80 ± 0.10
Run 64 39 kW	4.37 ± 0.04	4.19 ± 0.03	4.23 ± 0.10	4.12 ± 0.12	4.14 ± 0.06	4.11 ± 0.07
Run 65 39 kW	4.41 ± 0.04	4.35 ± 0.05	4.43 ± 0.10	4.34 ± 0.11	4.22 ± 0.05	4.11 ± 0.08
Run 65 42 kW	4.40 ± 0.03	4.31 ± 0.05	4.36 ± 0.07	4.33 ± 0.07	4.11 ± 0.03	4.08 ± 0.06

Chapter 8
Background Estimation

Background events from various sources were evaluated and cut sets were developed in the $K_L \to \pi^0\nu\overline{\nu}$ analysis. The goal was to reduce the background events while maximizing the acceptance to signal. Sources of background events to the $K_L \to \pi^0\nu\overline{\nu}$ decay can be categorized into "K_L decay background" and "neutron-included background". Among these background contributions, accidental activities can result in shifts in waveform timing and preserve events that should be vetoed. This chapter details the studies of the background contribution considered in the $K_L \to \pi^0\nu\overline{\nu}$ analysis.

8.1 Strategy

We use both MC simulation described in Chap. 6 (MC-driven) and special run data described in Sec. 4.4 (data-driven) to study background events. In the data-driven technique, data that met certain criteria were used as seeds to generate MC simulation. Details of generation of the simulation are described in each subsection. Accidental activities were considered and added to enhance the approximation of the simulation to data we collected. Various event selections targeting each background source were applied and evaluated. The number of remaining events in the simulation were scaled to the data collected (4.62×10^{12} K_L at the exit of the beam line[1]) to estimate the number of background events. Table 8.1 shows the number of events gen-

[1]See Sec. 7.5

erated for each background source. Details of each background source is introduced in the following sections.

Table 8.1: A list of number of events simulated for each background source. Detail of the data-driven scattered background studying, expressed as *, are described in Appx. A.

Background Sources	# of Events Used	Simulation Method
K_L Decay Background		
$K_L \to \pi^+\pi^-\pi^0$	4×10^{13}	MC, Data*
$K_L \to 2\pi^0$	1.85×10^{14}	MC
$K_L \to 2\gamma$	1×10^{11}	MC, Data*
$K_L \to 3\pi^0$	6×10^{13}	MC
$K_L \to \pi^\pm l^\mp \nu_l$	6×10^{12}	MC
Neutron Induced Background		
Hadron Cluster	1.01×10^{16}	Data
Upstream π^0	1.97×10^{14}	MC
CV$-\eta$	5.62×10^{14}	MC
CV$-\pi^0$	1.40×10^{14}	MC

8.2 Accidental Background

As mentioned in *Average γ Cluster Time* in Sec. 5.3.2 and *Accidental Overlay* in Sec. 6.1, wrong timing extraction from waveforms can lead to retaining events that are ought to be vetoed. This type of situation often occurs in waveform "masking", shown in Fig. 5.11, where overlapping pulses cause difficulty of timing extraction. Accidental activities refer to activities that result in waveforms formed by overlapping pulses, which is a source of background contribution. To study the effect of accidental background, TMon data[1] from Run 65 42 kW beam power were overlaid in the MC simulation for K_L decay background studies.

[1]Described in Sec. 4.3.4

8.3 K_L Decay Background

The K_L decay background sources included $K_L \to \pi^+\pi^-\pi^0$, $K_L \to 2\pi^0$, $K_L \to 2\gamma$, $K_L \to 3\pi^0$, and $K_L \to \pi^\pm l^\mp \nu_l$.[1] Considering veto detector inefficiencies, these events can become background events. Both the MC-driven and data-driven techniques were used to study these background events.

8.3.1 $K_L \to \pi^+\pi^-\pi^0$ Background

Mechanism

The $K_L \to \pi^+\pi^-\pi^0$ decay can give four final particles, with two photons deposited on the CsI calorimeter and two charged pions ($\pi^\pm$) travel down the beam pipe, as shown in Fig. 8.1. If the $\pi^\pm$ were to escape from detection, their missing transverse momentum would push the reconstructed π^0 into the signal region. Downstream detectors such as CC05, CC06, BPCV, and new BHCV were used for vetoing to prevent $\pi^\pm$ escaping from the detection.

This decay mode formed the background contribution in the low P_T region on the $P_T - Z_{vtx}$ plane. The upper bound of the π^0 P_T can be calculated as 133 MeV/c using the conservation of momentum in the transverse direction. If a K_L were to scatter at the vacuum window and the $\pi^\pm$ were not detected, it can be misidentified as a $K_L \to \pi^0\nu\overline{\nu}$ decay due to the apparent large transverse momentum from the π^0 decaying off the beam line. In the $K_L \to \pi^+\pi^-\pi^0$ decay, situation of two photons hitting the CsI calorimeter while the $\pi^\pm$ deposited at the same positions can be neglected since the CV detector had high efficiency in detector charged particles [35].

Method of Estimation

Due to the large branching fraction of the $K_L \to \pi^+\pi^-\pi^0$ decay (12.54% [8]), the "recycling method" mentioned in Sec. 6.1 were used to analyze background from

[1] $K_L \to \pi^\pm l^\mp \nu_l$: l is lepton e or μ, and ν_l is the neutrino associated with the lepton.

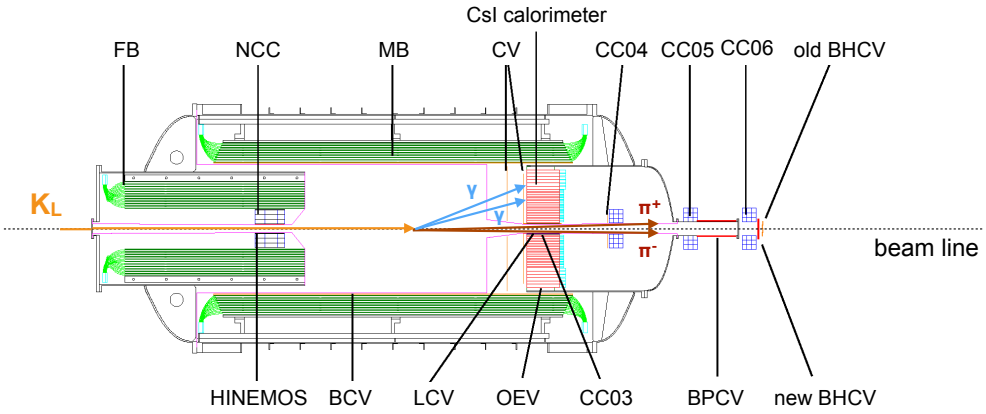

Figure 8.1: Schematic view of $K_L \to \pi^+\pi^-\pi^0$ background.

this decay efficiently and realistically. Since the inefficiency of $\pi^\pm$ detection locating downstream of the CsI calorimeter or the interaction of $\pi^\pm$ with the beam pipe were the contribution to the background, we picked out events with two photons hitting the fiducial region[1] of the CsI calorimeter (from π^0) while the $\pi^\pm$ travel down the beam pipe for the MC simulation. The $\pi^\pm$ was recycled by taking these events and repeatedly simulate the $\pi^\pm$ interaction with the downstream detectors. The procedure followed the steps:

1. $K_L \to \pi^+\pi^-\pi^0$ and the subsequent $\pi^0 \to 2\gamma$ decay were simulated.
2. Events that satisfied at least one of the following two conditions were selected and used as inputs for the full simulation.
   - 2 m $<$ True decay vertex ($Z_{vtx,MC}$) $<$ 7 m
   - Both photons hit the CsI calorimeter
3. Fully simulate two photons and the $\pi^\pm$ using the K_L momentum and K_L decay vertex from these selected events.
4. Background candidate events were selected with the veto cut condition in Table. 5.3 except for CC04, CC05, CC06, and BHPV detectors.
5. The $\pi^\pm$ tracks were extrapolated from the decay vertex position to downstream of the CC03 detector.

[1] $|x|, |y| > 100$ mm, $R = \sqrt{x^2 + y^2} < 900$ mm.

6. Extrapolated $\pi^{\pm}$ were fully simulated with accidental overlay. The π^0 information was reconstructed for the event and analyzed. The same π^0 and $\pi^{\pm}$ information were used 100 times to increase statistics of the MC simulation.

In case of scattered K_L decay, the simulation was generated using the Z0 Al target data. Details are described in Sec. 8.3.3.

Result

Figure 8.2 shows the $K_L \to \pi^+\pi^-\pi^0$ background distribution on the $P_T - Z_{vtx}$ plane. In order to eliminate this background in the low P_T region, we determined the signal region by drawing a boundary for $Z_{vtx}^{\pi^0}$ of 4000 $\sim$ 4700 mm and $P_T^{\pi^0}$ of 130 $\sim$ 150 MeV. The estimated background contribution was 0.05 ± 0.02.

Downstream veto detectors enclosed the KOTO detector and effectively reduced scattered $K_L \to \pi^+\pi^-\pi^0$ background. There was no background observed in the simulation and the upper limit of this background[1] was calculated to be 7×10^{-13} events.

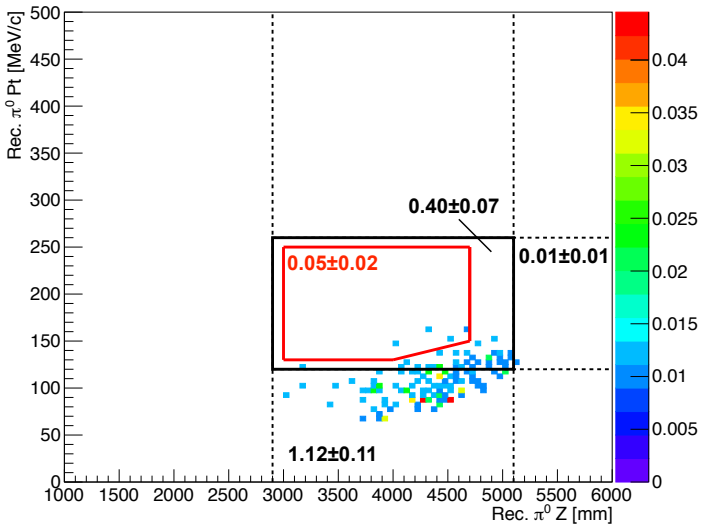

Figure 8.2: $K_L \to \pi^+\pi^-\pi^0$ background estimation. The background contribution from this mode mainly concentrated at the low P_T region.

[1] Appx. A

8.3.2 $K_L \to 2\pi^0$ Background

Mechanism

This background is one of the most dangerous background. There were four final particles and only two photons were available for vetoing. Detector inefficiency was critical for removing this background. A list of main background contribution candidates are listed below.

Missing Photon

- Sampling Effect

  When low energy photon hit the detectors with sandwich-layer structure of active material and inactive converter layers, such as the MB detector, its energy would not be detected when the shower is completely contained in the inactive converter layer. This inefficiency was serious in the MB detector. Another case of not being detected due to sampling was if γ hits a dead channel.

- γ Punch-Through

  In case of a high energy γ, it can escape from detection without interaction if the amount of the material along the incident path of γ is insufficient. This effect is called "Photon (γ) punch-through". It can occur in the MB and the BHPV detector.

- Photonuclear Reaction

  The photonuclear reaction occurs when a high energy photon is absorbed by the nuclei of detector materials and eject protons, neutrons, or other heavier particles from the nuclei. When neutrons were emitted, it will not be detected and dominates the contribution of veto inefficiency in high energy region.

Topology

- Fusion Clusters

  A fusion cluster refers to a cluster on the CsI calorimeter is composed of not just one photon. If three photons deposit on the CsI calorimeter and the cluster

positions were close to each other that fusion occurs, it leaves only one photon for vetoing. Such event can be treated as a two-photon event. Similarly, if all four photons deposit on the CsI calorimeter and generate fusion clusters, it can misidentified as a two-photon event. Fusion clusters can make large contribution to background.

- Odd Pairing

  In the reconstruction of a π^0, even pairing refers to the both photons on the CsI calorimeter came from the same π^0, and odd pairing refers to two photons on the CsI calorimeter came from different π^0s. In case of an odd pairing event, the vertex is not properly reconstructed and can affect its kinematics.

Method of Estimation

Unlike $K_L \to \pi^+\pi^-\pi^0$, $K_L \to 2\pi^0$ decays have small branching ratio (8.64×10^{-4} [8]). It is possible to simulate large number of $K_L \to 2\pi^0$ decays. Fast MC simulation was generated to study the $K_L \to 2\pi^0$ background events. The procedure for the $K_L \to 2\pi^0$ background study followed:

1. The decay of $K_L \to 2\pi^0 \to 4\gamma$ was simulated where the photons stopped at the surface of the detector.
2. Events that satisfied the following criteria were selected for $K_L \to 2\pi^0$ background studies since these assumption would be easily satisfied by this decay mode.
   - -1 m $<$ True decay vertex ($Z_{vtx,MC}$) $<$ 7 m
   - Number of photons hit the CsI calorimeter ≥ 2
   - Total energy of the photons $>$ 400 MeV

To reduce the background events, event selections listed below were applied.

- Low Energy γ

  In order to reduce the inefficiency, the veto energy threshold was set to be tighter than 2 MeV for the FB, MB, and OEV detector.

- γ Punch-Through

  More BHPV modules were added for the 2015 runs to increase the material for γ interaction. An Inner Barrel (IB) detector was built to add on the thickness for the MB detector. It was implemented inside the MB detector in 2016.

- Fusion Clusters

  The χ^2_{shape} and CSD_γ cuts mentioned in Sec. 5.3.3.2 was powerful towards distinguishing fusion clusters from single-photon cluster. It was used to suppress fusion cluster events.

- Odd Pairing

  As mentioned in Sec. 5.3.3.2, $E_\gamma\theta_\gamma$ and E_γ *Ratio* cuts were used to suppress odd pairing events.

Result

Figure 8.3 shows the $K_L \to 2\pi^0$ background distribution on the $P_T - Z_{vtx}$ plane. The $K_L \to 2\pi^0$ background contributions were mainly at the low P_T region and can potentially enter the signal region. The estimated background contribution was 0.02 ± 0.02 events.

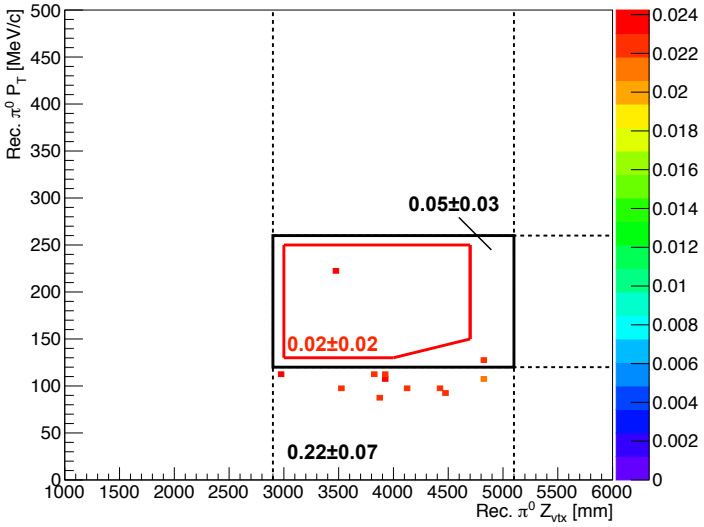

Figure 8.3: $K_L \to 2\pi^0$ background estimation.

8.3.3 $K_L \to 2\gamma$ Background

Mechanism

The $K_L \to 2\gamma$ decay would be a background event if the K_L scatters at the vacuum window and decay off the beam line, as illustrated in Fig. 8.4. The incident K_L has no transverse momentum except for when it scatters. In such case, the two photons on the CsI calorimeter would appear to have large P_T.

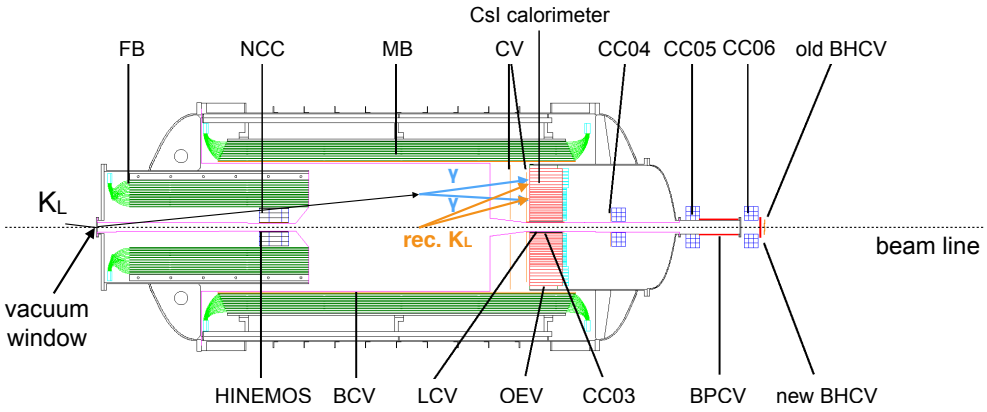

Figure 8.4: Schematic view of scattered $K_L \to 2\gamma$ background.

Method of Estimation

Full simulation of $K_L \to 2\gamma$ decays were simulated for background studies. As mentioned in Sec. 8.3.1, scattered K_L decay with two photons in the final state can appear to possess a large P_T in the event reconstruction. As mentioned in Sec. 5.3.3, the θ_{proj} cut was used to reduce the scattered $K_L \to 2\gamma$ background.

To further study investigate the scattered K_L induced background, a data-driven method using Z0 Al data in Run 78 was carried out. Details are described in Appx. A.

Result

Figure 8.5 shows the $K_L \to 2\gamma$ background distribution on the $P_T - Z_{vtx}$ plane. The estimated $K_L \to 2\gamma$ was 0.02 ± 0.01 events.

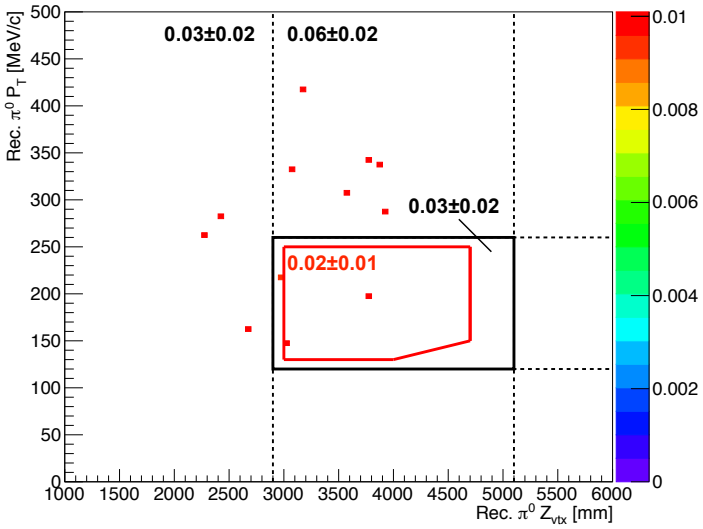

Figure 8.5: $K_L \to 2\gamma$ background estimation.

8.3.4 $K_L \to 3\pi^0$ Background

Mechanism

This decay is considered the cleanest among all K_L decay modes. Since it has six photons, it can easily be rejected by the veto detectors. However, in case of two photons hitting the CsI calorimeter while other low energy photons hit the upstream veto detectors, such as the FB or the MB detector, the veto detector inefficiencies can lead to background contribution[1]. Similar scenario with fusion clusters, which can lead to background contribution if they were created on the CsI calorimeter.
As mentioned in Sec. 8.2, In consideration of accidental activities occur with a $K_L \to 3\pi^0$ event that leaves two photons on the CsI calorimeter, either due to detector inefficiency or fusion clusters, the waveform "masking effect" from the accidental activities would be a source of background contribution.

In Sec. 5.3.2, masking effect in the waveform timing extraction can be a source of the $K_L \to 3\pi^0$ background when there are accidental activities. In the situation of the accidental overlay mentioned in Sec. 6.1, if the first event corresponds to the

[1]See Sec. 8.3.1

accidental particle and the second event belongs to a photon from a $K_L \to 3\pi^0$ decay, this event will not be vetoed.

Method of Estimation

Fast simulation of $K_L \to 3\pi^0$ decays were generated. To study the accidental waveform masking effect, events after applying accident overlay were used as seeds for recycling[1] to increase statistics. The procedure of generating $K_L \to 3\pi^0$ events follows:

1. The decay of $K_L \to 3\pi^0 \to 6\gamma$ was fully simulated.
2. Events that satisfied the following criteria were selected for $K_L \to 3\pi^0$ background studies.
   - Photons on the CsI are within the fiducial area, where $|x|, |y| > 100$ mm, and $R = \sqrt{x^2 + y^2} < 900$ mm.
   - Total energy of the photons > 400 MeV

Result

Figure 8.6 shows the $K_L \to 3\pi^0$ background distribution on the $P_T - Z_{vtx}$ plane. The estimated $K_L \to 3\pi^0$ was 0.01 ± 0.01 events.

8.3.5 $K_L \to \pi^{\pm} l^{\mp} \nu_l$ Background

Mechanism

Based on the design of the KOTO detector, background contribution from this decay mode should be small. It would contribute as background events if two charged photons were not detected by the CV detector and were identified as photons on the CsI calorimeter.

[1] See Sec. 6.1

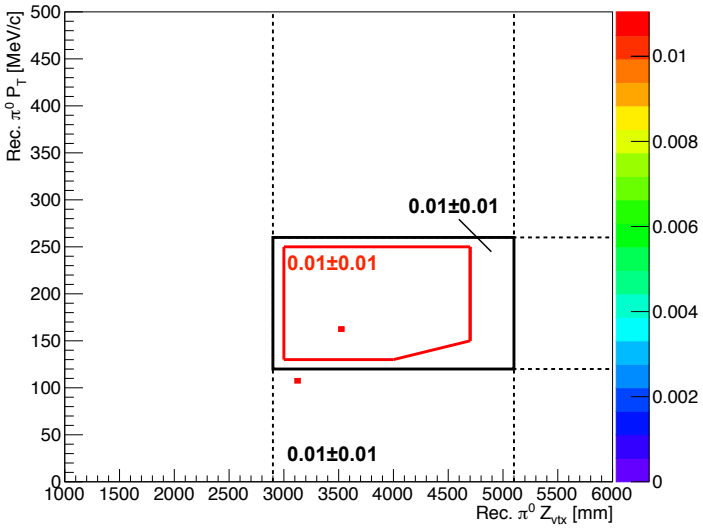

Figure 8.6: $K_L \to 3\pi^0$ background estimation.

Method of Estimation

The $K_L \to \pi^{\pm} l^{\mp} \nu_l$ decays were simulated and the "recycling method" mentioned in Sec. 6.1 was used to increase statistics. Events that were sensitive to the CV detector inefficiency were selected as seeds. The efficiency of the CV detector was high, and the cluster shape related cuts were able to differentiate charged particles from the photons.

Result

No remaining events were observed in the MC simulation after applying all cuts.

8.4 Neutron-Induced Background

Neutron is one of the most dangerous background to the $K_L \to \pi^0 \nu\overline{\nu}$ decay since both events are neutral. Halo neutrons, which refers to neutrons around the beam hole region that entered the KOTO detector decay volume, are one of the most serious background sources. Halo neutrons can interact with detector material and

produced η or π^0 mesons and leave two photons on the CsI calorimeter and introduce background events. They can directly hit the CsI calorimeter and create a hadronic shower. Differentiation between hadron clusters and photon clusters became crucial. We performed studies on the energy showers on the calorimeter, such as Pulse Shape Discrimination (PSD) [50] and Cluster Shape Discrimination (CSD), and developed various cuts to reduce neutron-induced background events. Details on each neutron-induced background scenario are described in this section.

8.4.1 Hadron Cluster Background

Mechanism

Figure 8.7 shows an example of a halo neutron induced background. Direct incidence of halo neutrons onto the CsI calorimeter can lead to hadronic interaction and form a primary cluster. A secondary neutron can be emitted in this interaction and form another cluster. The two clusters on the CsI calorimeter without any activities on the veto detectors can contributed as background.

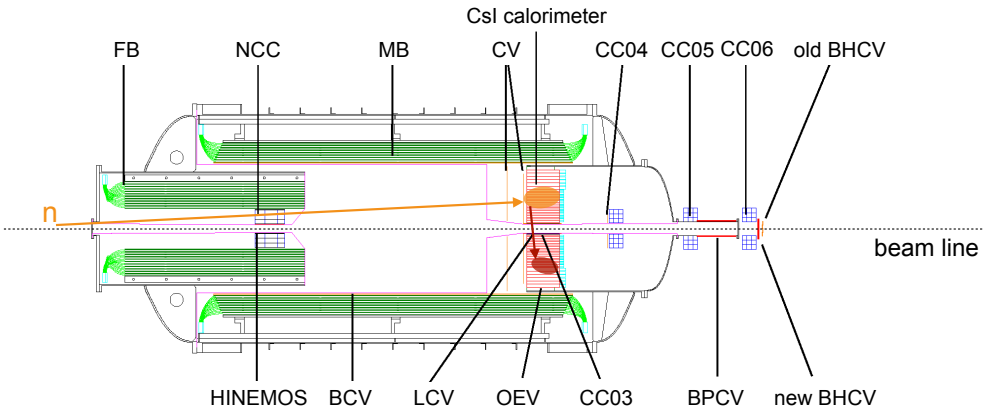

Figure 8.7: Schematic view of halo neutron background. A halo neutron hit the CsI calorimeter and generated a secondary cluster. Event reconstruction with non-zero transverse momentum with only two clusters on the CsI calorimeter can fake a $K_L \to \pi^0\nu\bar{\nu}$ signal.

Method of Estimation

A data driven approach was used to study hadronic cluster background induced by halo neutrons. The Z0 Al target data was used as seeds to generate scattered neutrons. Two-cluster events that passed the selection criteria similar to the signal event were selected as control samples. Studies on the electromagnetic shower created by photons and hadronic shower created by neutrons were evaluated. The *CSD* and *PSD* event selection methods mentioned in Sec. 5.3.3.2 were developed to distinguish these two types of shower on the calorimeter.

Result

Figure 8.8 shows the hadron cluster background distribution on the $P_T - Z_{vtx}$ plane. The estimated number of background was 0.24 ± 0.17 events.

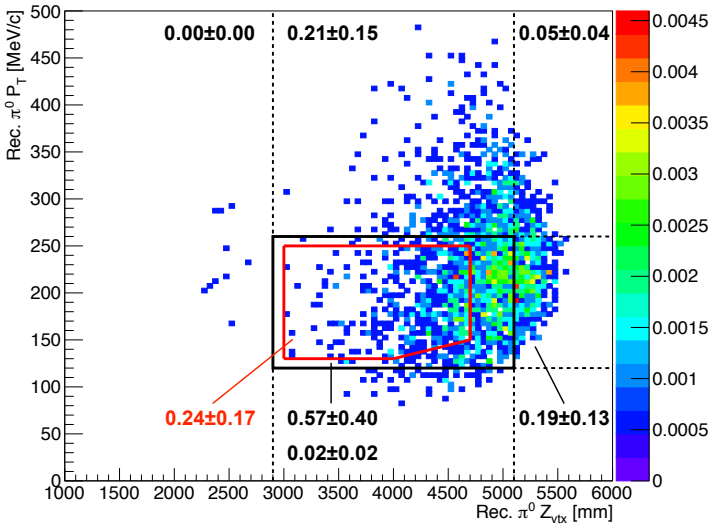

Figure 8.8: Hadronic background estimation.

8.4.2 Upstream π^0 Background

Mechanism

This background was produced by halo neutron interacting with the NCC detector and producing $\pi^0 \to 2\gamma$ in the decay region. If the measured photon energy is smaller due to photo-nuclear interaction in the CsI calorimeter or photon pairing to a secondary neutron interacting in the calorimeter, the reconstructed $Z_{vtx}^{\pi^0}$ would shift downstream into the signal region.

Method of Estimation

Halo neutrons from the result of the beam line MC simulation were used for the study.

Result

Figure 8.9 shows the upstream π^0 background distribution on the $P_T - Z_{vtx}$ plane, which were mostly outside the signal region. The estimated number of background was 0.04 ± 0.03 events.

8.4.3 CV$-\eta$ Background

Mechanism

This background was induced by a halo neutron hitting the CV detector and produce an η meson. In the reconstruction of the $\eta \to 2\gamma$ decay from the CsI calorimeter using π^0 mass would push the decay vertex $Z_{vtx}^{\pi^0}$ upstream in the signal region.

Method of Estimation

Halo neutron with η production were simulated. The opening angle of 2γ on the CsI calorimeter and their incident angle χ^2 were evaluated. As mentioned in

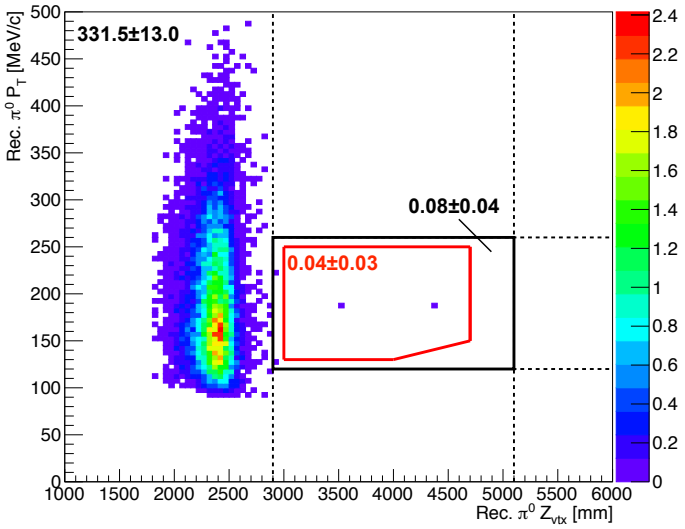

Figure 8.9: Upstream π^0 background estimation.

Sec. 5.3.3.2, the χ^2_θ and $\eta - \theta$ χ^2 cut were developed to suppress such events.

Result

Figure 8.10 shows the CV$-\eta$ background distribution on the $P_T - Z_{vtx}$ plane. The estimated number of background was 0.04 ± 0.02 events.

8.4.4 CV$-\pi^0$ Background

Mechanism

The mechanism of this background is the same of that in the CV$-\eta$ background, as described in Sec. 8.4.3.

Method of Estimation

The method of estimation of this background is the same of that in the CV$-\eta$ background, as described in Sec. 8.4.3.

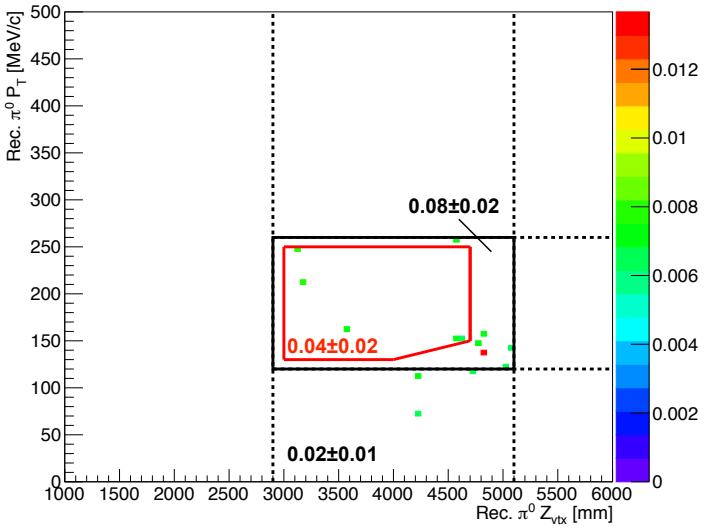

Figure 8.10: CV$-\eta$ background estimation.

Result

Figure 8.11 shows the CV$-\pi^0$ background distribution on the $P_T - Z_{vtx}$ plane. No remaining events were observed in the signal region after applying all cuts. The upper limit was calculated to be 0.08 events at 90% C.L.

8.5 Summary of the Background Estimation

Table 8.2 lists the summary of the estimated number of background events in the signal region after applying all cuts for each background source. Table 8.3 shows the summary of the total number of excepted number of background events in each region on the $P_T - Z_{vtx}$ plane shown in Fig. 8.12. The total background contribution from K_L and neutron were 0.42 ± 0.18.

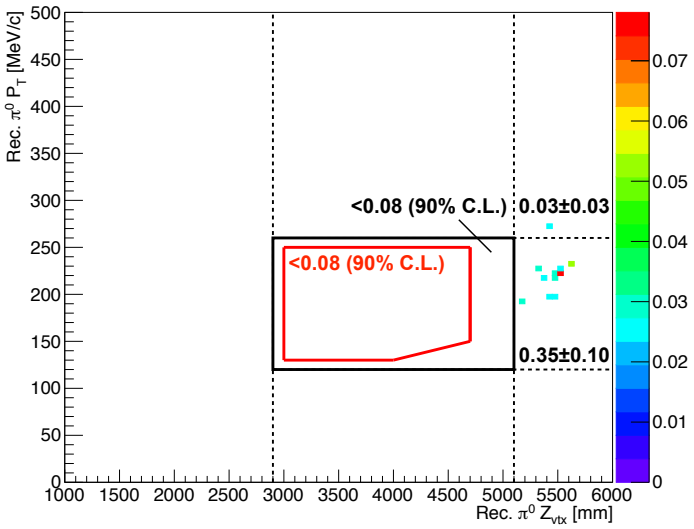

Figure 8.11: CV$-\pi^0$ background estimation.

Table 8.2: Background estimation summary for $K_L \to \pi^0\nu\bar{\nu}$. The number of background events were scaled to data collected, which corresponded to 4.62×10^{12} at the beam exit.

Background Sources	Number of Background Estimated
K_L Decay Background	
$K_L \to \pi^+\pi^-\pi^0$	0.05 ± 0.02
$K_L \to 2\pi^0$	0.02 ± 0.02
$K_L \to 2\gamma$	0.02 ± 0.01
$K_L \to 3\pi^0$	0.01 ± 0.01
$K_L \to \pi^\pm l^\mp \nu_l$	0
Neutron Induced Background	
Hadron Cluster	0.24 ± 0.17
Upstream π^0	0.04 ± 0.03
CV$-\eta$	0.04 ± 0.02
CV$-\pi^0$	0

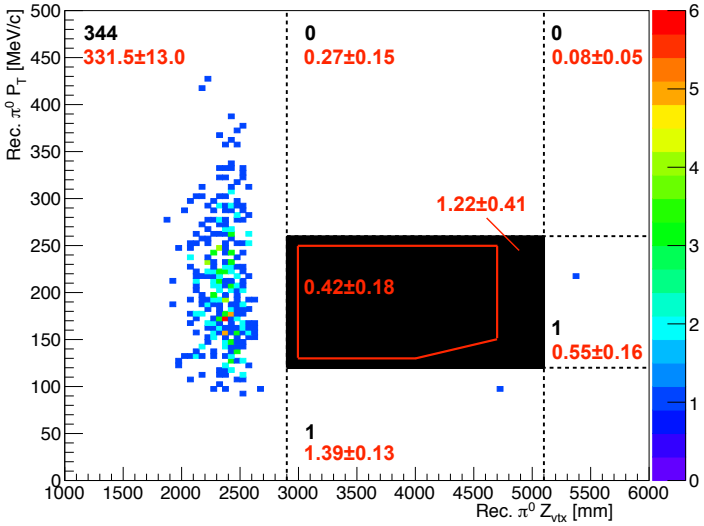

Figure 8.12: Total number of background events in 2015 analysis. These events were normalized to the total number of K_L, obtained from the $K_L \to 2\pi^0$ normalization study at the beam exit. The number of events observed in data in each region (black) agreed with the number of events estimated from the background studies (red).

Table 8.3: Number of background estimated for each region on the $P_T - Z_{vtx}$ plane. The number of background events were scaled to the data collected, which corresponded to 4.62×10^{12} at the beam exit.

Region	Number of Background Estimated
1	331.5 ± 13.0
2	0.27 ± 0.15
3	0.08 ± 0.05
4: Signal Region	0.42 ± 0.18
5: Blind Region	1.22 ± 0.41
6	0.55 ± 0.16
7	1.39 ± 0.13
8	0

Chapter 9
Results and Discussions

Chapter 7 detailed the way to obtain the normalization factor for the $K_L \to \pi^0\nu\overline{\nu}$ analysis. Chapter 8 provided the background estimation methods used for the $K_L \to \pi^0\nu\overline{\nu}$ decay. The number of K_L at the beam exit was 4.62×10^{12} and the total number of estimated background events was 0.42 ± 0.18. The uncertainty for the $K_L \to \pi^0\nu\overline{\nu}$ analysis and the upper limit of the $BR(K_L \to \pi^0\nu\bar{\nu})$ calculation using the results from these two chapters are detailed in this chapter.

9.1 Uncertainties

As mentioned in Sec. 7.2, the $K_L \to 2\pi^0$ decays were used for scaling the number of remaining events to the $K_L \to \pi^0\nu\overline{\nu}$ breaching ratio or its upper limit. This relationship was described in Eq. 7.4, using $K_L \to 2\pi^0$ decay as the normalization mode. The alternative representations and derivation are written in Eq. 9.1 and Eq. 9.2, where N_{sig} is the number of events observed in the signal region, BR is the branching ratio of a decay, A_{sig} is the acceptance of the signal events, and p is the prescaling factor for the $K_L \to 2\pi^0$ decay. The parameter $N_{K_L\to 2\pi^0}$ and $A_{K_L\to 2\pi^0}$ are the number of $K_L \to 2\pi^0$ events and the acceptance for the $K_L \to 2\pi^0$ decay mode in the normalization analysis.

$$\frac{N_{sig}}{BR(K_L \to \pi^0\nu\bar{\nu}) \times A_{sig}} = \frac{p \times N_{K_L\to 2\pi^0}}{BR(K_L \to 2\pi^0) \times A_{K_L\to 2\pi^0}} \tag{9.1}$$

$$\Rightarrow BR(K_L \to \pi^0\nu\bar{\nu}) = \frac{N_{sig}}{p \times N_{K_L\to 2\pi^0}} \times \frac{A_{K_L\to 2\pi^0}}{A_{sig}} \times BR(K_L \to 2\pi^0) \tag{9.2}$$

The acceptance can be broken down as follows:

$$A_{K_L\to 2\pi^0} = A_{geom.}^{K_L\to 2\pi^0} \times A_{\gamma}^{K_L\to 2\pi^0} \times A_{\pi^0}^{K_L\to 2\pi^0} \times A_{veto}^{K_L\to 2\pi^0} \tag{9.3}$$

$$A_{sig} = A_{geom.}^{sig} \times A_{onlineCOE}^{sig} \times A_{\gamma}^{sig} \times A_{\pi^0}^{sig} \times A_{shape}^{sig} \times A_{veto}^{sig}. \tag{9.4}$$

The subscripts describe the type of acceptance, where *geom.*, *onlineCOE*, γ. π^0, *shape*, and *veto* are the acceptance associated with detector geometry, online COE trigger effect (trigger related), γ selections, π^0 kinematic cuts, cluster shape cuts, and veto cuts. The acceptance was evaluated using the MC simulation, or through the comparison between data and the MC simulation. As mentioned in Sec. 7.2, common discrepancies between the data and MC for the $K_L \to 2\pi^0$ and $K_L \to \pi^0\nu\overline{\nu}$ decays can be cancelled and are not needed in the calculation of systematic uncertainty. The systematic uncertainty for the $K_L \to \pi^0\nu\overline{\nu}$ branching ratio was calculated using the quadrature sum of the uncertainties from each acceptance category, as expressed in Eq. 9.5. In the geometric and veto acceptance calculations, $K_L \to 2\gamma$ event were used to substitute $K_L \to \pi^0\nu\overline{\nu}$ decays to evaluate the cut efficiency since both decays yield final product of only two photons and "nothing" else. Details of acceptance in each category and contributions to the systematic uncertainty of $K_L \to \pi^0\nu\overline{\nu}$ are discussed later in this section.

The sources of systematic uncertainty in the $K_L \to \pi^0\nu\overline{\nu}$ analysis can be categorized in Table 9.1. To obtain the uncertainty of the $K_L \to \pi^0\nu\overline{\nu}$ branching ratio, uncertainties from individual term that contributes to the calculation of the $K_L \to \pi^0\nu\overline{\nu}$ branching ratio were summed in quadrature, as described in Eq. 9.5. All terms contributed to the systematic uncertainty of the $K_L \to \pi^0\nu\overline{\nu}$ branching ratio calculation except for $\sigma_{N_{norm}}$, which contributed as statistical uncertainty. Summary of these values and the single event sensitivity, which will be discussed in Sec. 9.2, can be found in Appx. B. The variable σ is the uncertainty and the subscripts indicate the source of each uncertainty, where $A_{K_L\to 2\pi^0}$, A_{sig}, $BR(K_L \to 2\pi^0)$, $Purity$, N_{norm}, and $NormConsistency$ refer to acceptance of $K_L \to 2\pi^0$ normalization, $K_L \to \pi^0\nu\overline{\nu}$ signal acceptance, branching ratio of $K_L \to 2\pi^0$, purity of $K_L \to 2\pi^0$ normalization,

normalization factor mentioned in Sec. 7.2, and consistency from three normalization modes discussed in Chap. 7. In the final uncertainty calculation for $K_L \to \pi^0\nu\overline{\nu}$, the statistical uncertainty was 0.80%, the total system uncertainty calculated was 10.53%, and the total uncertainty was 10.56%.

Table 9.1: Sources of uncertainties in the $K_L \to \pi^0\nu\overline{\nu}$ analysis. This list is a combination from Table 5.2, Table 5.3, and Table 7.2.

Event Selection Type	Cut Variable	Requirement	Systematic Uncertainty
Geometry	See Sec. 9.1.1	K_L Momentum	1.08%
Online Trigger Effect	Average γ Cluster Time	$< 215 \pm 15$ ns	1.94%
	$E_{tot,\gamma}$	≥ 650 MeV	
	Offline COE Radius	$\sqrt{x_{COE}^2 + y_{COE}^2}$	
γ Selection	E_γ	100 MeV $\leq E_\gamma \leq$ 2000 MeV	0.81%
	(x_γ, y_γ)	$\lvert x_\gamma \rvert \geq 150$ mm, $\lvert y_\gamma \rvert \geq 150$ mm	
		$\sqrt{x_\gamma^2 + y_\gamma^2} \leq 850$ mm	
π^0 Selection	$E_{tot,\gamma}$	≥ 650 MeV	5.11%
	$\Delta T_{vtx,\gamma}$	≤ 1 ns	
	γ Cluster Distance	≥ 300 mm	
	E_γ Ratio	≥ 0.2	
	π^0 Kinematic	$(P_T^{\pi^0}/P_z^{\pi^0}) - Z_{vtx}^{\pi^0}$ and $E_{\pi^0} - Z_{vtx}^{\pi^0}$	
	Offline COE Radius	$\sqrt{x_{COE}^2 + y_{COE}^2}$	
	$\theta_{proj,\gamma}$	$\leq 150^\circ$	
	$E_\gamma \theta_\gamma$	$\geq 2500\,\text{MeV} \cdot \text{deg}$	
	γ Cluster Distance from Dead Channels	≥ 53 mm	
Cluster Shape Cut	γ Cluster size	≥ 5	5.08%
	RMS$_\gamma$	≥ 10 mm	
	$\chi^2_{shape,\gamma}$	< 4.6	
	CSD$_\gamma$	> 0.8	
	$\chi^2_{\theta,\gamma}$	< 4.5	
	$\eta - \theta\ \chi^2$	> 17	
	PSD$_\gamma$	> 0.1	
$K_L \to 2\pi^0$ Kinematics	See Table 7.2	π^0 and K_L selections	2.71%
Veto	See Table 5.3	All applied	3.73%

$$\begin{aligned}
\sigma_{total} &= \underbrace{\sigma_{A_{K_L\to 2\pi^0}} \oplus \sigma_{A_{sig}}}_{0.88\%} \oplus \underbrace{\sigma_{BR(K_L\to 2\pi^0)}}_{0.69\%} \oplus \overbrace{\underbrace{\sigma_{Purity}}_{0.38\%} \oplus \underbrace{\sigma_{N_{norm}}}_{0.80\%}}^{\sigma_{N_{K_L\to 2\pi^0}}} \oplus \underbrace{\sigma_{NormConsistency}}_{5.61\%} \qquad (9.5)\\
&= \sigma_{stat.} \oplus \sigma_{sys.}\\
&= \sigma_{N_{norm}} \oplus \sigma_{sys.}
\end{aligned}$$

9.1.1 Geometric Acceptance

The geometric acceptance of $K_L \to 2\pi^0$ and $K_L \to \pi^0\nu\overline{\nu}$ decays were defined as the acceptance of all photons from the decay z vertex range from 3000∼4700 mm and hit the CsI fiducial region[1]. The K_L momentum spectrum parameters μ, σ_0, A, and S in Eq. 6.1 were taken into consideration in the calculation of systematic uncertainty. The geometric acceptance was evaluated using the fast simulation motioned in Sec. 6.1 and the systematic uncertainty was 1.08%.

9.1.2 Online Trigger Effect

The efficiency of the *Average γ Cluster Time* cut affected the acceptance of the online trigger effect. The efficiency ratio is defined in Eq. 9.6 and used in the calculation of acceptance.

$$\epsilon \text{ Ratio} = \left[\left(\frac{\epsilon^{MC}_{K_L\to 2\pi^0}}{\epsilon^{data}_{K_L\to 2\pi^0}} \right) / \left(\frac{\epsilon^{MC}_{K_L\to 2\gamma}}{\epsilon^{data}_{K_L\to 2\gamma}} \right) \right] - 1 \tag{9.6}$$

The efficiency (ϵ) is defined as

$$\epsilon^i = \frac{\#\text{ of events with all cuts}}{\#\text{ of events with all cuts except for the } i^{\text{th}} \text{ cut}}, \tag{9.7}$$

The $K_L \to 2\gamma$ samples were used instead of the $K_L \to \pi^0\nu\overline{\nu}$ decay to evaluate the efficiency ratio between data and MC since both decays have the same final state of leaving only two photons for observation. The systematic uncertainty yield was 0.28%.

The systematic uncertainty for the total energy for the $K_L \to 2\pi^0$ decay was negligible and there was a small uncertainty ($< 0.01\%$) from changing the normalization region in the $K_L \to 2\gamma$ mode.

The online COE effect was evaluated and yield a systematic uncertainty of 1.92%. Details of the methods used can be found in Ref. [51].

[1]See Sec. 5.3.3.1: ($|x|, |y| > 100$ mm and $\sqrt{x^2+y^2} < 900$ mm)

The geometric acceptance is the combined quadratic sums from all three sources. It had a systematic uncertainty of 1.08%.

9.1.3 γ Selection

The $K_L \to 2\pi^0$ events were reconstructed without the photon energy (E_γ) and the CsI fiducial (x_γ, y_γ) cuts. Among these $K_L \to 2\pi^0$ samples, π^0 mesons were extracted as validation samples and compared between data and MC. The acceptance of γ selection has the same definition as that of the cut efficiency in Eq. 9.7, and denoted as A^i. The difference of the γ selection acceptance between data and MC can be calculated to obtain the systematic uncertainty, as described in Eq. 9.8. The total systematic uncertainty was 0.81%.

$$\sigma = \sqrt{\sum_{i}^{All} \left(\frac{A^i_{MC} - A^i_{data}}{A^i_{data}} \right)^2} \tag{9.8}$$

9.1.4 π^0 Selection

The method of acceptance and systematic uncertainty calculation for the π^0 selection was the same as that used in the γ selection, described in Sec. 9.1.3. The π^0 mesons from the $K_L \to 2\pi^0$ decays were extracted as samples and each cut was evaluated. The total systematic uncertainty was summed in quadrature and had a value of 5.11%.

9.1.5 Cluster Shape Cut

The method of acceptance and systematic uncertainty calculation for the cluster shape cut was the same as that described in the π^0 selection (Sec. 9.1.4). The uncertainties for the cluster shape cuts were resulted from the π^0 selection. The total systematic uncertainty was summed in quadrature and had a value of 5.08%.

9.1.6 $K_L \to 2\pi^0$ Kinematics

Same as defined in Sec. 9.1.3, the $K_L \to 2\pi^0$ kinematic cuts were taken into account and evaluated. The systematic uncertainty from the $K_L \to 2\pi^0$ kinematic cut was 2.71%.

9.1.7 Veto Cut

As mentioned in Sec. 9.1.1, $K_L \to 2\gamma$ events were used to calculate the acceptance and propagate error analysis. Common error can be cancelled by taking the acceptance ratio of the $K_L \to 2\gamma$ (to substitute $K_L \to \pi^0\nu\overline{\nu}$ mode) to that of $K_L \to 2\gamma$ (from normalization analysis). The efficiency for each veto cut was calculated and summed in quadrature using Eq. 9.8, with symbol ϵ^i substituting A^i. The combined veto efficiency was treated as the veto cut acceptance. It had the systematic uncertainty of 3.73%

9.1.8 Normalization Mode Consistency

Consistency between three normalization modes was considered in the calculation of the systematic uncertainty. The difference among K_L yield for all three normalization modes in each beam power for each Run period in Table 7.3 was checked. The systematic uncertainty from this contribution was 5.61%.

9.1.9 Other Uncertainty Factors

The uncertainty for the normalization factor, $N_{K_L \to 2\pi^0}$ in Eq. 9.3 and Eq. 9.4, can be written as

$$N_{K_L \to 2\pi^0} = Purity \times N_{norm}. \tag{9.9}$$

The purity for the $K_L \to 2\pi^0$ was evaluated in the normalization study, as described in Sec. 7.2. It had a systematic uncertainty was 0.38%. The normalization factor gave a statistical uncertainty of 0.80%.

9.2 Single Event Sensitivity

The Single Event Sensitive (S.E.S.) was used to the represent the capability of observing $K_L \to \pi^0\nu\overline{\nu}$ events and to calculate the upper limit of the $K_L \to \pi^0\nu\overline{\nu}$ branching ratio [62]. The S.E.S. was calculated based on Eq. 7.4 with $N_{sig} = 1$ and $K_L \to 2\pi^0$ decay mode as the normalization factor defined in Eq. 9.10.

$$\text{S.E.S.} = \frac{1}{A_{sig} \times N_{K_L \to 2\pi^0}} \tag{9.10}$$

The normalizing factor ($N_{K_L \to 2\pi^0}$), corresponding to the total number of K_L at the beam exit among the data analyzed, was obtained in Sec. 7.5 to be 4.62×10^{12}. The breakdown of acceptance (A_{sig}) and corresponding S.E.S. values for each beam power in each Run period is listed in Appx. B. The S.E.S. value in the $K_L \to \pi^0\nu\overline{\nu}$ analysis was obtained as

$$\text{S.E.S.} = (1.30 \pm 0.01_{\,stat.} \pm 0.14_{\,sys.}) \times 10^{-9}. \tag{9.11}$$

The S.E.S. decreased by an order of magnitude compared to the previous value obtained in the 2013 analysis of $(1.28 \pm 0.04_{\,\text{stat.}} \pm 0.13_{\,\text{sys.}}) \times 10^{-8}$ with 100 hours of data collection [22]. The systematic uncertainty is greater than the statistical uncertainty in the results of the KOTO experiment. In setting the upper limit of BR($K_L \to \pi^0\nu\overline{\nu}$) using blind analysis, the systematic uncertainties were determined by cut efficiencies in the normalization studies (Chap. 8). Increase in statistics can improve the systematical uncertainties as versatile cuts values on event selections can be applied. Therefore, accumulating more data is highly desirable in the KOTO experiment.

9.3 Revealing the Signal Region

Knowing the value of S.E.S., the upper limit of the $K_L \to \pi^0\nu\overline{\nu}$ branching ratio can be calculated using the number of events observed in the signal region [62]. Figure. 9.1

shows the summary of the number of estimated background and the observed events in each region.

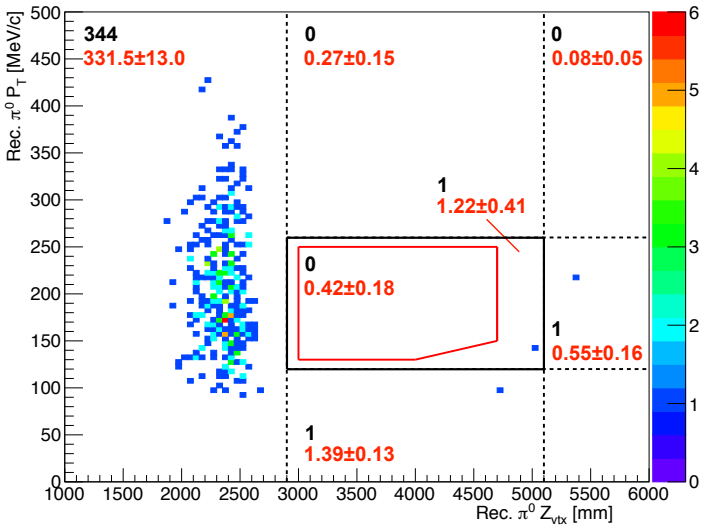

Figure 9.1: Result of 2015 $K_L \to \pi^0\nu\overline{\nu}$ analysis. The number of expected background (red) and the observed events (black) are labeled in each region of the reconstructed π^0 $P_T - Z_{vtx}$ plane. No events were observed in the signal region.

After applying all event selection cuts (Table 5.2 and Table 5.3), no events were observed in the signal region. This result was consistent with our background estimation. The upper limit of the branching ratio was calculated in Eq. 9.12 with 90% C.L. [62]. The variable σ_r is the total uncertainty, which was 10.56%, as mentioned in Sec. 9.1. The upper limit of $BR(K_L \to \pi^0\nu\bar{\nu})$ is 3×10^{-9}, which updated the current value of 2.6×10^{-8} by an order of magnitude [8].

$$\begin{aligned} BR(K_L \to \pi^0\nu\bar{\nu}) \text{ Upper Limit} &= 2.30 \times \left(1 + \frac{1 - \sqrt{1 - 2.30^2 \times \sigma_r^2}}{2.30}\right) \times \text{S.E.S.} \\ &= 3.0 \times 10^{-9} \end{aligned} \tag{9.12}$$

Discussion on calculating uncertainties were discussed in Sec. 9.1. More veto detectors were added and several analysis techniques and cuts were developed to

suppress background events since the 2013 analysis. The *CSD* cut and the *CV-η* cut especially reduced the background events in the blind region by using information of clusters on the CsI calorimeter. The *PSD* cut was efficient towards reducing the neutron background using the waveform information.

The result of $K_L \to \pi^0\nu\overline{\nu}$ analysis using data collected from 2015 set the upper limit of the branching ratio to be 3×10^{-9}, which is a factor of three of the Grossman-Nir bound of 1.4×10^{-9}, as shown in Fig. 1.4. As the KOTO experiment collects more statistics, the upper limit of $BR(K_L \to \pi^0\nu\bar{\nu})$ will reach the Grossman-Nir bound and start eliminating currently existed models that probe for BSM physics. On the other hand, the 2015 analysis result is valuable probing for new physics. As mentioned in Sec. 1.2.3, the FCNC process is forbidden at tree level in the SM. The process of $K_L \to \pi^0 X^0$ was assumed to occur at tree level and the invisible boson X^0 is a Weakly Interacting Light Boson (WILB) [63, 64] with a mass around M_{π^0}. The S.E.S. of probing this new physics process can be calculated using the same method as that used in the $K_L \to \pi^0\nu\overline{\nu}$ analysis as $(1.01 \pm 0.01_{stat.} \pm 0.11_{sys.}) \times 10^{-9}$. The upper limit of $BR(K_L \to \pi^0 X^0)$ can be calculated using Eq. 9.12, substituting with the S.E.S. for the new physics, to be 2.4×10^{-9} at 90% C.L. A list of statistics used for calculation for each beam power in each Run period is in Appx. B.

9.4 Upgrades for the KOTO Detector

Several hardware upgrades can be imposed to reach the SM sensitivity, which is two order of magnitudes away from the 2015 result. The readout system of the CsI calorimeter will be modified to dual-end readout system by adding MPPC readout at the upstream side of the CsI calorimeter. This upgrade is implemented in summer 2018 and is expected to reduce the hadron cluster background by a factor of 10 [65]. A new BPCV detector is planned to be added in the beamline between the CC04 and extend to the CC06 detector to reduce the $K_L \to \pi^+\pi^-\pi^0$ background by detecting π^+ and π^- mesons. The IB detector was implemented in 2016 to increase the depth of detectors at the barrel region to accommodate the photon interaction length. This

was to reduce background from $K_L \to 2\pi^0$ decays [66]. Thicker or denser shielding can be added between the primary beam line and the MB detector to reduce accidental activities from the primary beamline.

Upgrades related to the J-PARC facility can bring us closer to reaching the SM sensitivity. The upgrades include replacing the current T1-target with a rotating "Euro Coin" target and extend the hadron hall facility. The rotating "Euro Coin" target will be able to withstand the beam power up to 150∼200 kW, whereas the current T1-target can hold up to 50 kW or 80 kW with direct water-cooling method [67]. The hadron hall extension will bring the KOTO detector from the current 16° angle from the primary beamline to 5°, which will result in more K_L yield, though modification on the KOTO detectors such as increasing the length of the barrel region is needed [68, 69].

9.5 Conclusion

The KOTO 2015 results gave the upper limit of $BR(K_L \to \pi^0\nu\bar{\nu})$ as 3×10^{-9} with S.E.S. of $(1.30 \pm 0.01_{\,stat.} \pm 0.14_{\,sys.}) \times 10^{-9}$, which updated the current value of 2.6×10^{-8} [8] and is approaching the Grossman-Nir bound of 1.4×10^{-9}, as shown in Fig. 9.2. The hardware upgrades and analysis technique developments enhance our results by an order of magnitude since 2013. We are continuing our efforts towards reaching the SM sensitivity.

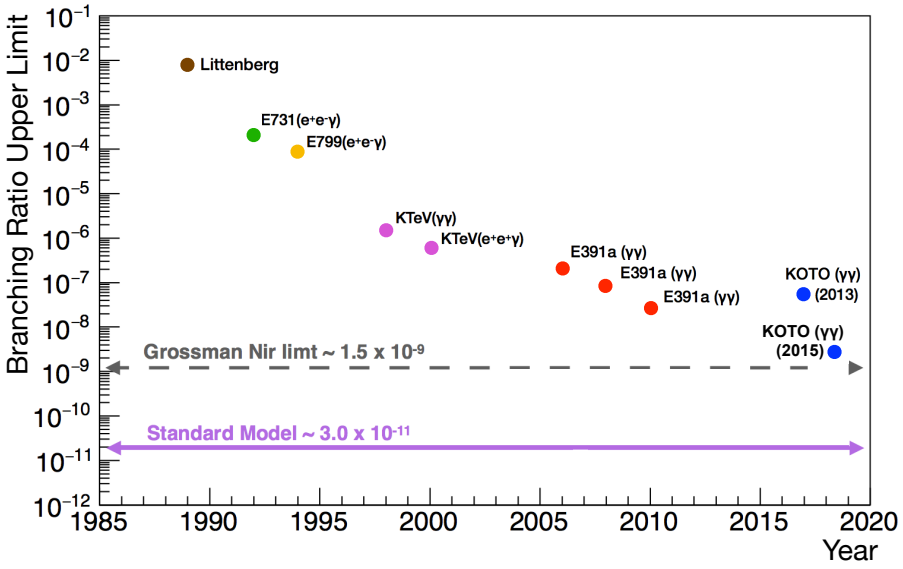

Figure 9.2: Updated searches of $BR(K_L \to \pi^0 \nu\overline{\nu})$ upper limit.

Appendices

Appendix A
Scatter K_L Study

In the KOTO experiment, the $K_L \to \pi^0\nu\bar{\nu}$ signal is identified by observing two photons on the CsI calorimeter with a large transverse momentum, and no activities on the hermetic veto counters. The event reconstruction in the KOTO detector assumes the decay originated from the neutral beam line. Consequently, decay modes with two photons in the final state and decay off the beam line, such as scattered $K_L \to \gamma\gamma$ and $K_L \to \pi^+\pi^-\pi^0$ decays from scattered kaons, can appear to possess a large transverse momentum in the event reconstruction, as shown in Fig. 8.4. Backgrounds from the scattered kaons at the vacuum window can be estimated and scaled using the material density and thickness between the Z0 Al target and the vacuum window, which was made of Kapton. The $K_L \to 3\pi^0$ events were selected for this study because the background contamination was small.

To further study background events resulted from K_L scattering at the vacuum window, the Z0 Al target data was used. The $K_L \to 3\pi^0$ events with COE radius greater than 200 mm were selected for the scattered K_L study. The background contamination from this decay mode was small compare to other K_L decay modes, as detailed in Sec. 8.3.4. The $K_L \to 3\pi^0$ decay should have small P_T, and applying a threshold on the COE radius guaranteed the decay was originated from a scattered K_L. The event reconstruction was carried out by assuming the decay vertex to be on the COE-axis instead of the beam line. The reconstructed K_L vertex momentum and position that passed the COE cut were identified as scattered K_L that can contribute

as background events. These events were used to simulate immediate $K_L \to 2\gamma$ decay inside the decay region and studied with various cuts. The procedure of the scattered K_L background study is described as follows. The same procedure was used to study the scattered $K_L \to \pi^+\pi^-\pi^0$ background events and their contribution.

1. Select $K_L \to 3\pi^0$ events from Z0 Al target data using Table 7.2, Table 5.3, and COE radius > 200 mm.
2. Reconstruct these events onto the COE axis instead of the beam line.
3. Use the reconstructed K_L vertex momentum and position information as seeds to generate MC simulation.
4. Reconstruct these events using the same analysis methods in the $K_L \to \pi^0\nu\overline{\nu}$ analysis.
5. Apply all $K_L \to \pi^0\nu\overline{\nu}$ cuts for scattered K_L background study.
6. Scale the remaining events from the Al target to the vacuum window based on their material properties.

   The scaling method uses the same concept as that in Eq. 9.1, multiplied by the material scaling factor, as shown in Eq. A.1, where ρ is the density of the material and d is the material thickness. The subscripts vac and Al denote the material for the vacuum window (Kapton) and the Z0 Al target. Table A.1 lists the material information.

$$\text{Material Scaling Factor} = \frac{\rho_{vac} \times d_{vac}}{\rho_{Al} \times d_{Al}} \tag{A.1}$$

Table A.1: Vacuum window (Kapton) and Z0 Al target material properties.

Material	Density [g/cm^3]	Thickness [mm]	Z Position [mm]
Vacuum Window (Kapton)	1.42	0.0125	0
Z0 Al Target	2.699	10	-634

Figure A.1 shows the distribution of reconstructed K_L using the beam axis, and the true K_L $P_T - Z_{vtx}$ for the scattered $K_L \to 2\gamma$ study. The number of background scaled

to the vacuum window was 0.014 ± 0.001. In the case of $K_L \to \pi^+\pi^-\pi^0$ background study, no events were observed after applying all cuts. One background event was used to calculate the upper limit of the $K_L \to \pi^+\pi^-\pi^0$ background contribution.

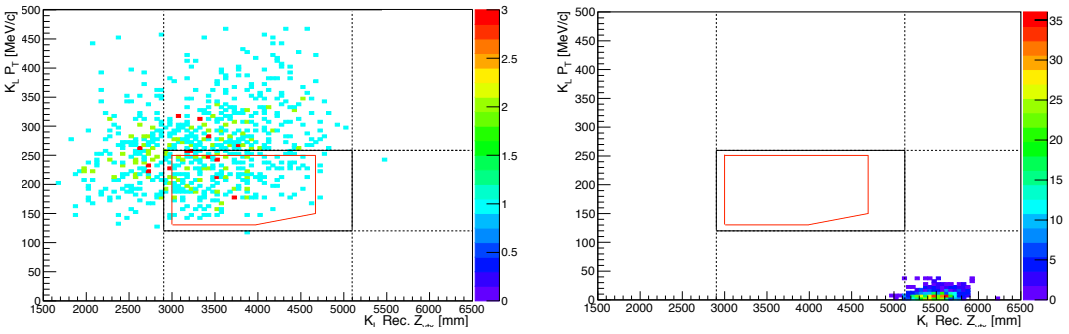

Figure A.1: Reconstructed (left) and true decay (right) of scattered $K_L \to 2\gamma$ events on the $P_T - Z)vtx$ plane. The reconstruction assumed the decay vertex was on the beam axis.

The K_L scattering rate at the Al target can be obtained by comparing to the minimum bias data in consideration of the prescaling factor[1] p, as shown in Eq. A.2. The result of the K_L scattering rate at the Z0 Al target was 3.68×10^{-4}, and 2.4×10^{-6} at the vacuum window.

$$\text{Scattering Rate}_{\text{Al}} = \frac{\#\text{ of } K_L \to 3\pi^0 \text{ events in Z0 Al target run}}{\#\text{ of } K_L \to 3\pi^0 \text{ events in minimum bias run} \times p} \tag{A.2}$$

[1] $p = 3$ for minimum bias data. See Sec. 4.3

Appendix B
Systematic Uncertainty Summary

This appendix lists the systematic uncertainty associated to that listed in Table 9.1 for each beam power in each Run period. The definition of acceptance and efficiency are described in Sec. 9.1. Cut acceptance and veto efficiency figures shown here used Run 65 42 kW as example illustration.

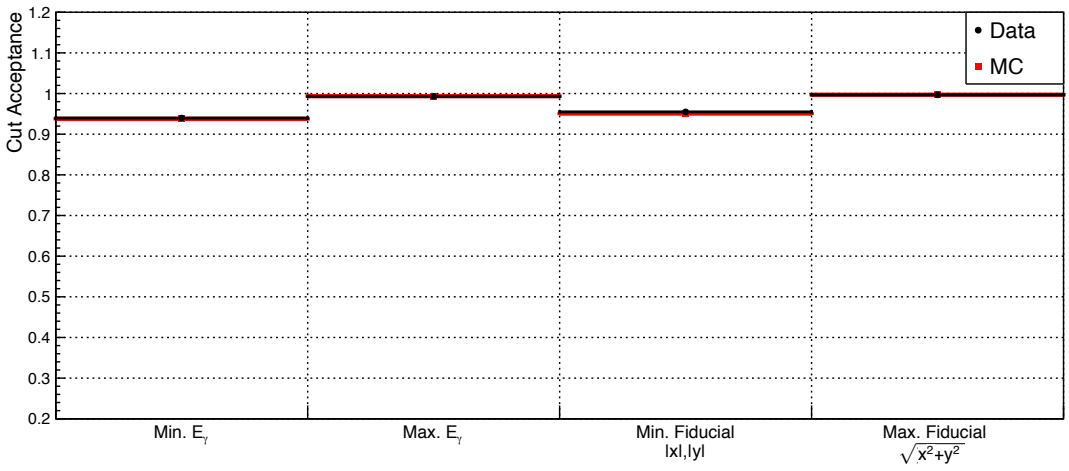

Figure B.1: Acceptance for γ selection.

Table B.1: Systematic uncertainty for γ selection.

Run Condition	Quadratic Sum	1/S.E.S. [$\times 10^7$]	$\sigma_{1/\text{S.E.S.}}$ [$\times 10^5$]
Run 62 24 kW	1.25%	3.886	4.86
Run 62 27 kW	1.40%	6.310	8.86
Run 63 27 kW	1.01%	2.734	2.76
Run 63 29 kW	0.70%	2.195	1.53
Run 63 32 kW	0.85%	6.505	5.52
Run 64 32 kW	1.35%	3.497	4.71
Run 64 39 kW	1.14%	9.119	10.4
Run 65 39 kW	0.92%	10.44	9.63
Run 65 42 kW	0.45%	32.39	14.5
Total	0.81%	77.08	62.8

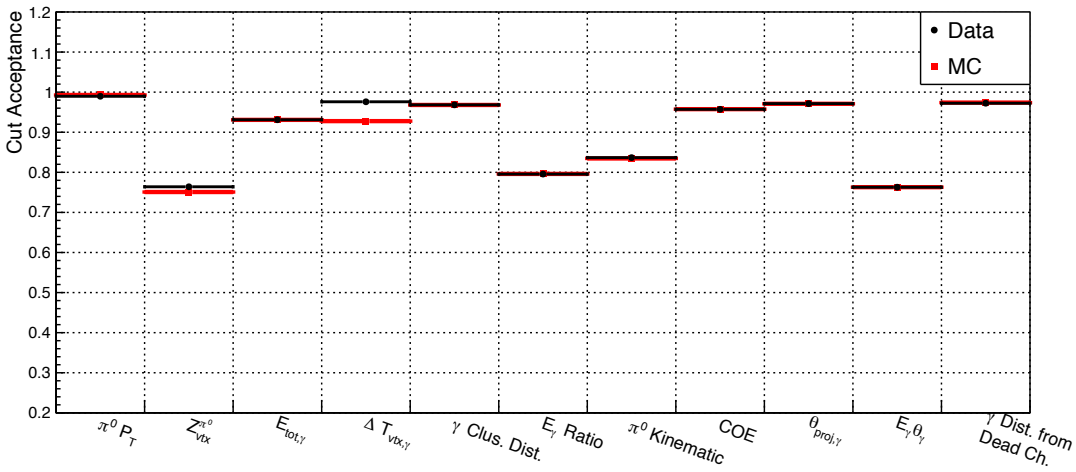

Figure B.2: Acceptance for π^0 selection.

Table B.2: Systematic uncertainty for π^0 selection.

Run Condition	Quadratic Sum	1/S.E.S. [$\times 10^7$]	$\sigma_{1/\text{S.E.S.}}$ [$\times 10^6$]
Run 62 24 kW	5.08%	3.886	1.98
Run 62 27 kW	3.14%	6.310	1.98
Run 63 27 kW	5.04%	2.734	1.38
Run 63 29 kW	7.30%	2.195	1.60
Run 63 32 kW	4.84%	6.505	3.15
Run 64 32 kW	6.85%	3.497	2.39
Run 64 39 kW	5.06%	9.119	4.62
Run 65 39 kW	5.06%	10.44	5.28
Run 65 42 kW	5.25%	32.39	17.0
Total	5.11%	77.08	39.4

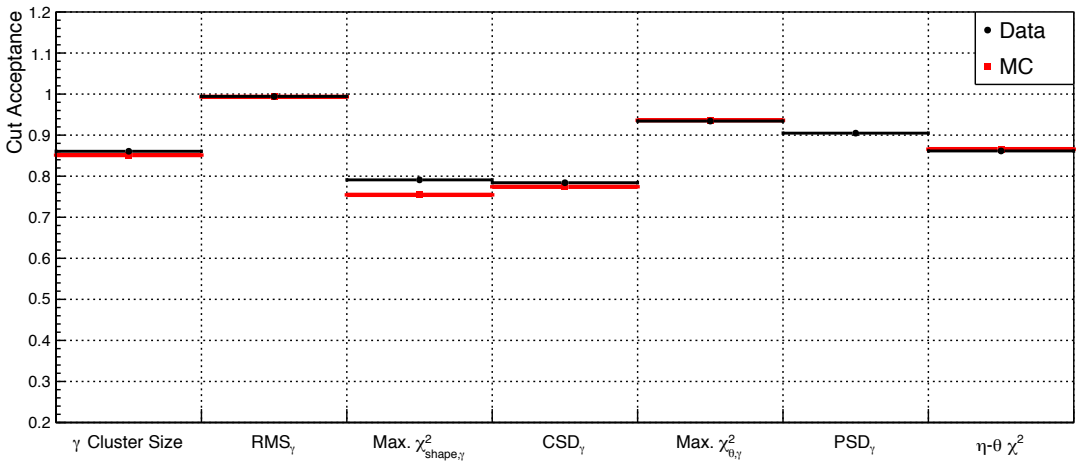

Figure B.3: Acceptance for cluster shape cut.

Table B.3: Systematic uncertainty for shape selections.

Run Condition	Quadratic Sum	1/S.E.S. $[\times 10^7]$	$\sigma_{1/\text{S.E.S.}}$ $[\times 10^6]$
Run 62 24 kW	4.72%	3.886	1.83
Run 62 27 kW	4.67%	6.310	2.95
Run 63 27 kW	4.64%	2.734	1.27
Run 63 29 kW	6.02%	2.195	1.32
Run 63 32 kW	6.78%	6.505	4.41
Run 64 32 kW	5.96%	3.497	2.08
Run 64 39 kW	4.79%	9.119	4.37
Run 65 39 kW	4.23%	10.44	4.42
Run 65 42 kW	5.09%	32.39	16.5
Total	5.08%	77.08	39.1

Table B.4: Systematic uncertainty for $K_L \to 2\pi^0$ selections.

Run Condition	Quadratic Sum	1/S.E.S. $[\times 10^7]$	$\sigma_{1/\text{S.E.S.}}$ $[\times 10^6]$
Run 62 24 kW	3.60%	3.886	1.40
Run 62 27 kW	3.90%	6.310	2.46
Run 63 27 kW	1.39%	2.734	0.38
Run 63 29 kW	1.64%	2.195	0.36
Run 63 32 kW	1.91%	6.505	1.24
Run 64 32 kW	9.34%	3.497	3.27
Run 64 39 kW	5.49%	9.119	5.00
Run 65 39 kW	2.41%	10.44	2.51
Run 65 42 kW	1.30%	32.39	4.22
Total	2.71%	77.08	20.9

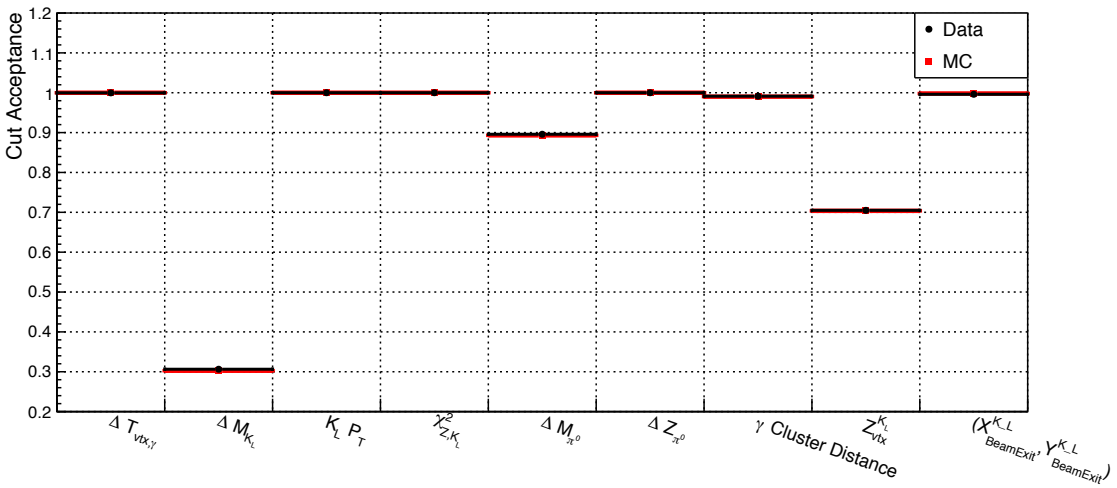

Figure B.4: Acceptance for $K_L \to 2\pi^0$ selection.

Table B.5: Systematic uncertainty for Veto selections.

Run Condition	Quadratic Sum	1/S.E.S. [$\times 10^7$]	$\sigma_{1/\text{S.E.S.}}$ [$\times 10^6$]
Run 62 24 kW	5.72%	3.886	2.05
Run 62 27 kW	4.31%	6.310	2.72
Run 63 27 kW	6.63%	2.734	1.81
Run 63 29 kW	9.16%	2.195	2.01
Run 63 32 kW	3.57%	6.505	2.32
Run 64 32 kW	9.11%	3.497	3.19
Run 64 39 kW	3.32%	9.119	3.03
Run 65 39 kW	3.45%	10.44	3.60
Run 65 42 kW	2.48%	32.39	8.05
Total	3.73%	77.08	28.8

Table B.6: Acceptance for $K_L \to \pi^0 X^0$ decay. The total S.E.S. was 1.007×10^{-9}

Run Condition	A_{sig} [$\times 10^{-4}$]	# K_L at Beam Exit [$\times 10^{11}$]	1/S.E.S. = $A_{sig} \times N_{K_L}$ [$\times 10^7$]
Run 62 24 kW	3.604	1.387	4.998
Run 62 27 kW	3.446	2.370	8.167
Run 63 27 kW	3.126	1.146	3.582
Run 63 29 kW	1.883	1.487	2.800
Run 63 32 kW	1.702	4.954	8.431
Run 64 32 kW	2.668	1.723	4.598
Run 64 39 kW	2.003	5.824	1.166
Run 65 39 kW	2.050	6.496	1.332
Run 65 42 kW	1.953	21.38	4.175

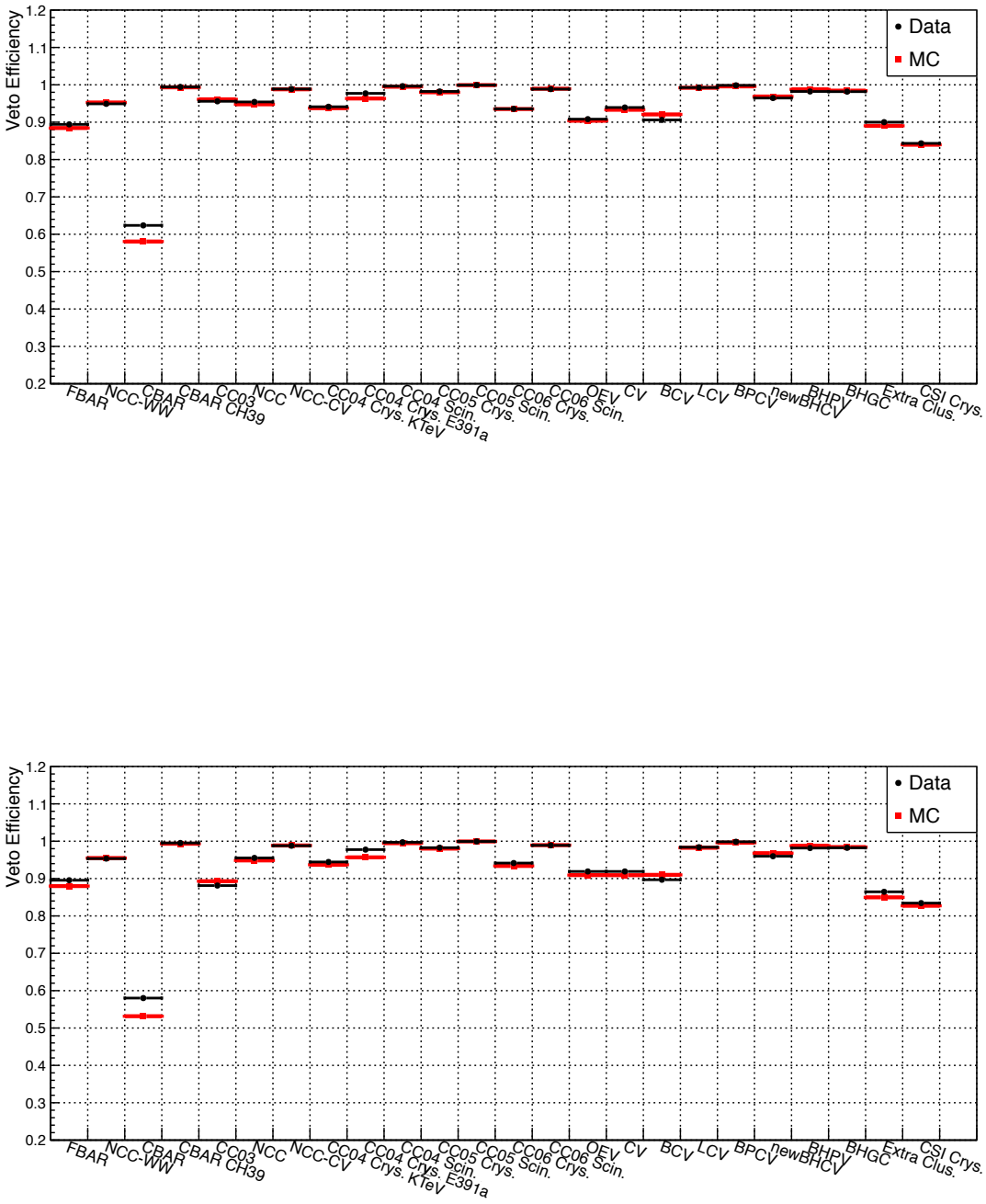

Figure B.5: Veto efficiency for $K_L \to 2\gamma$ (top) and $K_L \to 2\pi^0$ (bottom).

Appendix C
Acronyms, Glossary, and Symbols

Acceptance

Number of events remained over total number of events

ADC

Analog-to-Digital Converter

Beam Exit

Located behind the second collimator (z = -1507 mm)

BR

Branching Ratio

BSM

Beyond Standard Model

COE

Center of Energy

C.L.

Confidence Level

Constant Fraction

A constant fraction method was used to determine the timing of a waveform, where the half-peak on the rising edge of the waveform was used to extract timing information.

FCNC

Flavor Changing Neutral Current

Fiducial

Area of effect. E.g. CsI calorimeter: $R < 900$ mm, $|x|, |y|, > 100$ mm.

FIFO

First-in-First-Out

FPGA

Field-Programmable Gate Array

FWHM

Full Width at Half Maximum

L1 Request (L1Req)

Events that passed the L1 trigger decision

L1 Accept (L1A)

Events that passed the L1 trigger decisions (L1Req) and are considered for a L2 trigger decision

L2 Accept (L2A)

Events that passed the L2 trigger decision

L2 Reject (L2R)

Events that failed the L2 trigger decision

Livetime

Amount of time the system is processing data without any delay over the the total data taking time.

MACTRIS

The MAster Control and TRigger Supervisor board

Masking

Loss of a complete waveform shape due to multiple waveform pulses stack together. An example is shown in Fig. 5.11.

MC

Monte Carlo

Nominal Time

Timing of the trigger issued

PMT

Photomultiplier Tube

P.O.T.

Protons on Target

P_T

Transverse momentum

SM

Standard Model

Spill

The cycle of the extraction of a shot of beam (Fig. 2.3)

SYIM

Switch Yard Intensity Monitor

TMon

Target Monitor

WLS

Wave-Length Shifting

Bibliography

[1] "Standard Model," Online 2

[2] F. Englert and R. Brout, "Broken Symmetry and the Mass of Gauge Vector Mesons," Phys. Rev. Lett, 13 , 321 (1964), 2

[3] P. W. Higgs, "Broken Symmetries, Massless Particles and Gauge Fields," Phys. Lett. 12, 132 (1964). 2

[4] ATLAS Collaboration, "Observation of a new particle in the search for the Standard Model Higgs boson with the ATLAS detector at the LHC," Phys. Lett. B716, pp.1-29 (2012). 2

[5] CMS Collaboration, "Observation of a new boson at a mass of 125 GeV with the CMS experiment at the LHC," Phys. Lett. 716, pp.30-61 (2012). 2

[6] C. S. Wu, *et al.*, "Experimental Test of Parity Conservation in Beta Decay," Phys. Rev. 105, 1413 (1957). 3

[7] J. H. Christenson, J. W. Cronin, V. L. Fitch, and R. Turlay, "Evidence for the 2π decay of the k_2^0 meson," Phys. Lett. 716, pp.30-61 (2012). 3, 4

[8] K. .A. Olive, *et al.* (Particle Data Group), "Review of Particle Physics", Particle Data Group, Chin. Phys. C, **38**, 9, 090001, (2014). 4, 62, 80, 82, 86, 122, 124, 137, 141, 161, 163

[9] M. Gell-Mann and A. Pais, "Behavior of Neutral Particles under Charge Conjugation," Phys. Rev. 97, 1387 (1955). 4

[10] K. Lande, E. T. Booth, J. Impeduglia, L. M. Lederman, and W. Chinowsky, "Observation of Long-Live Neutral V Particles," Phys. Rev. 103, 1901 (1956). 4

[11] L. Wolfenstein, "Parametrization of the Kobayashi-Maskawa Matrix," Phys. Rev. Lett. 51, 1945 (1983). 5

[12] T. Inami and C. S. Lim, "Effects of Superheavy Quarks and Leptons In Low-Energy Weak Processes $K_L \to \mu\bar{\mu}$, $K^+ \to \pi^+\nu\bar{\nu}$, and $K^0 \leftrightarrow \bar{K}^0$," Prog. Theor. Phys. 65, 1772 (1981). 7

[13] A. J. Buras, D. Buttazzo, and R. Knegjens, "$K^+ \to \pi^+\nu\bar{\nu}$ and $K_L \to \pi^0\nu\overline{\nu}$ in the Standard Model: Status and Perspectives," J. High Energ. Phys. 2015, 166 (2015). 7

[14] Y. Grossman and Y. Nir, "$K_L \to \pi^0\nu\overline{\nu}$ beyond the Standard Model," Phys. Lett. B398, 163-168 (1997). 8

[15] F. Mescia and C. Smith, "$K \to \pi\nu\nu$ decay in the Standard Model," Online 8

[16] M. Blanke, "New Physics Signatures in Kaon Decays," PoS(KAON13)010 (2013).

[17] G. Colangelo and G. Isidori, "Supersymmetric contributions to rare kaon decays: beyond the single mass insertion approximation," J. High Energ. Phys. 9809 009 (1998). 9

[18] G. Colangelo and G. Isidori, "General minimal flavor violation," Phys. Rev. D 80, 076002 (2009). 9

[19] J. Comfort, *et al.*, "Proposal for $K_L \to \pi^0\nu\overline{\nu}$ Experiment at J-Parc," KOTO Experiment Proposal (2006). 9

[20] Japan Proton Accelerator Research Complex (J-PARC) Facility. 9

[21] Japan Atomic Energy Agency (JAEA) and High Energy Accelerator Research Organization (KEK), "Radioactive Material Leak at the Hadron Experimental Facility of Japan Proton Accelerator Research Complex (J-PARC)," Accelerator Facility Accident Report (2013). 11

[22] J. K. Ahn, *et al.*, "A new search for the $K_L \to \pi^0\nu\overline{\nu}$ and the $K_L \to \pi^0 X^0$ decays," Progr. Theor. Exp. Phys., **2017**, 2, pp. 021C01 (2017). 11

11, 160

[23] M. Ikegami, "Beam commissioning and operation of the J-PARC linac," Prog. Theor. Exp. Phys. 2012, 2B002 (2012). 11

[24] H. Hotchi *et al.*, "Beam commissioning and operation of the Japan Proton Accelerator Research Complex 3-GeV rapid cycling synchrotron," Prog. Theor. Exp. Phys. 2012, 2B003 (2012). 11

[25] T. Koseki *et al.*, "Beam commissioning and operation of the J-PARC main ring synchrotron," Prog. Theor. Exp. Phys. 2012, 2B004 (2012). 11

[26] T. Sekiguchi, "Neutrino facility and neutrino physics in J-PARC," Prog. Theor. Exp. Phys. 2012, 2B005 (2012). 11

[27] H. Takahashi *et al.*, "Construction and beam commissioning of Hadron Experimental Hall at J-PARC," J. Phys. Conf. Ser. 312, 052027 (2011). 11

[28] K. Agari *et al.*, "Primary proton beam line at the J-PARC hadron experimental facility," Prog. Theor. Exp. Phys. 2012, 2B008 (2012). 11

[29] H. Takahashi *et al.*, "Construction and beam commissioning of Hadron Experimental Hall at J-PARC," J. Phys. Conf. Ser. 312, 052027 (2011). 13

[30] H. Takahashi *et al.*, "Indirectly water-cooled production target at J-PARC hadron facility," J. Radioanal. Nucl. Chem. 305, 803 (2015). 14

[31] T. Masuda *et al.*, "Long-lived neutral-kaon flux measurement for the KOTO experiment," JProg. of Theo. and Expt. Phys. 2016, 1, 1 (2016). 15

[32] T. Shimogawa, "Design of the neutral K_L^0 beamline for the KOTO experiment," Nucl. Instrum. Meth. A 623, 585 (2010). 16

[33] Y. Tajima *et al.*, "Barrel photon detector of the KEK $K_L^0 \to \pi^0\nu\bar{\nu}$ experiment," Nucl. Instrum. Methods A592, 261-272 (2008). 19, 20

[34] N. Kawasaki, "A Gamma and Neutron Counter of Undoped CsI Crystals with WLSFiber Readout for the KOTO Experiment," PoS(KAON13)040 (2013). 20

[35] D. Naito, *et al.*, "Development of a low-mass and high-efficiency charged-particle detector," Prog. of Theo. and Expt. Phys. 2015, 2, 1 (2016). 21, 117, 137

[36] T. Oda, "KOTO 実験におけるビーム周囲荷電粒子 Veto 検出器の開発," M.S. thesis, Saga University (2012). 21

[37] T. Matsumura, *et al.*, "Photon-Veto Counters at the Outer Edge of the Endcap Calorimeter for the KOTO Experiment," Nucl. Instrum. Methods A795, 19-31 (2015). 23

[38] Y. Odani, "中性K中間子稀崩壊実験のためのビーム周辺部ガンマ線検出器について," M.S. thesis, Saga University (2012). 23

[39] S. Banno, "J-PARC KOTO実験のカロリメータ下流部に設置するガンマ線検出器の開発とその性能評価," M.S. thesis, Osaka University (2013).

[40] Y. Takashima, "J-PARC KOTO実験用下流ガンマ線検出器の開発とその性能評価," M.S. thesis, Osaka University (2014). 24

[41] K. Nakagiri, "KOTO 実験の中性ビーム中で荷電粒子を検出する Thin Gap Chamber の開発," M.S. thesis, Kyoto University (2015). 24, 118

[42] I. Kamiji, "KOTO実験における高レート多線式比例計数管のための 波形整形機能をもつ信号増幅器の開発," M.S. thesis, Kyoto University (2015). 25

[43] K. Miyazaki, "J-PARC KOTO 実験における、 $K_L \to \pi^+\pi^-\pi^0$ 背景事象削減のための荷電粒子検出器の開発," M.S. thesis, Osaka University (2016). 25, 119

[44] Y. Maeda, "KOTO実験のための中性子不感型光子veto検出器の開発," M.S. thesis, Kyoto University (2010). 26

[45] S. Shinohara, "KOTO実験におけるビーム外縁部を覆う中性子低感度な光子検出器の開発と性能評価," M.S. thesis, Kyoto University (2016). 26, 27

[46] M. Bogdan, J. Ma, H. Sanders and Y. Wah, "Custom 14-bit, 125 MHz ADC/data processing module for the KL experiment at J-PARC," Proc. IEEE Nucl. Sci. Symp. Conf. Rec., **1**, pp. 133134 (2007). 38

[47] J. Micallef, "Analysis of $K_L \to 2\pi^0$ Decay Mode and Simulation of Data Acquisition System Upgrades for the KOTO Experiment," Bachelor thesis, University of Michigan (2016). 43, 65

[48] G. Thayer, "RCE Platform Technology (RPT) ATCA and the COB," RCE/ATCA Training Workshop at CERN (2015). 49

[49] J. Lee, "Energy Calibration Method for the KOTO CsI Calorimeter," Ph.D. thesis, Osaka University, (2014). 59

[50] Y. Sugiyama, "Pulse shape discrimination method to suppress neutron- induced background in the J-PARC KOTO experiment", Ph.D. thesis, Osaka University (2016). 63, 64, 99, 147

[51] Y. Maeda, "Search for the Decay $K_L \to \pi^0\nu\overline{\nu}$ with a Neutron-Insensitive GeV-Energy Photon Detector", Ph.D. thesis, Kyoto University (2016). 24, 74, 75, 77, 96, 102, 104, 109, 110, 113, 118, 119, 157

[52] T. Masuda, "Development and Experimental Study of the KOTO Detector system using Three K_L Neutral Decay Modes", Ph.D. thesis, Kyoto University (2014). 59, 80, 82, 114

[53] E. Iwai, *et al.*, "Performance study of a prototype pure CsI calorimeter for the KOTO experiment," Nucl. Instrum. Meth. A 786, 135 (2015). 81

[54] K. Sato, "Measurement of the CsI calorimeter performance and K_L momentum spectrum for the J-PARC KOTO experiment," Ph.D. thesis, Osaka University (2015). 98, 108

[55] J. K. Ahn, *et al.*, "Search for the $K_L \to \pi^0\nu\overline{\nu}$ and $K_L \to \pi^0 X^0$ decays at the J-PARC KOTO experiment," arXiv:1810.09655 (2018). 99

[56] A. Hoecker, *et al.*, "TMVA - Toolkit for Multivariate Data Analysis," PoS ACAT, 040 (2007). 99

[57] S. Agostinelli, *et al.*, "GEANT4—a simulation toolkit," Nucl. Instrum. Methods A506, 3, pp.250-303 (2003). 106

[58] S. Agostinelli, *et al.*, "Improvements in the Geant4 Hadronic Physics," J. Phys.: Conf. Ser. 331, 032002 (2011). 111

[59] K. Shiomi, "Measurement of K_L^0 flux at the J-PARC neutral-kaon beam line for the $K_L \to \pi^0\nu\overline{\nu}$ experiment," Ph.D. thesis, Kyoto University (2012). 113

[60] Eito. Iwai, "CsI calorimeter for the J-PARC KOTO experiment," Ph.D. thesis, Osaka University (2012). 113, 114

[61] J. Xu, "Searching For Neutral Kaon Rare Decay," Ph.D. thesis, University of Michigan (2014). 113

[62] R. .D. Cousins and V. L. Highland, "Incorporating systematic uncertainties into an upper limit," Nucl. Instrum. Methods Phys. Res., Sect. A 320, 1-2, pp.331-335 (1992). 160, 161

[63] K. Fuyuto, W. Hou, and M. Kohda, "Loophole in $K \to \pi\nu\bar{\nu}$ Search and New Weak Leptonic Forces," Phys. Rev. Lett., 114, 17, 171802 (2015). 162

[64] G. Hou, W. Hou, and M. Kohda, "Loophole in $K \to \pi\nu\bar{\nu}$ Search $K_L \to \pi^0\nu\bar{\nu}$ Beyond Grossman—Nir Bound," J. Phys. Conf. Ser., 800, 2017, 1, 012024 (2017). 162

[65] K. Kotera, "Four dimensional calorimetry with both-side readout of the CsI calorimeter in the $K_L \to \pi^0 \nu\overline{\nu}$ search," PoS (to appear). 162

[66] M. Togawa, "A new cylindrical photon-veto detector for the KOTO experiment," J.Phys.Conf.Ser., 800, 1, 012043 (2017). 163

[67] H. Takahashi, "Production Target at J-PARC Hadron Experimental Facility," NBI2017: 10th International Workshop on Neutrino Beams and Instrumentation + 4th RaDIATE Meeting, (2017). 163

[68] H. Noumi, "Physics in J-PARC Hadron-hall Extension," JPS Conf. Proc. , 010017, (2017). 163

[69] H. Nanjo, "KOTO and KOTO Step2 to search for the rare kaon decay, $K_L \to \pi^0 \nu\overline{\nu}$," International workshop on physics at the extended hadron experimental facility of J-PARC, (2016). 163